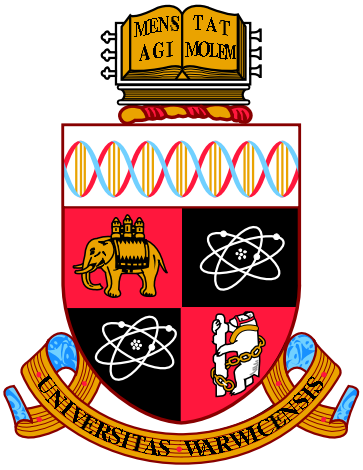

Theoretical Investigation of Solid State Cooling Using Spin Models

by

Matthew Bates

Thesis

Submitted to the University of Warwick

for the degree of

Doctor of Philosophy

Department of Physics

September 2015

THE UNIVERSITY OF WARWICK

Contents

List of Tables

List of Figures

Acknowledgements

There are no words to truly describe the numerous ways in which so many people have supported me and shaped my life, this project and this thesis during my time at Warwick in the last four years. Indeed I may, on reflection, decide that it is necessary to thank everyone that I have met (whether I have been able to get to know them or not) during my entire life, as they have all led me to this point.

You will forgive me, then, if these acknowledgements sound a little like an Oscar acceptance speech, I find it very difficult to not get emotional and poetic under circumstances such as these, the closing of a chapter of my life.

An attempt shall be made to thank only those whose influence has directly led to benefits to this project, to avoid putting myself in some situation where I am left thanking the whole world.

With the flowery introduction out of the way I would first and foremost like to thank my supervisor, Professor Julie Staunton, for all of her help during the project and getting the thesis into the shape it is. I would also like to thank my family: Mum, Andy and Dad, you have all helped me more than you may ever know, giving me inspiration and motivation for not just this project but all aspects of my life. After this it becomes a challenge to thank people in some order without giving offence or risking forgetting someone, so please bear with me as I collect people together as indistinguishable particles and thank them in alphabetical order.

The Big Band (and Wind Orchestra) provided much needed creative expression and fun throughout my time at Uni, I will remember you all fondly as the next stage of my life kicks off. Housemates, for not letting me live on my own (where I

might have gone stir crazy) and your patience with me and my messy ways I thank you, it has been a privilege to live with all of you and to have learned from you all. MathsPhys society, this set (not group!) encompasses a great many people to whom I am thankful for different things, but the unifying connection was (and somehow, remains to be) the MathsPhys society and for that I will always be thankful, I hope we see each other again soon. PS0.01 (and assorted hangers on), my thanks for the various conversations (including, but not limited to, those that were productive, entertaining and #Deep) and support that you all provided me whether I was brave enough to ask for it or not. The University of Warwick Mixed Hockey Club (and Berkswell), you reminded me that life wasn't all about work and I had to get on it (for once) from time to time, whenever I was having a bad time, being able to vent steam at some hockey balls and run like a maniac around the pitch helped me get some perspective back, it has been a privilege to know you all.

Having said that I would not single anyone out, I find it necessary to thank (in alphabetical order) Drs. Bennett, McDonald and Refaat for their advice and support in getting this thesis written.

Thank you all!

Declarations

This thesis is submitted to the University of Warwick in support of my application for the degree of Doctor of Philosophy. It has been composed by myself and has not been submitted in any previous application for any degree.

The work presented (including data generated and data analysis) was carried out by the author except in the cases outlined below:

Figure 3.4 was reproduced from reference [69].

Figure 4.4 was reproduced from reference [78].

Figure 4.8 was reproduced from reference [31].

Figure 4.21 was reproduced from reference [61].

Figure 4.22 was reproduced from reference [85].

Chapter 5 was a collaborative effort and the style and notation here are that of Goldsborough from reference [88], reproduced with permission.

Abstract

A mean field spin model coupled to a thermal model of a solid is used as a description of the electrocaloric effect in relaxor ferroelectrics at both first and second order transitions. This theoretical model is also used in efforts to find the tricritical point of transitions to maximise the adiabatic temperature change due to the electrocaloric effect while minimising the hysteresis losses in a cooling cycle. The electrocaloric effect is the adiabatic temperature change exhibited by a material under the sequential application then removal of electric fields. Relaxor ferroelectrics are materials with two interaction scales, local interactions in polarised nano regions (PNRs) and longer range interactions between PNRs. Electric dipoles are modelled as spins and their alignment due to an external field is used to examine polarisation-electric field loops. The results are compared to experimental data to determine values of parameters that may be used in simulations to model the electrocaloric effect. I reproduced simulations of the electrocaloric effect in the ferroelectric material lead zinc niobate-lead titanate [$Pb(Zn_{1/3}Nb_{2/3})O_3$-$PbTiO_3$] by coupling the dipolar entropy of the spins to the entropy of a thermal lattice one can examine the temperature increase that must occur as the dipolar entropy decreases in an external field. The results of this simulation agree with experiment. Novel work is carried out in a prediction of the strength of the electrocaloric effect in polyvinylidene fluoride trifluoroethylene, P(VDF-TrFE), using a simulation where the material parameters are determined from the comparison of simulated polarisation-electric field hysteresis loops with experimental results. The simulations suggest that P(VDF-TrFE) is a material worth investigating experimentally because even though it has a weak electrocaloric strength, under large fields the potential adiabatic temperature change at

room temperature has promise for replacing conventional refrigerants.

Due to the simplicity of this coupled model and the physical similarities between the electrocaloric effect and the magnetocaloric effect (an analogous effect observed in certain magnetic materials where an adiabatic temperature change is seen under the application and removal of a magnetic field) an investigation is also carried out on the magnetocaloric material iron rhodium (FeRh). In simulations I varied global and local stoichiometry to affect the ordering of spins and thus the entropy and strength of the magnetocaloric effect. I compared the results of our simulations with experiment and examine the variation in peak isothermal entropy change and adiabatic temperature change under variation in stoichiometry as well as the effects on the full width at half maximum. The results show that a simple model can give a qualitative representation of the effect.

Work of a different nature is presented at the end of the thesis due to it being a short and complete topic which interested me during my PhD. Details are given on how Catalan numbers may be used to determine the depth of leaves in binary tree graphs and path length between them using both diagrammatic notation and the methodology of generating functions. An analytic solution is drawn from a combinatoric problem that initially appeared to only be soluble by brute force numerics.

Chapter 1

Introduction

1.1 Introduction

Since 1834 [1], the developed world has enjoyed the benefits of the vapour compression refrigeration cycle and the fantastic cooling power that it brings. In the summer in the United States of America, up to fifty percent of energy consumption is used for some form of cooling [2].

The best vapour compression refrigerators designed today reach a maximum of fifty-five percent of the ideal Carnot efficiency [3] which is likely close to the limits of what will be possible in this mature and well studied field. Many refrigerants currently used in a vapour compression cycle come from the Hydrofluorocarbon (HFC) family [4]. HFCs are used as a substitute for earlier ozone depleting refrigerants and represent 89 percent of US fluorinated gas emissions [5]. As fluorinated gases have a large CO_2 equivalent [6] this means that HFCs may account for up to 45 percent of the world's CO_2-equivalent emissions by 2050 [4]. If an alternative method of refrigeration could be found that is less energy intensive then it would be cheaper for the end user and less polluting for the environment.

This means that a large step could be taken in tackling the issue of global warming if a more energy efficient refrigeration system using less polluting materials should be developed. Solid state refrigeration using various caloric effects could provide this solution. A caloric effect is where the application and subsequent removal of some external force causes an isothermal entropy change which leads to an adiabatic temperature change [7].

Elasto- and Barocaloric effects are caused by uniaxial stress and pressure respectively. Magnetocalorics rely on the application of a magnetic field and have the potential of reducing the energy consumption of a domestic fridge by fifty per-

cent [8]. The electrocaloric effect, achieved with the application of an electric field, has the chance to be more readily applicable than the magnetocaloric effect due to the relative ease of generating large electric fields in comparison with magnetic fields. The substitution of rare earth elements in a refrigerant can enhance the magnetocaloric effect [9], however due to geopolitical reasons the supply of rare earths is expensive and unreliable. Giant electrocaloric effects have been found with materials that are widely available [10] and with a more detailed understanding of the mechanisms behind the electrocaloric effect it may be possible to optimise an electrocaloric refrigerant to produce an effect as strong or even stronger than that of the magnetocaloric effect.

The thesis will be structured as follows. The rest of this chapter will present a brief overview of the field of electro and magnetocalorics as relevant to the work presented in this thesis, this will set the scene for the work undertaken but is, by no means, an exhaustive review of the literature.

I will use chapter 2 to discuss the thermodynamics of a cooling cycle introducing the mathematics and methodology as well as the efficiencies and metrics that will be useful in describing the electrocaloric effect.

I shall then introduce statistical mechanics in chapter 3 to provide a general description that can be applied to a refrigerant, including the description of the phase transitions that it must pass through to maximise the strength of the electrocaloric effect and addressing potential sources of loss during a cooling cycle.

In chapter 4 I present a simple model of spins (to represent the electric dipoles of a refrigerant) coupled to a phonon lattice that will enable us to describe the isothermal entropy changes and adiabatic temperature changes that the system undergoes during a cooling cycle. Novel work is carried out to investigate the tricritical point of antiferroelectric to ferroelectric phase transitions using our model. I will then collate the ideas introduced in the previous chapters and use them to reproduce simple models from the literature. This produces an understanding of how the basic ingredients examined earlier in the thesis lead to a successful model of solid state cooling. This chapter will demonstrate the novel work done on applying our model of electrocalorics to the analogous field of magnetocalorics to examine the isothermal entropy change and adiabatic temperature change in iron rhodium and how the peak and widths of these responses are affected by the disorder in the material.

I then present work unrelated to the bulk of the thesis in chapter 5. This is, however, a brief and complete project exhibiting other work performed during the PhD. It is an explanation of how Catalan numbers may be used to enumerate

binary tree graphs of a given size and the number of vertices on a path between any two leaves of the tree.

Finally chapter 6 summarises the work in the thesis and provides a discussion for how work may proceed in this area.

1.2 Caloric Materials and Caloric Effects

The field of electrocalorics is relatively young in comparison with both the field of magnetocalorics and that of the well researched traditional vapour compression cycle, yet there is already much written on the subject. In the next few sections we shall review some of the topics relevant to this thesis, namely the properties of ferroelectrics and relaxor ferroelectrics, thin film polymer relaxor ferroelectrics and anti ferroelectrics and their suitability in electrocaloric applications.

1.3 Ferroelectrics

Ferroelectricity was first reported in 1920 by Valasek [11] and was so named due to the similarity of the permanent electric dipole to the permanent magnetic moment observed in ferromagnetic materials. Shortly after the discovery of ferroelectricity came the realisation of the electrocaloric effect in Rochelle salt in 1930 [12] which can be seen as analogous to the magnetocaloric effect found in 1881 [13]. However, due to the weakness of the effect in traditional ferroelectrics, it was another twenty five years before the electrocaloric effect was revisited with the possibility of creating a practical cooling cycle [3].

Just as ferromagnetic materials at sufficiently low temperatures have an intrinsic alignment of magnetic spins without the application of any external magnetic field, ferroelectric materials have a spontaneous net alignment of electric dipoles even without the presence of an external electric field [14]. Above the Curie temperature (T_C) of a ferroelectric/magnetic (FE/FM) material exists the paraelectric/paramagnetic (PE/PM) phase where the electric/magnetic spins are unaligned and there is no net polarisation/magnetisation. Cooling below T_C the spins begin to align in the FE/FM phase.

In ferroelectrics this transition is often associated with a structural transition, such as a small displacement off centre of the titanium ion in lead titanate ($PbTiO_3$) when the material changes from a cubic to tetragonal structure on passing below T_C [15], this asymmetry in the unit cell causes a dipole to form along the direction of the displacement.

Ferroelectrics have competing short range and long range order. Short range order causes the formation of domains within the ferroelectric where the electric dipoles of individual unit cells are all aligned in the same direction. The long range order within a ferroelectric is the alignment of the domains which are less strongly linked than individual dipoles. The interfaces between domains of differing alignment are called domain walls, these have an associated energy which is the difference between the ground state energy (found in the situation with the wall) and the energy of the system with all dipoles aligned. As an external field is applied the domain walls will move as dipoles align with the external field, domains aligned with the field will grow in size while those not aligned will shrink. Thus the discussion of the free energy and entropy of a ferroelectric ought to use a macroscopic model to consider the details of the domains and domain wall motion rather than individual dipoles.

Ferroelectric materials are, by definition, associated with polarisation hysteresis under the application and removal of an electric field. Hysteresis is the effect observed when there is a delay in response from a system with respect to an external stimulus. For example a paraelectric system will show no hysteresis, freely aligning itself with an externally applied field instantly, whereas a ferroelectric system has an intrinsic polarisation before the application of the external field. Should the field point anti-parallel to this polarisation, the polarisation will not immediately align with the field but there will be a delay until the field is sufficiently large before the polarisation aligns with field as shown in figure (1.1) [14].

Energy is put into the material in destroying, creating and moving the domain walls to allow the domains to fully align with the field. This is energy that is not used in creating an isothermal entropy change (ΔS_{iso}) and thus is energy input that, under a cooling cycle, would be wasted (see section (3.4) for more details).

The effect of hysteresis was modelled by (among others) Vives et al. [16]. Their model gives illumination on the effects behind hysteresis, the basic model takes Ising spins on a cubic lattice with nearest neighbour interactions and interactions with the external field. They then go on to introduce disorder to the system through the use of random on site fields (such as those that would arise from disordered chemical clusters as mentioned in section (1.4)), the disorder of random bonds (such as those between dipoles or domains that have domain walls of different thickness between them) - both of these effects will be discussed later in section (4.1). This allows for a good description of hysteresis losses due to polarisation hysteresis under the application of an external field, as the polarisation against applied field path is traced out (see figure (3.5) in section (3.4)) some energy is needed to overcome the

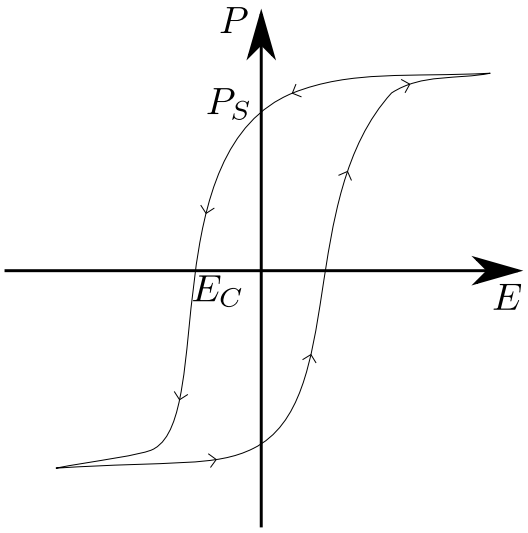

Figure 1.1: A hysteresis loop showing polarization against applied electric field oriented in the same axis. P_S is the value of polarisation that remains when the field is removed, called the remnant polarisation. E_C is the coercive field - the field strength required to reduce the polarisation to zero.

remnant polarisation of the material, this energy is lost every cycle and so reduces the efficiency of the system - this occurs for magnetic systems as well [17]. Large hysteresis is associated with the large entropy change of a first order transition (see section (3.3)) while second order transitions are associated with significantly reduced hysteresis losses [18]. It is possible to determine polarisation hysteresis loss from polarisation hysteresis loops [19].

It has been discovered more recently that not only can the direct (or positive) electrocaloric effect occur where the application of an external field leads to an initial increase of temperature of the material (the removal of the field then leads to a decrease of temperature which leads to the cooling cycle), there is also an inverse (negative) electrocaloric effect [20] where the application of the field leads to a decrease of temperature [21] - it is even possible to see both signs of the effect in one material at different phase transitions, e.g. antiferroelectric-ferroelectric and ferroelectric-paraelectric [22].

1.4 Relaxor Ferroelectrics

The resurgence in interest in the electrocaloric effect came due to the discovery of a temperature change under the application and removal of an electric field in relaxor ferroelectrics or relaxors.

Experimentally there have been found to be two temperatures of interest in relaxors [23] where peaks have been observed in both the strength of the electrocaloric effect [24] and the electric permittivity of the sample [25]. This leads to a description of the formation and alignment of polarised regions on the scale of nanometres (Polar Nano Regions or PNRs) [26]. At very high temperatures, relaxors experience a paraelectric (PE) phase (which is the same as as a PE phase in a traditional ferroelectric), on cooling they pass through a so called ergodic relaxor (ER) phase [27] in which the PNRs form, these are local clusters of alignment embedded in the material which itself has a random orientation of dipoles. This alignment occurs as the material is cooled from the PE phase to below the Burns temperature, T_B. Even further below this there is the freezing temperature (T_f) at which the PNRs become frozen in orientation and the relaxor becomes non-ergodic [28]. For temperatures $T_f < T < T_B$, the PNRs are free to independently explore the phase space and the vector of the electric dipole may point in any direction, hence the term ER. Below T_f, should an external field be applied then the PNRs would align and the material would behave as a ferroelectric. Heating an aligned relaxor above T_f again will return it to the ER phase. Phase transitions in relaxors occur across a broader range of temperature than those found in traditional ferroelectrics which are localised to one temperature [21]. This is due to the variation in size and relative strength of the PNRs, with this variation they form and align across a range of temperatures (centred around T_B and T_f respectively) leading to a diffuse transition not observed in pure ferroelectrics. There have been models describing the size and distribution of PNRs with statistical mechanics ([29], [30], [31]) and this school of thought will influence this thesis.

A key structural difference between ferroelectrics and relaxors is the lack of long range structural order in relaxors [32] at high temperatures, the breaking of the regular, ordered system into distinct PNRs [33] removes the order found in aligned ferroelectrics. The relaxors, however, develop long range coherence below T_f [15] and thus we may assume long range order in the system [34] even though it may not, at first glance, be expected. Note also that the transition into the FE phase in a ferroelectric is driven by a structural transition, while relaxors can become polarised in an external field at T_B and a remnant polarisation will be kept only below T_F and neither temperature is necessarily a structural transition.

Relaxors also exhibit strong electrostriction, that is that they experience large strain when in an electric field [35]. This gives evidence of the long range length scale of the interactions between polar nano-regions as this electrostrictive nature appears in the ER phase [36]. The especially high electrostriction in relaxors when

compared with regular ferroelectrics [37] is due to the expansion and contraction of the PNRs under external fields [38] which is not present in ordinary ferroelectrics. This strain in the material can induce a secondary electrocaloric effect which is often neglected in theoretical treatments even though it may contribute significantly to the total isothermal entropy change [3].

Traditional relaxors are a subset of the inorganic ferroelectric crystals with a perovskite structure i.e. ABX_3 where A and B are cations and X is an anion, usually oxygen, which binds to both - for example $PbTiO_3$ [28] as shown in figure (1.2). These crystals were originally lead based [3] although more recently lead free compounds have been created which still have an appreciable electrocaloric effect [39]. In order to increase the strength of the effect, relaxors often have substitution of elements on the B site to introduce compositional disorder to the system and this can be controlled by the way the material is formed with quick annealing from high temperatures not allowing the system to reach a (complex) ordered ground state, but instead resting in a metastable state [28].

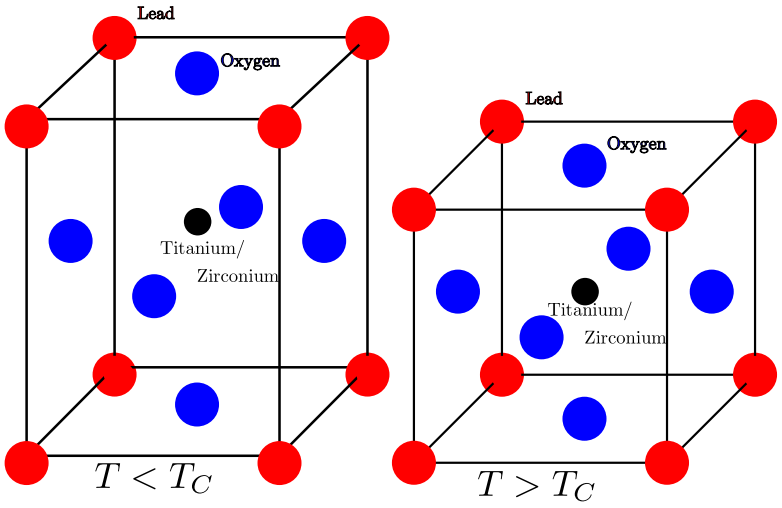

Figure 1.2: $PbZnO_3 - PbTi_3$, an example of the unit cell of a cubic perovskite. A system of purely $PbZnO_3$ or $PbTiO_3$ would be a regular ferroelectric which goes through a structural phase transition at T_C from tetragonal (with a displacive central ion leading to an electric dipole) to cubic (regular with no displacive ion, thus no spontaneous polarisation). The disorder caused by the possible substitution of a zinc ion in place of a titanium ion or vice versa causes the change to a relaxor.

Such a crystal relaxor system $(Pb(Zn_{1/3}Nb_{2/3})O_3$-$PbTiO_3$ also called PZN-PT) was investigated by Valant et al. [31]. Experimentally they grew single crystals of PZN-PT and observed how the strength of the electrocaloric effect was affected by

the strength of the externally applied electric field. They found that the effect was weak far below the Curie temperature (T_C) of the material, rapidly increased and peaked at T_C and then slowly decreased beyond T_C (see figure (4.8) in section (4.2)). They created a simple mean field model of Ising spins (here modelling dipoles of the mobile titanium ions in the unit cells of a PNR) coupled to an Einstein lattice to simulate the behaviour of the dipoles and the connection with phonon activity in their crystals. Disorder in this material is modelled from the variety in the transition temperatures of the PNRs. The results (see figure (4.7) in section (4.2)) hold well below T_C, but predict that the electrocaloric effect will drop away rapidly above T_C. This suggests that above T_C the interactions between the electric dipoles of the PNRs is not the only contribution to the electrocaloric effect. The literature suggests that while the interactions between PNRs may cease to overcome thermal agitation above T_C, the PNRs continue to exist and so may be aligned under an external field until their destruction at the Burns temperature and this allows for the continued existence of the electrocaloric effect [40].

As the strength of the effect is partly related to the coupling of the relaxor to the external field, the limitations of the electrocaloric effect have been the maximum strength of field that may be applied, restricted by the electric breakdown strength of the specimens [41] beyond which point the relaxor becomes conductive and a cooling cycle cannot be created. Moving from a bulk crystal to a thin film material allows larger fields to be applied leading to a greater adiabatic temperature change [42]. There is a general inverse relationship between the breakdown field strength and film thickness [43] which is due to the different mechanisms that lead to breakdown in thin films and bulk materials. In bulk materials the electric breakdown strength is proportional to the square root of the Young's modulus and micro cracks in the material can lower the Young's modulus, thus weakening the dielectric breakdown strength [44]. In thin films the Young's modulus is significantly greater and the dominant contribution turns out to be an ionisation avalanche [3] where one part of the film becoming ionised induces ionisation in its neighbours and this spreads through the material.

A different approach to using a spin lattice coupled to an Einstein solid was taken by Pirc et al. [36] when they created their Spherical Random Bond Random Field (SRBRF) model which has both random bonds - to reproduce the effect of a range of interaction strengths between the dipoles of the PNRs - and also random on site fields which are from random chemical clusters within the relaxor. By assumption the random bonds are infinitely ranged and Gaussian distributed, similarly the localised random fields are Gaussian distributed. The dipoles of the PNRs

are reorientable and count towards the random bonds whereas the random chemical clusters are static in the material and so provide a permanent, on site random field, the disorder (randomness) of both comes from the great variation in size and location of PNRs and chemical clusters within a relaxor. This model is based on the experience of the authors in the field of spin glasses and, indeed, is solved using the replica method as one may do with spin glasses.

1.5 Polymers

The advantage of thin films over bulk materials is their higher dielectric breakdown strengths meaning they can be exposed to larger fields and produce a larger adiabatic temperature change (ΔT_{adi}), ferroelectric polymers may have even larger dielectric breakdown strengths leading to the opportunity for greater ΔT_{adi} [3]. Present research is concentrated around poly(vinylidene fluoride-trifluoroethylene) or P(VDF-TrFE) [21] possibly with the addition of chlorofluoroethylene to make the terpolymer P(VDF-TrFE-CFE) [26]. Such polymers may be electron irradiated to break up the large polarisation domains and form polar nano-regions (the spins of our model), thus creating a relaxor [45]. Polymers can also exhibit a large electrostrictive response to an applied external field (due to the flexibility of the PNRs and the surrounding medium) [37] increasing the strength of the secondary electrocaloric effect when compared with inorganic relaxors.

The chemical chain of P(VDF-TrFE) is shown in figure (1.3), the ferroelectric properties of the polymer chain come from the large variation in electronegativity of the constituent elements [46]. Electronegativity is a measure of how strong the attraction is between an atom and a pair of covalent bonding electrons, with equal electronegativity the electrons will sit equidistant between two atoms, however should one atom have a larger electronegativity then it will attract the electrons to it and this displacement of the electrons will induce an electric dipole [47]. Fluorine has an electronegativity of 4.0 on the Pauling [48] scale while carbon and hydrogen have values of 2.6 and 2.2 respectively (for reference the least electronegative materials are caesium and francium with a value of 0.7). A rule of thumb [47] is that for an electronegativity difference of around 2 the interactions could be considered ionic, so we can see that the fluorine atoms will exert an almost ionic character on the system, leading to strong electric dipoles.

As the ferroelectric polymer is formed out of a melt, rod shaped grains form and the size of these grains and the roughness of the surface is strongly dependent on the annealing conditions [49]. This structural disorder means that creating a

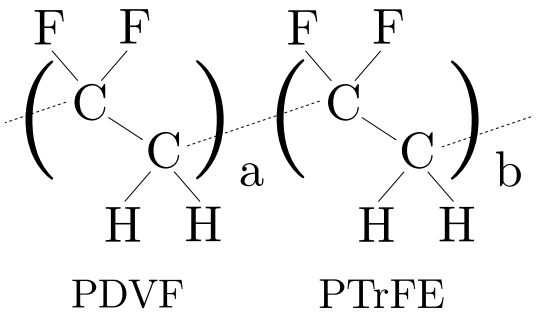

Figure 1.3: The monomers of the P(VDF-TrFE) copolymer

physically realistic model of relaxor polymers is infeasible, but perhaps the model created for crystal relaxors would be a good starting point.

That was the thinking of Pirc et al. [26] who adapted their SRBRF model ([36], see the previous section) for a crystal relaxor and used it to model a polymer, they take the various grains in the polymer to be the sources of PNRs and produced the same Hamiltonian as before with the same Gaussian distribution of interaction strengths and random fields. The main differences to their previous work is the argument that there are far fewer random chemical clusters in the polymer than in the inorganic crystal and thus the effect of the random fields is weaker.

1.6 Antiferroelectrics

As a $\Delta\mathcal{S}_{iso}$ leads to a large ΔT_{adi}, finding materials which display such an entropy change is important. Such changes need not only occur at the ferroelectric to paraelectric transition but also at an antiferroelectric to ferroelectric transition and these have been found in inorganic relaxors [24], [42] (note that both of these references show positive electrocaloric effect at both transitions). Should the applied external field induce a phase transition, then the difference between the order parameters of the antiferroelectric and ferroelectric phases could cause a large $\Delta\mathcal{S}_{iso}$.

The coexistence of competing phases is reminiscent of the work of Imry and Wortis [50] where they suggest that, should different regions of a material have different transition temperatures (note that the transition does not need to be antiferroelectric to ferroelectric, it could be any other transition as long as there is a change of phase) one would expect to find a diffuse transition peak rather than a sharp transition at the transition temperature, T_T; relaxors have a diffuse phase transition [51] thus such a model could be well used to describe them. A naive argument to describe the diffuseness of the phase transition would be that each region

would change phase at the T_T it would have were it a bulk sample not in contact with any other region. This, however, is not a full view of the picture as when one region changes phase it would create a phase interface between it and its neighbours, such an interface would have a free energy cost associated with it, should this cost be greater than the free energy gained by the region changing phase it would be energetically unfavourable for the change of phase to occur. This implies that inhomogeneity within the material can have an effect on a phase transition and thus on the $\Delta\mathcal{S}_{iso}$ and ΔT_{adi} that would be produced, it would be of interest to observe this effect in both inorganic relaxors and the relaxor polymers to see the difference between the two and how changing the compositional disorder would affect the electrocaloric effect in each. Their model predicts that some fraction of regions will be able to exist in their energetically favourable phase within a bulk in a different phase this would lead to, at least, partial rounding of a first order phase transition as there would be different regions transitioning at different times, the model is unable to predict whether complete rounding (i.e. complete removal of the first order character of the transition) would occur or not.

Peng et al. examined antiferroelectric relaxors [24]. They explicitly observed a strong $\Delta\mathcal{S}_{iso}$ and ΔT_{adi} at the antiferroelectric-ferroelectric transition but also the two temperature scales of a relaxor at the ferroelectric-paraelectric transition where many experiments reveal a single peak at the T_C of the material, there is in fact a clear double peak. Of these two peaks, the higher temperature one is associated with T_B (i.e. where the PNRs begin to form, the ergodic relaxor phase) and the lower with T_f (where they align and freeze). They point out that such a double peak structure has been seen in relaxor ferroelectrics [23] in addition to their antiferroelectrics, thus suggesting that the double peak is not an artefact related to the antiferroelectric nature of their material lead barium zirconate but is related to the formation and freezing of PNRs.

1.7 Magnetocalorics

The magnetocaloric effect (the magnetic equivalent of the electrocaloric effect) was first observed in 1881 by Emil Warburg [13], far before the electrocaloric effect. Initially harnessed to cool below liquid helium temperatures (using materials such as cerium magnesium nitrate) it was more thoroughly investigated than the electrocaloric effect as the first magnetocaloric materials displayed a larger temperature change than the first electrocaloric materials under similar field strengths.

Interest piqued when a so called 'giant' magnetocaloric effect was observed in

$Gd_5(Si_2Ge_2)$ at room temperature in 1997 [52], this suggested that magnetocaloric could be applied to room temperature refrigeration.

One magnetocaloric of particular interest in this project is iron rhodium (FeRh). FeRh forms a structure where there are unit cells with one atom type on the corners and the other atom type in the centre. However, at non-zero temperatures there is a non-zero probability of finding an Fe atom having displaced an Rh atom from the Rh lattice or vice versa (at least one or two percent of the sites may experience this after typical annealing processes [53], the higher the temperature the greater this probability). Thus if the system is quenched from a high temperature it may relax into a state with large deviation in local stoichiometry (the ratio of the constituent elements) from a global 50-50 mix.

Deviation from stoichiometry is an important consideration for FeRh as it is a magnetic material that is very sensitive to composition, even a 2% variation in iron concentration can completely remove a ferromagnetic to antiferromagnetic phase transition that exists when the material contains equal proportions of iron and rhodium [54]. The temperature of this transition can be readily changed by varying the way the sample is treated (e.g. via electron irradiation) [55].

Such sensitivity to composition makes FeRh an interesting material to study to examine the effects of local structural disorder. Such disorder is well suited to being modelled by the treatment of Vives et al. [16] mentioned earlier and as such makes a natural continuation of the investigation set up with the model that shall be produced in this project.

1.8 Key Features From the Literature

We have seen in this review of the literature that even inorganic, ferroelectric crystals are complex systems but that the key contribution to a model of the electrocaloric effect comes from the interactions between electric dipoles (vectors linked to particular locations in the material - much like vector spins on a lattice) and the interaction with underlying structure in the material that compensates for any induced decrease in dipolar entropy. We also know that polymers are significantly more complicated materials to model, yet due to their high electric breakdown strength can exhibit a larger $\Delta\mathcal{S}_{iso}$ than bulk or thin film crystals. It is also clear that the large $\Delta\mathcal{S}_{iso}$ associated with an antiferroelectric to ferroelectric transition can lead to a large ΔT_{adi}.

Current experimental work on inorganic relaxors focusses heavily on perovskite crystals and specifically lead based materials, while the polymer research

field is dominated by P(VDF-TrFE) which contains fluorine. If research can find relaxors without these environmentally damaging materials which also have a large ΔT_{adi} then there is strong justification for using the electrocaloric effect over conventional refrigerants (such as the environmentally harmful HFCs) or the magnetocaloric effect (which currently relies on rare-earth elements [21] and larger fields than the electrocaloric effect [3]).

Two key targets in research then are to create a general (not relaxor specific) model that, at the very least, produces qualitative agreement with experiment and has the predictive power to simulate parameters of different elements and suggest what the effect of the addition or removal of certain elements to a mix may be and how it compares to current relaxors. The other target would be an understanding of the mechanism behind the electrocaloric effect in the paraeletric phase, the models predict that this cannot be simply due to dipolar interactions.

With these thoughts in mind we proceed now to creating a spin based model of the electrocaloric effect to represent what occurs below the Curie temperature of a relaxor.

Chapter 2

Classical Physics of a Cooling Cycle

2.1 Cooling Cycles

It is important to be able to have an understanding of the phenomenology behind the cooling cycle we wish to employ and to have an estimate of the strength of the effect. This chapter will be concerned with producing a simple, general description of cooling cycles - reversible processes where due to external work done on a refrigerant and heat exchange with the environment, the temperature of the refrigerant is lowered such that it may be used to cool a volume. We shall examine these cycles using classical thermodynamics before describing important quantities to measure for comparison between refrigerants and then telling of the phenomenology of a general caloric cycle.

2.2 The Carnot Cycle

The maximum efficiency that an ideal cooling cycle can achieve is called the Carnot limit and is reached by the Carnot Cycle [56]. In the general case a cycle runs as follows: reversible, adiabatic work (also called isoentropic work as entropy remains constant because there is no heat or matter transfer) is done on the refrigerant to lower the temperature from a high value, T_1 to a lower one, T_2. In the second stage heat is transferred to the system from a cold reservoir (the system is at a constant temperature, i.e. this process happens isothermally), then more isoentropic work is done on the refrigerant to increase its temperature back to T_1 before the cycle is completed through isothermal heat transfer away from the refrigerant to return the

system to the state in which it began. This process manipulates state variables V_1 and V_2 which are pairs of thermodynamic parameters such as pressure and volume or entropy and temperature.

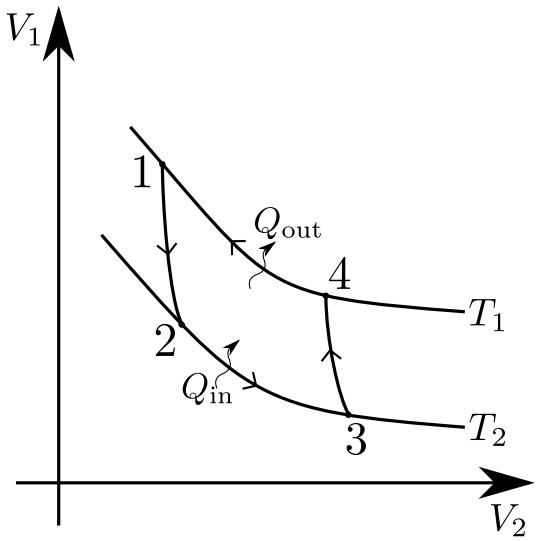

Figure 2.1: A Carnot cycle on state variables V_1 and V_2. Going from 1 to 2 is an isoentropic lowering of V_1. Moving from 2 to 3 heat is transferred isothermally (at constant temperature T_2) from the substance to be cooled to the refrigerant to increase V_2. From 3 to 4 isoentropic work increases V_1, then heat is transferred (at constant temperature T_1) from the refrigerant to the environment between 4 and 1 to return it to its original state. Adapted from [57]

In figure (2.1), the area under the cycle is the amount of heat exchanged between the refrigerant and the object it is cooling, the area inside the cycle is the amount of work done by the surroundings. The efficiency of the cooling cycle (the Carnot efficiency) is the ratio of the work done over the sum of the heat exchanged and the work done, i.e.:

$$\text{Efficiency} = \frac{T_1 - T_2}{T_1} = 1 - \frac{T_2}{T_1} \tag{2.1}$$

For a vapour compression system the first step is an isoentropic expansion of the vapour refrigerant lowering the pressure (one state variable, c.f. V_1 in figure (2.1)) and, as a side effect, its temperature. Heat applied to the refrigerant isothermally increases the volume (c.f. V_2 in figure (2.1)) of the vapour at a constant temperature. Isoentropic work done compresses the vapour, increasing the pressure to its original value and raising the temperature, finally excess heat is bled off to return the vapour to its former volume and the cycle is complete. This is

shown in the left hand side of figure (2.2).

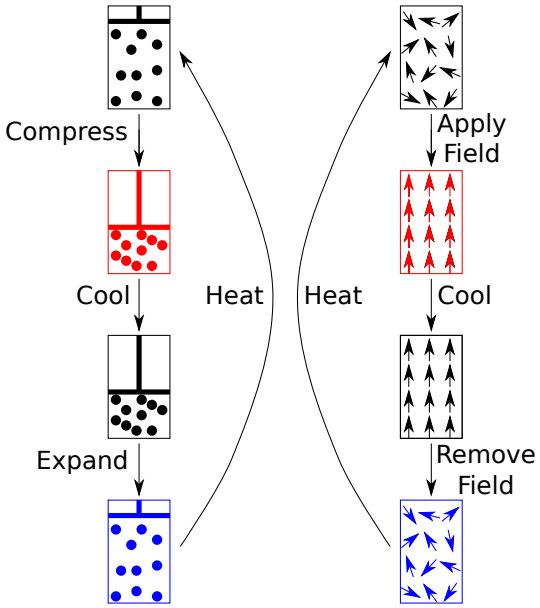

Figure 2.2: Vapour compression (on the left hand side) and electrocaloric (on the right hand side) cooling cycles for comparison where, in the first step, work is done to the refrigerant (compression in the case of vapour compression and application of an external field for electrocaloric), then heat is transferred away from the system. In the next step work is done in the opposite manner to before (expansion of the fluid or removal of the field), in the final step the refrigerant absorbs heat from the load to be cooled and the cycle is repeated.

Considering the electrocaloric cooling cycle (as seen in figure (2.3)) then where our state variables are electric field and polarisation rather than pressure and volume. If we apply an external field to increase the alignment of the electric dipoles (i.e. raise the polarisation) and therefore isothermally decrease the entropy of the dipoles, the lattice will increase its own entropy to compensate and therefore undergo an adiabatic temperature increase, then the next step of a cooling cycle is to release the excess heat to the environment. Removing the electric field causes a reduction in the polarisation as the dipoles disorder, the energy to disorder again is drawn from the lattice, thus there is an adiabatic temperature decrease as the dipolar entropy isothermally increases back to its original value. The refrigerant can then receive heat from the load to be cooled in order to return to its original temperature. The magnetocaloric effect is equivalent with simply magnetic dipoles replacing the electric dipoles, to keep the discussion general the dipoles shall henceforth be called spins as they will be treated as unit spins in our model.

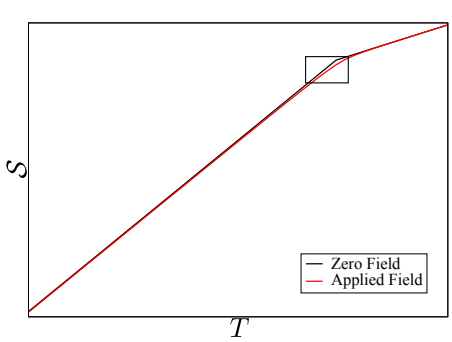

(a) The total entropy of a system with and without an applied field across a range of temperatures. The box is the region in figure (2.3b)

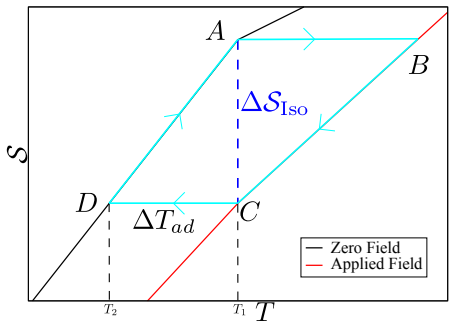

(b) A magnified view of the isothermal entropy and adiabatic temperature changes around a phase transition

Figure 2.3: Comparing the total entropy (lattice and dipolar) under an applied field and under zero field to see the $\Delta\mathcal{S}_{iso}$ and ΔT_{adi}. A cooling cycle happens in the following way: the refrigerant is at rest at A with temperature T_1 and entropy $\mathcal{S}_A$. An external field is applied, increasing the temperature to T_B at constant entropy. As the refrigerant equilibrates its temperature with the environment by releasing heat it moves from B to C returning to T_1, effectively having undergone $\Delta\mathcal{S}_{iso}$ reducing the entropy from $\mathcal{S}_A$ to $\mathcal{S}_C$. As the external field is removed, there is an adiabatic temperature change from T_1 to T_2 which is the cooling observed during the caloric effect. Heat is then absorbed from the load to be cooled to return the refrigerant to $\mathcal{S}_A$ and T_A. The largest entropy change occurs at the phase transition as there is a structural change at this temperature which causes a large change in polarisation which in turn causes a large entropy change.

2.3 Metrics of Performance

When comparing potential refrigerants it is important to have well defined metrics to ensure that the reader is clear about the claims made by an author and that different refrigerants may be directly compared and contrasted. One refrigerant may have a large adiabatic temperature change (ΔT_{adi}) with a very narrow peak while another may have a moderate cooling across a wide temperature range, both may require a large external field to produce their cooling relative to the small field required by a third refrigerant. The metrics of performance discussed in this section will allow us to examine the benefits of potential refrigerants.

The first measure of the strength of caloric effects we shall examine is the refrigerant capacity [58], defined as the adiabatic temperature change multiplied by the isothermal entropy change ($\Delta T_{adi}\Delta\mathcal{S}_{iso}$). In a reversible cycle, the isothermal

entropy changes at T_1 and T_2 must be equivalent and so, on a temperature-entropy graph (if, for example, temperature and entropy were the state variables V_1 and V_2 of figure (2.1)), the work done on the refrigerant is the area inside the cycle and is equal to $\Delta T_{adi}\Delta\mathcal{S}_{iso}$, the refrigerant capacity. This means that the refrigerant capacity can compare the relative cooling power (RCP) of an idealised system.

Some groups [59], [17] report a similar comparison measuring the value of the RCP where $RCP = \mathcal{S}_{\mathrm{Iso}}\delta T_{\mathrm{FWHM}\mathcal{S}_{\mathrm{Iso}}}$ measures the combination of the peak value of the isothermal entropy change and width of the entropy at half the of the peak value (the subscript FWHM being short for Full Width at Half Maximum). This allows reviewers to discriminate against sharp peaks in $\Delta\mathcal{S}_{iso}$ [60]. Reporting the peak $\Delta\mathcal{S}_{iso}$ may make it seem like a material has strong cooling power, but if this peak is highly localised then the RCP would be low, showing that the refrigerant would make for a poor practical device when compared to another refrigerant with a more distributed generally high $\Delta\mathcal{S}_{iso}$ and a higher RCP.

The relation $\frac{\Delta T_{adi}}{\Delta E}$ (also called the electrocaloric strength, c.f. the magnetocaloric strength for magnetocalorics [61]), gives a measure of the temperature change when compared to the change in strength of the external field, ΔE. While a large ΔT_{adi} is a clear figure of merit to a cooling cycle, if these are achieved only at the expense of a large applied field then the refrigerant needs a larger energy input than a refrigerant which possibly leads to a smaller ΔT_{adi} but does not require as large a field. Results of $\frac{\Delta T_{adi}}{\Delta E}$ remove any dependence on experimental variables [3] and report a measure of the intrinsic properties of an electrocaloric material. This figure should, however, be be treated with caution when considering practical cooling cycles as a refrigerant with large $\frac{\Delta T_{adi}}{\Delta E}$ but a small electric breakdown strength (see section (1.5)) would mean that it is not possible to take full advantage of this large intrinsic effect to produce a powerful cooling cycle.

Another important number for consideration in practical cooling cycles is the coefficient of performance (COP) [21], a value equal to the cooling power over the input power. This represents the efficiency of a system in practice, including all losses to a hysteresis cycle (section (3.4)), Joule heating in the system from leakage currents, etc. The importance of this measurement is that, combined with the Carnot efficiency (see section (2.2)) we get a total measure of the possible cooling power of the system, the headline (technical) efficiency.

Clearly, only using the Carnot efficiency means that whichever materials have a large operating window (the range of temperatures at which the refrigerant can undergo a caloric effect) would be considered to be the ideal candidates for a refrigerant. On the other hand, comparing only the COP means whichever system

loses as little energy as possible from hysteresis or leakage currents (so, those closest to their Carnot efficiency) would be deemed the best refrigerants.

With a combination of the COP and $\frac{\Delta T}{\Delta E}$, we can compare and contrast different refrigerants to observe what qualities and properties distinguish refrigerants that have high COP and $\frac{\Delta T}{\Delta E}$, leading to an informed decision about new refrigerants to trial and how it may be possible to improve the strength of the electrocaloric effect in materials with high electric breakdown strength but weaker COP and $\frac{\Delta T}{\Delta E}$. For example, a 55-45 mix of the polymer P(VDF-TrFE) has a similar $\frac{\Delta T}{\Delta E}$ to $PbSc_{0.5}Ta_{0.5}O_3$ (0.006 - 0.008 K cm kV^{-1}, respectively), but due to the high dielectric strength of the polymer a larger ΔT can be obtained (12.6 K compared to 6.2 K), thus an examination of the COP would be of interest to determine whether the extra energy input to create the larger ΔT is justified. Similarly $PbZr_{0.95}Ti_{0.05}O_3$ has an equivalent ΔT to P(VDF-TrFE) (12 - 12.6 K, respectively), but nearly three times as large a $\frac{\Delta T}{\Delta E}$ (0.015 - 0.006 K cm kV^{-1}). An investigation into the COP of both would determine whether this advantage is sustained in a repeated cycle. It should be noted that the different Curie temperatures of these materials (495 K, 353 K and 341 K for $PbZr_{0.95}Ti_{0.05}O_3$, P(VDF-TrFE) and $PbSc_{0.5}Ta_{0.5}O_3$ respectively) offers an alternative reason why one material might be preferred to another, in this case.

By comparing headline efficiencies we can directly compare the total cooling power of refrigerants. Simulations suggest that cooling systems based on materials with a large electrocaloric effect can have higher COPs ($>$ 60% of Carnot efficiency [24]) than conventional vapour compression refrigerants [3], suggesting that cooling systems based on the electrocaloric effect can, indeed, produce more energy efficient refrigeration.

2.4 The Maxwell Relations

As described in section (2.2) a caloric cooling cycle comes about due to the application of an external force, in the case of the electrocaloric effect it is an external electric field acting on the electric dipoles of the system that leads to an isothermal entropy change ($\Delta\mathcal{S}_{iso}$). The field encourages increased polarisation (alignment of the electric dipoles) in the material thus decreasing their entropy.

In order to counter this decrease in dipolar entropy the material will increase its entropy by generating more and higher frequency lattice vibrational modes [62], having the side effect of increasing the temperature of the material. This means that with no net change in entropy the system has undergone an adiabatic temperature change, ΔT_{adi} [62]

To obtain a description of these processes we specify the free energy of the system:

$$F = (U - T\mathcal{S}) - \left(\vec{E} \cdot \vec{P}\right) \tag{2.2}$$

where U is the internal energy of the system, T is the temperature, $\mathcal{S}$ is the entropy, $\vec{E}$ is an externally applied field and $\vec{P}$ is the value of the polarization of the system.

From equation (2.2) taking the polarisation and external field to be aligned in the same direction direction (therefore treating them as scalars) and by assuming that all quantities are continuous across the phase transition (i.e. that the phase transition is second order rather than first order), it is possible to derive the following Maxwell relations

$$\left.\frac{\partial F}{\partial E}\right|_T = -P \tag{2.3}$$

and

$$\left.\frac{\partial \mathcal{S}}{\partial E}\right|_T = \left.\frac{\partial P}{\partial T}\right|_E \tag{2.4}$$

Equation (2.4) can be integrated [18] to give an indirect value of $\Delta\mathcal{S}_{iso}$ from

$$\Delta\mathcal{S}_{iso} = \int_{E_1}^{E_2} \left.\frac{\partial P}{\partial T}\right|_{E'} dE' \tag{2.5}$$

where E_1, E_2 are the initial and final applied field strengths and E' is a variable to integrate over.

The heat capacity is a measure of how much energy must be transferred to (or from) the system in order for its temperature to increase (or decrease). A material with a high heat capacity can absorb a large amount of energy with only small variation in its temperature, while a material with a low heat capacity may have large temperature variations for only small energy exchange. The heat capacity at constant volume can be expressed as a function of entropy and temperature by

$$C_v = T\left(\frac{\partial \mathcal{S}}{\partial T}\right)_v \tag{2.6}$$

For small variations in entropy and temperature $(\Delta\mathcal{S}, \Delta T)$ it is possible [21] to estimate ΔT_{adi}

$$C_v \approx T\frac{\Delta\mathcal{S}}{\Delta T} \tag{2.7}$$

$$\Rightarrow \Delta T \approx T\frac{\Delta\mathcal{S}}{C_v} \tag{2.8}$$

This approach makes assumptions on continuity that are justified solely for continuous, second order phase transitions. However if, for discontinuous, first order phase transitions, the change in polarisation is sufficiently small then the relation can be used to approximate the true value of ΔT_{adi} [63]. This approach may also work well in disordered broadened transitions associated with the polymer relaxor ferroelectrics in which we are interested (see section (1.5)).

While the Maxwell equations give a handle on the electrocaloric effect there are concerns that, due to the assumptions of an ergodic system in their derivation [10] and the fact that relaxor ferroelectrics are not ergodic below their freezing temperature (see section (1.4)), the Maxwell relations may not be valid for describing relaxor ferroelectrics. They also only give a basic estimation of the direct electrocaloric effect but do not consider the secondary effect which comes from the strain imposed by the external electric field and the corresponding change in temperature due to the reverse piezoelectric effect [3] (where a mechanical strain is induced by an applied electric field). Furthermore, the Maxwell relations are unable to differentiate between refrigerants that have different microscopic properties and are therefore unable to determine the effect that the substitution of a new chemical into the refrigerant would have. Due to this we shall look to develop a microscopic theory for the electrocaloric effect based on statistical mechanics so that we may create a model building from the dipoles assigned to the localised polar nano regions.

Chapter 3

The Statistical Mechanics of a Cooling Cycle

3.1 Introduction to Statistical Mechanics

While the Maxwell relations give an estimate of the strength of the electrocaloric effect, they offer no ability to change any parameters to get variations of the strength of the effect in different materials. Statistical mechanics deals with probabilities and the average behaviour of a large system, and it is possible to create a more flexible description of the microscopic causes behind the various caloric effects.

This chapter shall investigate the statistical ensemble of a caloric refrigerant, describe how phase transitions may be discontinuous in the order parameter (a measure of the ordering of the dipolar spins in our system) and first order or continuous and second order. It will examine the losses from hysteresis associated with a first order phase transition, describe a general caloric effect in the language of statistical mechanics, explain the lattice contribution to the effect and the relation between $\Delta\mathcal{S}_{iso}$ and ΔT_{adi}. Finally the application of mean field theory to the electrocaloric effect will be used to set up a system where it is possible to investigate tuning the phase transition to maximise $\Delta\mathcal{S}_{iso}$ at a minimum hysteresis loss through repeated cooling cycles.

3.2 The Canonical Ensemble

In this section we shall describe a generic spin system to illustrate the statistical mechanics of an system of interacting electric dipoles and to allow us to investigate its phase transition. The full electrocaloric effect requires the consideration of

lattice vibrations too and these shall be considered in section (3.8). The canonical ensemble is a statistical ensemble that represents states of a system fixed at a given temperature due to contact with an external thermal reservoir.

For simplicity we shall initially consider only a pure spin system and write the Helmholtz free energy (using the canonical partition function, Z) as

$$F = -k_B T \ln(Z), \tag{3.1}$$

where Z can be described from the inverse temperature $\left(\beta = (k_B T)^{-1}\right)$ - k_B is Boltzmann's constant. We also need to use the Hamiltonian $\left(H_{\{\vec{S}_i\}}\right)$ of a given state $\left\{\vec{S}_i\right\}$, we can then write

$$Z = \sum_{\{\vec{S}_i\}} e^{-\beta H_{\{\vec{S}_i\}}}. \tag{3.2}$$

The Hamiltonian can be described in generality by interactions with an externally applied field ($\vec{E}$) and from different levels of coupling between elements (i.e. spins, $\vec{S}_i$) of the system such as interactions with on site fields, pairwise interactions, interaction between three elements and so on through higher order terms ($H.O.T.$).

$$H_{\{\vec{S}_i\}} = -\sum_i \vec{h}_i \cdot \vec{S}_i - \frac{1}{2}\sum_{i,j} J_{i,j}\vec{S}_i \cdot \vec{S}_j - \cdots H.O.T. + \cdots - \vec{E} \cdot \sum_i \vec{S}_i, \tag{3.3}$$

We may use the partition function and the Hamiltonian to define the probability $\left(\mathcal{P}_{\{\vec{S}_i\}}\right)$ that the system is in state $\left\{\vec{S}_i\right\}$ as

$$\mathcal{P}_{\{\vec{S}_i\}} = \frac{1}{Z} e^{-\beta H_{\{\vec{S}_i\}}} \tag{3.4}$$

which is simply the Boltzmann distribution. Knowing the probability of given states means we can determine the polarisation of a given site L

$$\vec{P}_L = \sum_{\{\vec{S}_i\}} \vec{S}_L \mathcal{P}_{\{\vec{S}_i\}} \tag{3.5}$$

This makes sense as it is the average value of the spin on site L. Note that if this value is the same on every site then we recover the order parameter from section (2.4), i.e.

$$\vec{P} = \sum_{L} \vec{P}_L \tag{3.6}$$

If we now define, as is convention, U to be the internal energy of the system, $\vec{E}$ as our external field, T is the temperature and $\mathcal{S}$ is the entropy we can describe the Helmholtz free energy

$$F = \sum_{\{\vec{S}_i\}} \mathcal{P}_{\{\vec{S}_i\}} H_{\{\vec{S}_i\}} + k_B T \sum_{\{\vec{S}_i\}} \mathcal{P}_{\{\vec{S}_i\}} \ln\left(\mathcal{P}_{\{\vec{S}_i\}}\right) \tag{3.7}$$

$$\equiv U - \vec{E} \cdot \vec{P} - T\mathcal{S} \tag{3.8}$$

This result is the same as that derived using variational methods in equation (3.37).

Comparing equations (3.7) and (3.8) it can be seen that

$$U - \vec{E} \cdot \vec{P} = \sum_{\{\vec{S}_i\}} \mathcal{P}_{\{\vec{S}_i\}} H_{\{\vec{S}_i\}} \tag{3.9}$$

$$\mathcal{S} = -k_B \sum_{\{\vec{S}_i\}} \mathcal{P}_{\{\vec{S}_i\}} \ln\left(\mathcal{P}_{\{\vec{S}_i\}}\right) \tag{3.10}$$

We can see that equation (3.9) makes sense as the left hand side is simply the internal energy and interaction of the spins of the system with an external field and the right hand side gives the sum of the the energy for all possible states, each weighted by their probability. While equation (3.10) is the familiar form for the entropy.

With the formalism in place to describe the polarisation, free energy and entropy of the system, it would be instructive to look at where maximum changes in entropy and thus temperature occur during a caloric cooling cycle and so the next section shall describe phase transitions and the theory behind them.

3.3 Landau-Ginzburg-Devonshire Theory

Landau theory [64] is used to describe second order phase transitions in generality, in such transitions one observes how the order parameter varies continuously from non-zero at low temperatures phase to zero at high temperatures. Devonshire [65] derived a theory of a similar nature to that of Landau's work to describe the ferroelectric phase transition in barium titanate. The Devonshire theory extended Landau theory

to a first order system. Ginzburg and Landau [66] created a formalism to describe superconductivity, they added terms in the derivative of the order parameter to the original Landau theory and when such terms are included in a theory of ferroelectrics they can be used to describe features such as domain walls [67], thus the general theory to describe phase transitions in a ferroelectric would be the Landau-Ginzburg-Devonshire theory.

The Landau-Ginzburg-Devonshire formalism expands the free energy (F or F_0 at zero ordering), as a power series of the order parameter (P) multiplied by Landau parameters [57] (a, b and c are the first, second and third Landau parameters respectively [41]) and E is the applied electric field. This demonstrated in equation (3.11).

$$F = F_0 + aP^2 + bP^4 + cP^6 + \cdots - EP \tag{3.11}$$

here we have assumed the order parameter and applied field are uniaxial vectors oriented in the same direction so we are only interested in their magnitude, $\left|\vec{P}\right| = P$. We also only have even powers of the order parameter as, for ferroelectric and antiferroelectric systems, the order parameter is symmetric under reversal of direction - all aligned in a given direction is equivalent to all aligned in the opposite direction.

Simplistically, the macroscopic phase of our system can be ferroelectric, antiferroelectric or paraelectric depending on whether the system preferentially aligns, anti-aligns or has no preferred alignment. The order parameter takes the value zero in a disordered, paraelectric phase, this rises to a non-zero value as the material transitions to an ordered phase. For example, the polarisation of a ferroelectric can be used as an order parameter (and, indeed, that will be the order parameter used in chapter (4)), the polarisation is at a maximum when at a low temperature in the ferroelectric regime and all dipoles are fully aligned in the same direction and decreases to zero as the material transitions to the paraelectric regime.

The dipoles talked about in this thesis are not the smallest dipoles in the system, individual electric dipoles created due to charge separation in a unit cell, but are domains of dipoles, the product of multiple dipoles being strongly attracted and oriented in the same direction as one domain.

The order parameter for an antiferroelectric material is simply the staggered polarisation of the material. The staggered polarisation takes two sublattices with equal and opposite (in zero field) polarisations, if these sublattices interleave each other in a chequerboard fashion then for each site on sublattice 1 (with polarisation P_1), its nearest neighbours are on sublattice 2 and are oppositely aligned to it (with polarisation P_2) and vice versa. Thus, the free energy can simply be calculated by

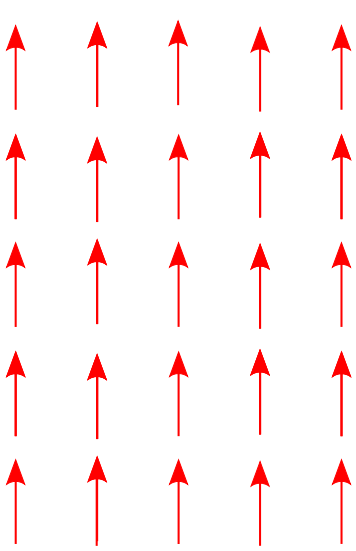

(a) A lattice with ferroelectric ordering. This perfectly ordered lattice would have a ferroelectric order parameter of 1.

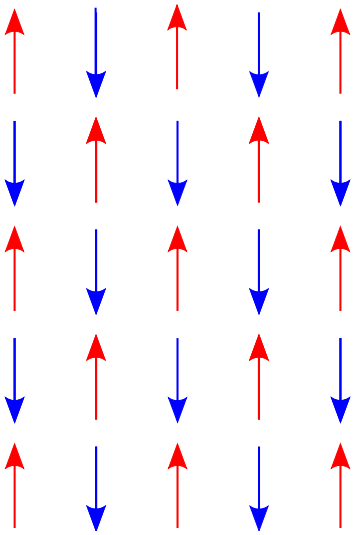

(b) A lattice with antiferroelectric ordering. This perfectly ordered (but anti-aligned) lattice would have an anti-ferroelectric order parameter of 1 but a ferroelectric order parameter of 0.

Figure 3.1: Two dimensional lattice orderings

determining $P = P_1 - P_2$ - the antiferroelectric order parameter - and substituting into equation (3.11).

The polarisation of the system is determined by the global minimum of the free energy, whichever value of polarisation minimises the free energy is the polarisation that the system relaxes into. As the landscape evolves with temperature and the minima and maxima change in size and location, what was once a global minimum may become only a local minimum or even no longer a minimum at all and the system will pass from one phase to another via a phase transition. As seen in figures (3.2) and (3.3) these can either be a continuous (in the order parameter) second order transition or a discontinuous (in the order parameter) first order transition.

We shall first look for second order transitions in no external field, for this we only require the first three terms of the free energy, so let us examine the derivative of F to determine where the free energy minima are:

$$\frac{\partial F}{\partial P} = 2aP + 4bP^3 \tag{3.12}$$

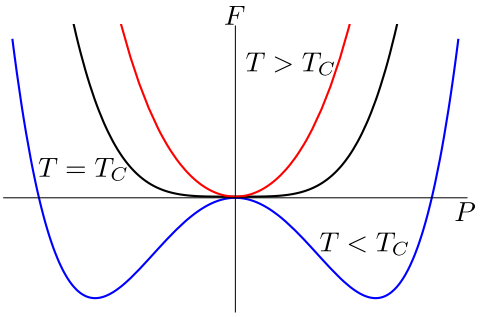

(a) The free energy landscape changing through a second order transition

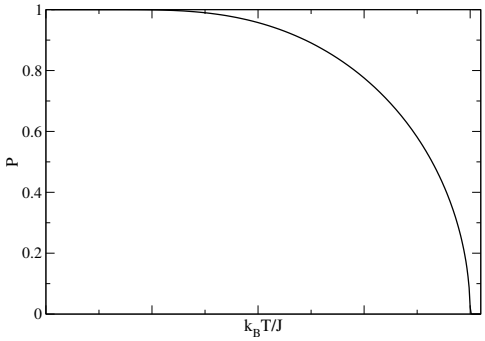

(b) The order parameter P as a function of temperature

Figure 3.2: In the left hand image, the free energy of a system as a function of polarisation at various temperatures through a second order (ferroelectric) transition. Three temperatures are represented, one below the transition temperature (the blue line), one at the transition temperature (black line), one above the transition temperature (red line). This shows how the two minima below the Curie temperature meet at 0 polarisation at the Curie temperature (as the system goes from polarised to unpolarised) and the global minimum of free energy remains at 0 polarisation about the Curie Temperature. In the right hand image we see the order parameter (i.e. the polarisation) undergo a continuous, second order transition as a function of temperature.

This has a minimum when $\frac{\partial F}{\partial P} = 0$ when is when either

$$P = 0 \qquad \text{or} \qquad P^2 = -\frac{a}{2b} \tag{3.13}$$

To classify these as minima or maxima we shall look at the second derivative

$$\frac{\partial^2 F}{\partial P^2} = 2a + 12bP^2 \tag{3.14}$$

For $P = 0$ this gives a second derivative equal to $2a$, which means that $P = 0$ is a minimum for $a > 0$ and a maximum for $a < 0$, so below T_C we want $a < 0$ and above T_C we want $a > 0$, let us make the assumption [68] that

$$a = a_0(T - T_c) \tag{3.15}$$

where a_0 is a constant and T_c is the critical, transition temperature.

For $P \neq 0$, we get

$$\frac{\partial^2 F}{\partial P^2} = 2a - 6a \qquad = -4a \tag{3.16}$$

With the definition of a from equation (3.15) this makes $P \neq 0$ a minimum for $T < T_C$ as required.

This analysis relies on the assumption that $b > 0$ otherwise equation (3.13) yields an imaginary value of P. In the case that $b < 0$ we must head to higher order terms and require $c > 0$ in order to have turning points at $P \neq 0$. The case of $b < 0$ creates a first order phase transition as seen in figure (3.3).

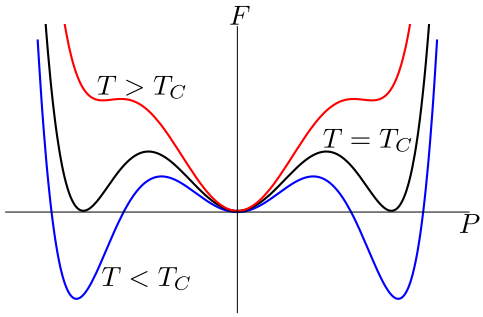

(a) The free energy landscape changing through a first order transition

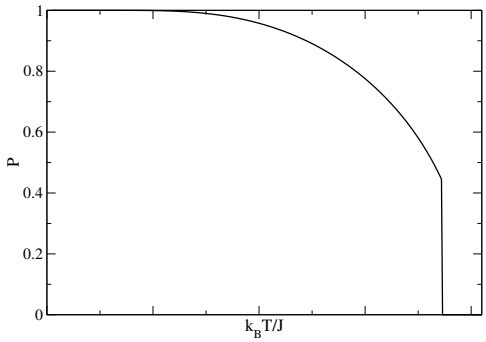

(b) The order parameter P as a function of temperature

Figure 3.3: In the left hand image is the free energy of a system travelling through a first order transition as a function of polarisation. Three temperatures are represented, one below the transition temperature (the blue line), one at the transition temperature (black line), one above the transition temperature (red line). This shows how there exist minima in the free energy which are not the global minimum (for example at 0 polarisation below the transition temperature and at non-zero polarisation at the transition temperature). It is the existence of these global minima which cause the discontinuous change in polarisation from non-zero to zero as they do not merge together at zero polarisation as was found in the second order transition case but they remain at non-zero values until they cease to be minima and the polarization which was trapped in a well now relaxes to the global minimum at zero. In the right hand image we see the order parameter of a first order transition.

In this situation we must redefine a

$$a = a_0(T - T_0) \tag{3.17}$$

where T_0 is a temperature that is not the transition temperature.

We shall again look at the derivative of the free energy, this time including the term with the third Landau parameter

$$\frac{\partial F}{\partial P} = 2aP + 4bP^3 + 6cP^5 \tag{3.18}$$

$$\tag{3.19}$$

Again, this has a minimum when $\frac{\partial F}{\partial P} = 0$, with solutions

$$P = 0 \qquad \text{or} \qquad P^2 = -4b \pm \frac{\sqrt{b^2 - 3ca}}{3c} \tag{3.20}$$

The system can be manipulated through changing the value of the second landau parameter to display second order transitions (when $b > 0$) or first order transitions ($b < 0$), these separate behaviours meet at a tricritical point where $a = b = 0$.

The second order transitions are seen to have lower hysteresis losses than first order transitions, while first order transitions have larger entropy changes than second order transitions. This can be explained by the change in order parameter between the paraelectric and ferroelectric phase. In the ferroelectric phase there is a non-zero order parameter, while in the paraelectric phase (in the absence of an external field) the order parameter is zero. Second order transitions vary continuously between the zero and non-zero order parameter, while first order transitions have a discontinuous change. A larger change in polarisation results in a larger change in entropy of the system which is why first order transitions exhibit larger entropy changes. However, the large change in polarisation is due to the motion of walls between ferroelectric domains and the energy costs required to cause this movement take away from the total energy applied to the system through the external field and reduce the energy used in the cooling cycle.

Figure (3.4) shows how it is possible to manipulate a system to change the transition temperature between phases, by moving across the phase diagram of the material we may reach a point where second and first order transitions meet and here we would find a tricritical point.

If the system can be tuned to a tricritical point, it can have a large entropy jump (associated with a large change in P), as exhibited in a first order transition, but simultaneously minimise the hysteresis losses [62] as observed in second order

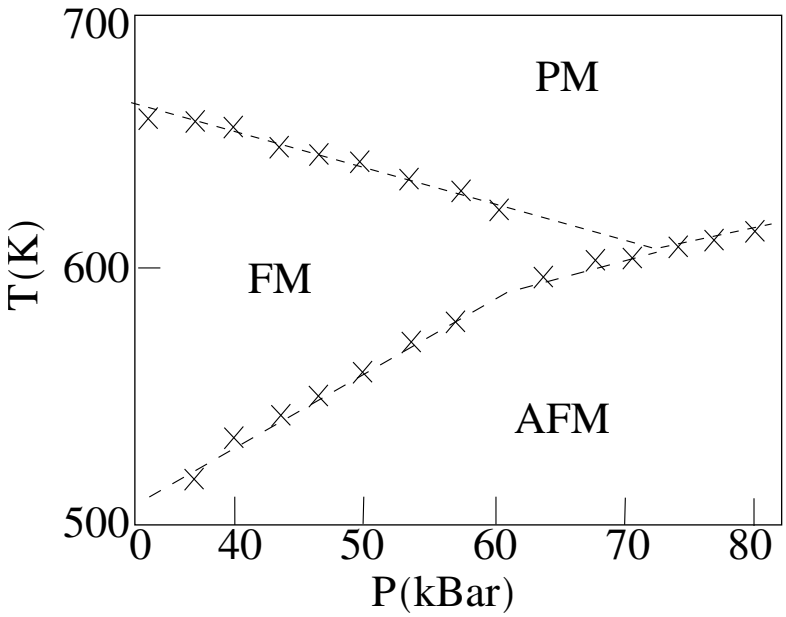

Figure 3.4: A two-dimensional phase diagram of iron rhodium (FeRh, a material that shall be studied in this thesis) showing how varying pressure and temperature may lead this material through ferromagnetic (FM), antiferromagnetic (AFM) or paramagnetic (PM) phases. Adapted from [69]

transitions. This would be the ideal electrocaloric.

3.4 Hysteresis Cycles and Hysteresis Losses

As stated in section (1.3), hysteresis is the effect observed when there is a delay in response from a system with respect to an external stimulus. Domain walls are the cause of hysteresis in a ferroelectric and this explains why no hysteresis is observed in a paraelectric which is free of ferroelectric domains.

A paraelectric system shows no hysteresis, freely aligning itself with an externally applied field instantly, whereas a ferroelectric system has an intrinsic polarisation before the application of the external field. Should the field point antiparallel to this polarisation, the polarisation will not immediately align with the field but there will be a delay until the field is sufficiently large before the polarisation aligns with field as shown previously in figure (1.1) [14] and represented again in figures (3.5a), (3.5b).

Remembering figure (1.1) [14] and looking now at figures (3.5a), (3.5b), we observe that if a ferroelectric material is in a sufficiently large external field (we shall define that the direction in which the field is initially oriented is the $+Z$ direction

for the sake of a reference orientation) then the ferroelectric will be fully polarised in the same direction. This means that all electric dipoles will be oriented in the same direction.

From this starting point, gradually decreasing the field decreases the polarisation as the dipoles begin to relax into their preferred orientation. There are local regions of dipoles, known as domains, where the dipoles will all preferentially align with each other and between neighbouring domains with non-aligned orientations is a domain wall. The initial large electric field overcomes these domain walls and forces all dipoles to be aligned. As the field is removed the dipoles relax and domains with different orientation begin to appear and energy is lost into the system in the creation and movement of the domain walls separating these domains. As the system is a ferroelectric rather than a paraelectric, there will still be a net polarisation, even at zero field and this is due to enough domains having sufficiently similar electric orientations that they produce a net polarisation. Thus in the hysteresis curve we observe that at zero field there is now a residual, intrinsic polarisation P_S.

Should the external field now begin to increase in magnitude in the $-Z$ direction, the polarisation will decrease in value until the field strength reaches a value called the coercive field, E_C where the polarisation again returns to zero. In a relaxor ferroelectric, the domains are isolated polar nano-regions embedded in a matrix of non-polarised material, thus we do not have the same domain wall motion as experienced in a true ferroelectric. This leads to lower values of a coercive field and thinner hysteresis graphs observed than in a pure ferroelectric as less energy is lost to the domain wall motion.

When the field strength increases beyond E_C, the polarisation reverses direction and rapidly increases in magnitude as the domain walls move and individual dipoles align along the imposed orientation until the polarisation saturates as before.

Decreasing the strength of the field to zero results in a residual polarisation of equivalent strength but in the opposite direction to before. Increasing field strength in the $+Z$ direction results in 0 polarisation at the value of the coercive field again before the polarisation increases superlinearly to saturation.

The hysteresis loss [70] (as seen in figure (3.5)) is simply the difference between the energy required to reverse the internal polarisation of the material and the energy reclaimed from the material as it responds to a reduction in external field.

It is important to avoid the loss associated with the hysteresis effect which is found in first order transitions but is absent in second order transitions [18].

We now have a qualitative handle on the physics behind phase transitions

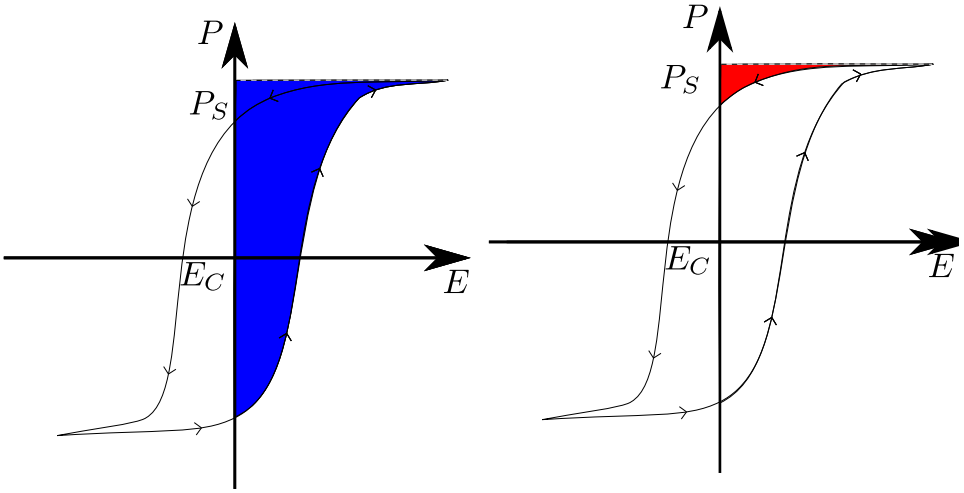

(a) Energy used to establish the field

(b) Energy released by collapse of the field

Figure 3.5: The total amount of energy needed to polarise the material is represented by the area inside the hysteresis loop and the area above it up to the maximum value of polarisation. The energy reclaimed is the area outside the hysteresis loop up to the maximum polarisation. The energy represented by the area inside the hysteresis loop is lost in the cycle.

and caloric effects, but we need to create a model with predictive power before we can test this understanding and make progress in our research. The next section will deal with creating models of caloric effects.

3.5 Mean Field Theories

A realistic model Hamiltonian of a system may be sufficiently complex that it is impractical or even impossible to solve it exactly. Indeed, even a simple system with pairwise interactions may prove too challenging to solve exactly for sufficiently many interactions of varying strength (for example there exists no exact solution for the n-body problem for $n > 3$). There are two possible solutions to the issue of a complex Hamiltonian, create a simpler Hamiltonian and observe it analytically, or attempt to solve the complex Hamiltonian with numerics. The purpose of this project was to create a simplistic model that would give at least a qualitative handle on caloric effects. To that end we make the use of a simplified method which keeps the key features of a system but renders it soluble rather than using the equally valid alternative approach of finding numerical solutions to a complex Hamiltonian.

A mean field theory is the simplifying method we chose; rather than exam-

ining all of the interactions of each spin with every other spin on the lattice we simply examine the interactions of that spin with the Weiss field (also called the mean field) generated by other spins [71]. We illustrate this with the Hamiltonian of equation (3.3) which contains only pairwise interactions

$$H = -\frac{1}{2}\sum_{i,j} J_{ij}\vec{S}_i \cdot \vec{S}_j - \sum_i \vec{E} \cdot \vec{S}_i \tag{3.21}$$

The sum is over pairs of spins i, j and the factor of a half removes the issue of double counting over the N sites in the sum; J_{ij} is the interaction between the spins on sites i and j [72]; $\vec{S}_i$ is the polarisation (magnitude and direction) of the spin on site i and $\vec{E}$ is the externally applied field. For the sake of this derivation we shall assume that J_{ij} is positive for all i, j and thus we are examining a ferroelectric material where the free energy is minimised by all spins being aligned.

We can make the approximation that

$$H_{mf} = -\sum_{i=1}^{N} \vec{h} \cdot \vec{S}_i \tag{3.22}$$

where $\vec{h}$ is our effective Weiss field, defined by

$$\vec{h} = \sum_{k=1}^{N} J_{ik}\vec{P} + \vec{E} \qquad = h\hat{n} \tag{3.23}$$

with $\vec{P}$ being the order parameter of the system, the same on every site (i.e. it describes a homogeneous ferroelectric system), h is simply the magnitude of the Weiss field oriented in the direction of the unit vector $\hat{n}$ (this is used to aid bookkeeping in the mathematics further down the line). The partition function of the 3D Ising model (see section (3.2)) for (potentially) multiple Weiss fields, labelled L, is given by

$$Z = \sum_{\{\vec{S}_i\}} e^{-\beta H_{mf,\{\vec{S}_i\}}} \qquad = \prod_L \left(\frac{4\pi \sinh\left(h_L\beta\right)}{h_L\beta} \right) \tag{3.24}$$

The partition function allows the probability of the system being in a given state to be determined from equation (3.4) which then allows the order parameter to be calculated using equation (3.9)

$$\vec{P} = \frac{\int \vec{S} e^{\beta h \hat{n} \cdot \vec{S}} d\vec{S}}{\int e^{\beta h \hat{n} \cdot \vec{S}} d\vec{S}} \qquad = \left(\coth(\beta h) - \frac{1}{h\beta} \right) \hat{n} \tag{3.25}$$

$\vec{P}$ is oriented in the direction of $\hat{n}$. Recalling the effective field from equation (3.23) and combining it with equation (3.25)

$$\left| \vec{P}_i \right| = \coth \left| \beta \vec{E} + \beta \sum_{k=1}^{N} J_{ik} \vec{P} \right| - \frac{1}{\left| \beta \vec{E} + \beta \sum\limits_{k=1}^{N} J_{ik} \vec{P} \right|} \tag{3.26}$$

Equation (3.26) is a transcendental equation which can be solved either numerically (via an iterative method) or graphically as seen (for the case where $\vec{E} = 0$) in figure (3.6).

At low temperatures there are multiple possible solutions $P = \pm P^*$ (where P^* is the absolute value of the solution) and $P = 0$ but there is a critical point at the critical temperature $T = T_C$ where the three solutions for the order parameter converge at 0. At this critical temperature there is a phase transition from an ordered state to a disordered state. As $T \to T_C$ it is clear that $\vec{P} \to 0$, so given the Taylor expansion for coth

$$\coth(x) \approx \frac{1}{x} + \frac{x}{3} - \frac{x^3}{45} + \cdots \tag{3.27}$$

This means that for small $\left| \vec{P} \right|$ in zero field

$$\left| \vec{P} \right| = \frac{1}{\left| \beta \sum\limits_{k=1}^{N} J_{ik} \vec{P} \right|} + \frac{\left| \beta \sum\limits_{k=1}^{N} J_{ik} \vec{P} \right|}{3} - \frac{1}{\left| \beta \sum\limits_{k=1}^{N} J_{ik} \vec{P} \right|} \tag{3.28}$$

$$\Rightarrow 3 \approx \frac{\sum\limits_{k=1}^{N} J_{ik}}{k_B T_C} \tag{3.29}$$

$$\Rightarrow T_C \approx \frac{\sum\limits_{k=1}^{N} J_{ik}}{3 k_B} \tag{3.30}$$

This can be seen graphically, as in Figure (3.6) we see that there becomes a

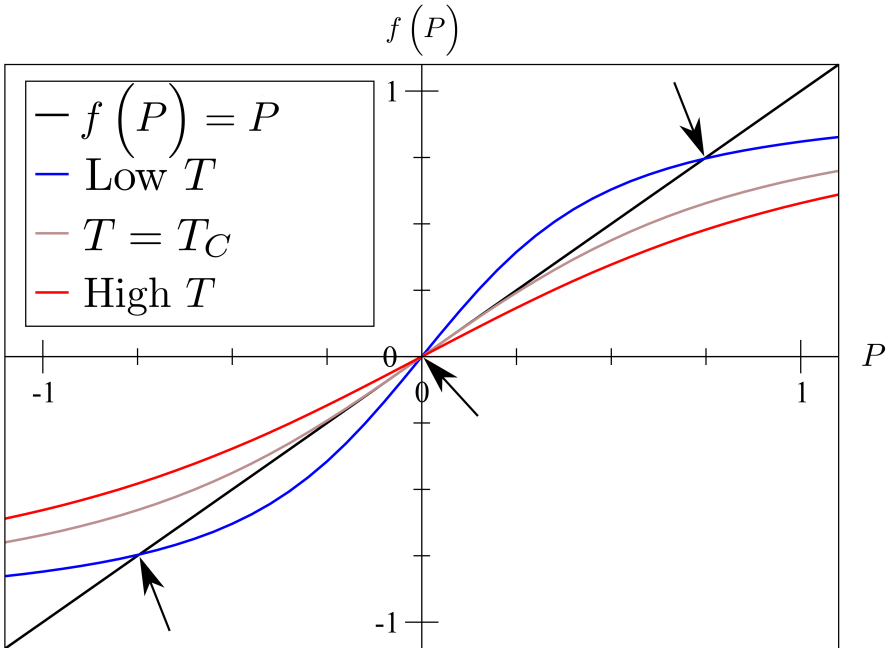

Figure 3.6: A plot showing how the polarisation may be determined in zero field for three temperatures, below T_C (the blue line), at T_C (the brown line) and above T_C (the red line). The polarisation is determined by the intersection of $f(P) = \coth\left(\beta \sum_{k=1}^{N} J_{ik}P\right) - \dfrac{1}{\beta \sum_{k=1}^{N} J_{ik}P}$ with $f(P) = P$, where $P = \pm\left|\vec{P}\right|$ for the sake of symmetry, these intersection points are marked by arrows and are values of polarisation of the global minima of the free energy landscape seen in section (3.3). We have assumed that the lattice is homogeneous and, thus, all values of P are the same for each site. For low temperatures (high β) there are three distinct intersection points representing the values of P which satisfy the equation (3.26), equivalent positive and negative polarisation and a polarisation of 0. As the temperature increases to T_C the three intersection points meet at 0. Above T_C, the only intersection point is at $P = 0$. Note that this value of T_C is the one predicted by mean field theory, as that is what has been applied to create this graph

critical point (in 2D) when

$$T_c = \frac{\sum_{k=1}^{N} J_{ik}}{3k_B} \tag{3.31}$$

it should be noted that this is a mean field assumption and not an exact critical temperature.

Our use of mean field theory will allow us easy access to both the free energy and the entropy of the system as they can be calculated as functions of only polarization and temperature, we shall show how in the following section.

3.6 Variational Methods

The working in the previous section is trivial to follow in the case of a homogeneous lattice where our assumption of the simple Weiss field being equivalent for every lattice site is valid. Should a more challenging system be investigated however, even something as common place as an antiferroelectric system where the order parameter alternates between value $\vec{P}_1$ and $\vec{P}_2$ on neighbouring lattice sites, it would be necessary to find a more general approach to determine multiple the Weiss fields. As such the Feynman-Peierls inequality [73] can be used to determine what the maximum allowed value of free energy of a general system described by the complex Hamiltonian H is by reference to a simpler system

$$F \leq F_0 + \langle H - H_0 \rangle = \tilde{F} \tag{3.32}$$

For the reference Hamiltonian

$$H_0 = -\sum_i \vec{h}_i \cdot \vec{S}_i \tag{3.33}$$

where the set of $\left\{\vec{h}_i\right\}$ are the Weiss fields to be found. We can write

$$F_0 = -k_B T \ln\left(\prod_L \left(\frac{4\pi \sinh\left(h_L\beta\right)}{h_L\beta}\right)\right) \tag{3.34}$$

$$H = -\frac{1}{2}\sum_{ij} J_{ij}\vec{S}_i \cdot \vec{S}_j - \sum_{i,j,k} \vec{K}_{i,j,k} \cdot \vec{S}_i\vec{S}_j\vec{S}_k + \cdots - \sum_i \vec{E} \cdot \vec{S}_i \tag{3.35}$$

where the spins of equation (3.35) become order parameters under averaging. From equation (3.7) we shall define that

$$\tilde{F} = \langle H \rangle - T \langle \mathcal{S} \rangle \tag{3.36}$$

where $\langle H \rangle$ is an ensemble average over the system specified by the simpler reference Hamiltonian, thus the orientation of individual spins are averaged over to give the polarisation of different domains, $\vec{P}_i$. This means (using the full generality of equation (3.3)) we can write

$$\begin{aligned} \tilde{F} = -\frac{1}{2} \sum_{ij} J_{ij} \vec{P}_i \cdot \vec{P}_j + \cdots + \sum_i \vec{h}_i \cdot \vec{P}_i - \sum_i \vec{E} \cdot \vec{P}_i \\ - k_B T \ln \left(\prod_i \left(\frac{4\pi \sinh (h_i \beta)}{h_i \beta} \right) \right) \end{aligned} \tag{3.37}$$

where the first term is the pairwise interaction of electric domains with different polarisation, higher order terms of interaction between domains are subsumed into the ellipses. The second term is the expression of the domains interacting with the Weiss fields, the third is the interaction of domains with the external field and the final term is the temperature of the system multiplied by the entropy. This result is equivalent to the one found in equation (3.7) and the polarisation can be determined by equation (3.5). The internal energy is expressed by the first term and the ellipses, $\vec{E} \cdot \vec{P}$ is the second term and the third and final terms give $T\mathcal{S}$.

The indices on the order parameter explicitly show that different sites may have different spins but these spins may actually be correlated with spins on non-adjacent sites. In order to make the most of equation (3.32), to find the minimum value of $\tilde{F}$ we can examine how it varies with respect to changes in the Weiss field. Breaking it down, differentiating the first line of equation (3.37) gives:

$$\begin{aligned} \frac{\partial \left(-\frac{1}{2} \sum_{ij} J_{ij} P_i P_j \hat{n}_i \cdot \hat{n}_j + \cdots - \sum_i \vec{E}_i \cdot \hat{n}_i P_i \right)}{\partial h_L} \\ = - \sum_i J_{iL} P_i \frac{\partial P_L}{\partial h_L} \hat{n}_i \cdot \hat{n}_L + \cdots - \vec{E}_L \cdot \hat{n}_L \frac{\partial P_L}{\partial h_L} \end{aligned} \tag{3.38}$$

We can differentiate the second line of equation (3.37) to get:

$$\begin{aligned}
&\frac{\partial\left(\sum_i h_i P_i \hat{n}_i \cdot \hat{n}_i - k_B T \sum_i \ln\left[\frac{4\pi \sinh(h_i\beta)}{h\beta}\right]\right)}{\partial h_L} \\
&= P_L + h_L \frac{\partial P_L}{\partial h_L} - \coth(h_L\beta) + \frac{1}{h_L\beta} \\
&= P_L + h_L \frac{\partial P_L}{\partial h_L} - P_L \\
&= h_L \frac{\partial P_L}{\partial h_L} \qquad (3.39)
\end{aligned}$$

Oriented in the direction $\hat{n}_L$.

Combining equations (3.38) and (3.39) we get:

$$\begin{aligned}
\frac{\partial \tilde{F}}{\partial h_L} = &-\sum_i J_{iL} P_i \frac{\partial P_L}{\partial h_L} \hat{n}_i \cdot \hat{n}_L + \cdots \\
&- \vec{E}_L \cdot \hat{n}_L \frac{\partial P_L}{\partial h_L} + h \frac{\partial P_L}{\partial h + L} \qquad (3.40)
\end{aligned}$$

Of course the derivative must be 0 at a minimum.

$$\begin{aligned}
\frac{\partial \tilde{F}}{\partial h_L} &= 0 \qquad (3.41) \\
&= -\sum_i J_{iL} P_i \frac{\partial P_L}{\partial h_L} \hat{n}_i \cdot \hat{n}_L + \cdots \\
&\quad - \vec{E}_L \cdot \hat{n}_L \frac{\partial P_L}{\partial h_L} + h_L \frac{\partial P_L}{\partial h_L} \qquad (3.42) \\
\Rightarrow h\hat{n}_L &= \sum_i J_{iL} P_i \hat{n}_i + \cdots + \vec{E}_L \qquad (3.43)
\end{aligned}$$

Thus, we have found, in generality, that the Weiss field which minimises the free energy is of the same form as the one assumed in equation (3.23).

And so we can confirm the value of $\tilde{F}$:

$$\begin{aligned}
\tilde{F} = &-\frac{1}{2}\sum_{ij} J_{ij} \vec{P}_i \cdot \vec{P}_j - \sum_i \vec{E}_i \cdot \vec{P}_i \\
&+ \sum_i \vec{h}_i \vec{P}_i - k_B T \ln\left(\prod_i \left(\frac{4\pi \sinh(h_i\beta)}{h_i\beta}\right)\right) \qquad (3.44)
\end{aligned}$$

And due to the inequality (3.32), we know that the true free energy is less than or equal to this value, we have found an estimate for the upper bound. Here the value of the Weiss field is that given in equation (3.43) as this will minimise the value of $\tilde{F}$ and P_i is given by equation (3.5).

Recalling equation (3.36), we can confirm that the entropy of the 2D Ising model is

$$\langle \mathcal{S} \rangle = -\frac{1}{T} \sum_i \vec{h}_i \cdot \vec{P}_i + k_B \ln \left[\prod_i \left(\frac{4\pi \sinh (h_i \beta)}{h_i \beta} \right) \right] \tag{3.45}$$

$$= -k_B \sum_i \mathcal{P}_i \ln (\mathcal{P}_i) \tag{3.46}$$

which is simply equation (3.10). Having this general relation for the free energy and entropy allows for very precise control of the system under investigation, the system can be made uniform as in the simple case above, or it can be easily made into an antiferroelectric, it can become a system with different interactions at different points in the lattice, thus allowing a more thorough investigation of various possible materials all with the same mean field treatment, simply by changing the Weiss field.

3.7 Caloric Effects

A spin lattice alone is not enough to describe the electrocaloric effect. The electrocaloric effect is the result of electric dipole (spin) interactions and the thermal agitation of the refrigerant.

As demonstrated in the section above, a general spin Hamiltonian has a spin entropy seen in equation (3.10).

However, the entropy change in the spins alone is not what leads to a caloric effect. The decrease in spin entropy leads to an increase in phonon entropy in the lattice [62] in order that the net entropy of the material does not change. One way to model such an entropy change on the lattice is with the Einstein model [57].

3.8 The Einstein Model of Solids

In the Einstein model we treat atoms on a lattice as N simple harmonic oscillators oscillating with the same frequency, which depends on the strength of the bonds within the lattice. Splitting the equation of motion into 3 components for the X, Y

and Z directions, therefore, an N atom solid is equivalent to $3N$ harmonic oscillators each vibrating at the frequency ν_E.

The energy levels of the harmonic oscillators are given by

$$E_\nu = h\nu_E \left(\nu + \frac{1}{2}\right) \tag{3.47}$$

$$\approx \Theta_E \left(\nu + \frac{1}{2}\right) \tag{3.48}$$

where the levels $\nu \in \mathbb{N}^0$ and Θ_E is the Einstein temperature of the lattice - the temperature at which the highest frequency mode (and, thus, all relevant frequency modes) is excited.

Assuming that the oscillators are in thermal equilibrium at inverse temperature β the partition function would be

$$Z = \sum_{v=0}^{\infty} e^{-\beta E_v} \tag{3.49}$$

$$= e^{-\beta h\nu_E/2} \sum_{v=0}^{\infty} e^{-\beta h\nu_E \nu} \tag{3.50}$$

$$= \frac{e^{-\beta h\nu_E/2}}{1 - e^{-\beta h\nu_E}} \tag{3.51}$$

$$= \frac{e^{-\beta \Theta_E/2}}{1 - e^{-\beta \Theta_E}} \tag{3.52}$$

This simple expression is based on the assumption that all oscillations have the same frequency. At low temperatures this leads to erroneous results as the frequencies can be highly dispersed, while at high temperatures ($T >> \Theta_E$) it well matches experimental data due to less variability in ν_E [74]. As the investigation in this thesis will be carried out on materials around or above their Einstein temperatures the low temperature problems with the model will not affect our results.

To correct the low temperature issues of the Einstein model, Debye summed over all possible frequencies instead of assuming that all phonons have the same frequency in his model of lattice vibrations [75]. Given that Debye temperatures are readily found experimentally, regularly reported in the literature and that we will be simulating systems above their Einstein and Debye temperatures, where the models provide equivalent results, we shall use the simple to calculate Einstein model with the reported Debye temperatures for a material replacing the less reported Einstein

temperature.

With the above mentioned partition function in equation (3.52) and the Debye temperature (Θ_D) we can now determine the free energy of the lattice

$$F_{Latt} = -\frac{1}{\beta}\ln(Z) \tag{3.53}$$

$$= -k_B T \ln\left(\frac{e^{-\beta\Theta_D/2}}{1-e^{-\beta\Theta_D}}\right) \tag{3.54}$$

The internal energy is given by

$$U = \frac{1}{Z}\frac{\partial Z}{\partial \beta} \tag{3.55}$$

$$= -\frac{\Theta_D}{2}\coth\left(\beta\frac{\Theta_D}{2}\right) \tag{3.56}$$

Which gives us a lattice entropy of

$$\mathcal{S} = \frac{1}{T}\left(U_{Latt} - F_{Latt}\right) \tag{3.57}$$

$$= -\frac{\Theta_D}{2T}\coth\left(\beta\frac{\Theta_D}{2}\right) + k_B \ln\left(\frac{e^{-\beta\Theta_D/2}}{1-e^{-\beta\Theta_D}}\right) \tag{3.58}$$

3.9 Isothermal Entropy Change

With all of this information it is now possible to determine ΔT first by finding the free energy

$$\tilde{F} = F_{spin} + F_{latt} \tag{3.59}$$

$$\begin{aligned} &= -\frac{1}{2}\sum_{ij} J_{ij}\vec{P}_i\cdot\vec{P}_j + \cdots - \vec{E}\cdot\sum_i \vec{P}_i \\ &\quad + \sum_i \vec{h}_i\cdot\vec{P}_i - k_B T\ln\left(\prod_L\left(\frac{4\pi\sinh(h_i\beta)}{h_i\beta}\right)\right) \\ &\quad - k_B T\ln\left(\frac{e^{-\beta\Theta_D/2}}{1-e^{-\beta\Theta_D}}\right) \end{aligned} \tag{3.60}$$

With the entropy

$$\mathcal{S} = -\frac{1}{T}\sum_i \vec{h}_i \cdot \vec{P}_i - k_B \ln\left(\prod_L \left(\frac{4\pi \sinh\left(h_L\beta\right)}{h_L\beta}\right)\right) - \frac{\Theta_D}{2T}\coth\left(\beta\frac{\Theta_D}{2}\right) + k_B \ln\left(\frac{e^{-\beta\Theta_D/2}}{1-e^{-\beta\Theta_D}}\right)$$
$$= \mathcal{S}_{spin} + \mathcal{S}_{latt} \tag{3.61}$$

This description of the free energy and entropy of the system is the same as those found in the literature [31].

By minimising the free energy we can determine the order parameter of the material for a given temperature and external field, this order parameter can then be used to determine the entropy using equation (3.61).

The isothermal entropy change (as seen in figure (2.3b)) comes about through the application of the external field causing a decrease in the dipolar entropy of the spins (due to an increase in their order parameter). However the system must not have a net decrease in entropy so higher phonon modes are activated and the entropy of the lattice increases.

This imbalance of temperature with the environment causes the excess heat to be leaked to the environment decreasing the entropy of the refrigerant but increasing the entropy of the surroundings, thus preserving total entropy. Simultaneously, the temperature and lattice entropy decrease until the temperature matches that of the surroundings.

The refrigerant is now at a lower net entropy than the entropy at which it started, the lattice entropy is the same as before the application of the field, but the dipolar entropy of the spins has decreased. The refrigerant is still at the temperature it was before the application of the external field and therefore has undergone an isothermal entropy change, removal of the field will result in an adiabatic temperature change.

3.10 Adiabatic Temperature Change

When the external field is removed the order parameter of the spin system decreases to match the appropriate value for the temperature of the system, but it can only do this through taking energy from the lattice to disorder itself. This energy lost from the lattice causes an adiabatic temperature change (as the entropy of the spins increases, so too the entropy of the lattice decreases with temperature, leading to

no net change in the refrigerant).

Mathematically, ΔT_{adi} is simply the temperature difference $T_1 - T_2$ such that

$$\mathcal{S}_E(T_1, E) - \mathcal{S}_0(T_2, 0) = 0 \tag{3.62}$$

where $\mathcal{S}_E$ is the entropy of the material under an external field and $\mathcal{S}_0$ is the entropy under zero field. This can be seen in figure (2.3) where the entropy around a phase transition is examined in both zero field and with an applied field.

This comes about due to the second law of thermodynamics. Entropy cannot be allowed to decrease so the material adjusts its temperature to convert the isothermal entropy change into an adiabatic temperature change.

Now that we have an understanding of how ΔT_{adi} occurs we wish to maximise $\Delta \mathcal{S}_{iso}$ so as to maximise ΔT_{adi}. However, section (3.4) warned of the cost of hysteresis losses on repeated cooling cycles. So we must now determine the optimal combination of temperature and applied field for maximising $\Delta \mathcal{S}_{iso}$ but minimising the hysteresis losses of a cooling cycle, as such we shall investigate the tricritical points of this system.

It is worth noting that a true ferroelectric will have larger hysteresis losses than a relaxor as it has a larger coercive field. There could be an argument then for the use of a dielectric in the cooling cycle, which will not experience any hysteresis losses, however the dielectric will also no ferroelectric phase and thus will not be capable of the necessary phase transition to induce the cooling cycle in the first place. This plus the fact that a relaxor at the ferroelectric to paraelectric transition experiences a structural phase transition, increasing the entropy (and thus temperature) change justifies the interest in relaxors over pure ferroelectrics or dielectrics.

3.11 Tuning a System to Tricritical Points

As mentioned in sections (3.3) and (3.4), the tuning between a first and second order transition has a large effect on the maximum entropy difference that can be obtained and also the energy lost to hysteresis, as such we wish to tune our caloric system to its tricritical point to optimise the cooling cycle so let us look at a toy example of how this may happen in practice.

Consider a system containing two sublattices, this would amount to a system with two different Weiss fields - one for each sublattice when solved with a mean field approximation. Each sublattice will have its own order parameter (say $\vec{P}_1, \vec{P}_2$, but system as a whole can have order parameters measured in the following way (see section (3.3))

$$\vec{P}_F = \frac{\vec{P}_1 + \vec{P}_2}{2} \tag{3.63}$$

$$\vec{P}_{AF} = \frac{\vec{P}_1 - \vec{P}_2}{2} \tag{3.64}$$

where $\vec{P}_F$ is the ferroelectric order parameter and, as usual, measures the polarisation. $\vec{P}_{AF}$ is the antiferroelectric order parameter measuring the staggered polarisation (explained in (3.3)).

The sublattices are arranged in such a way that the nearest neighbours to each spin will be spins on the alternate sublattice (c.f. section 4.6 in reference [76]), we will then take these spins to be preferentially anti-aligned to preserve the antiferroelectric order of the system. Interactions also take place between nearest neighbour spins on the same sublattice (next nearest neighbours by geometric distance). The Hamiltonian for such a system is the familiar one of

$$H = -\frac{1}{2}\sum_{i,j} J_{i,j}\vec{S}_i \cdot \vec{S}_j - \sum_i \vec{E} \cdot \vec{S}_i \tag{3.65}$$

where this time we can specify interactions internal to a sublattice (ferroelectric interactions labelled as J_I) and interactions external to a sublattice (antiferroelectric interactions labelled as J_E).

We can then write our Hamiltonian as follows

$$H = -\frac{1}{2}\sum_{i,j\in\text{N.N.}} J_E\vec{S}_i \cdot \vec{S}_j - \frac{1}{2}\sum_{i,j\in\text{N.N.N.}} J_I\vec{S}_i \cdot \vec{S}_j - \sum_i \vec{E} \cdot \vec{S}_i \tag{3.66}$$

As such, a spin would interact in a ferroelectric manner with its next-nearest neighbours (which are on the same sublattice) and in an antiferroelectric way with its nearest neighbours (which are on the opposite sublattice). Describing the Weiss field for site i we treat all nearest neighbours as having the same average spin (the average spin of sites external to the sublattice of site i) and all next nearest neighbours having the same average spin - the one internal to sublattice i. Thus the Weiss fields (c.f. equation (3.43)) for sites on either sublattice will be

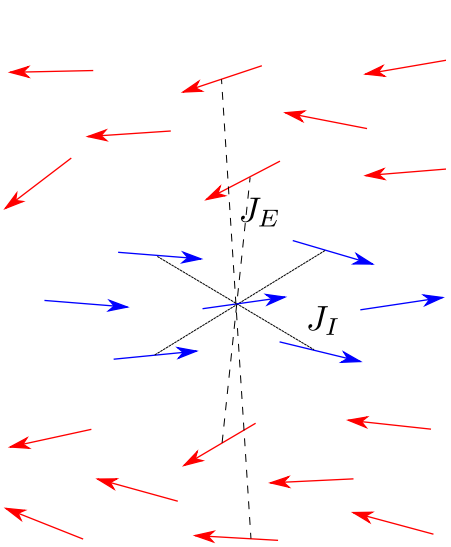

(a) Artist's impression of the system, layers of ferroelectric alignment, each oriented antiparallel to its neighbours.

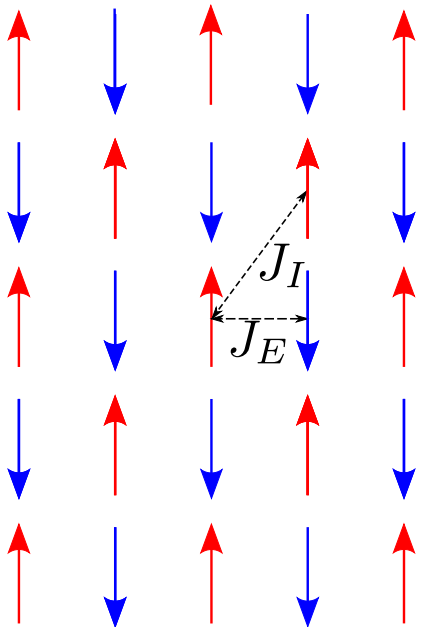

(b) How we imagine and treat the system

Figure 3.7: The configuration of this antiferroelectric set-up. On the left we see a more realistic interpretation of how the system may exist in reality, layers of alternately aligned dipoles stacked on top of each other. The image on the right shows how we treat that system in our model, we remove the locational complexity but preserve the interactions by making the 'spin' of each domain be surrounded by neighbours of the opposite alignment, we then adjust the strength of interactions with nearest and next nearest neighbours accordingly.

$$\begin{aligned} \vec{h}_1 &= J_E z_{N.N.} \vec{P}_2 + J_I z_{N.N.N.} \vec{P}_1 - \vec{E} \\ \vec{h}_2 &= J_E z_{N.N.} \vec{P}_1 + J_I z_{N.N.N.} \vec{P}_2 - \vec{E} \end{aligned} \tag{3.67}$$

$\vec{h}_1$ is the Weiss field felt by any site on sublattice 1 and $\vec{h}_2$ is the Weiss field felt by any site on sublattice 2, the order parameters for sublattice 1 and 2 are $\vec{P}_1$ and $\vec{P}_2$ respectively. $z_{N.N.}$, $z_{N.N.N.}$ are the number of nearest and next nearest neighbours respectively and $\vec{E}$ is the strength of the applied field.

The polarisation for each sublattice and the antiferroelectric and ferroelectric order parameters are shown in figure (3.8).

In order to find the tricritical point it is necessary to explore the phase diagram of the system with our two control parameters, namely the external electric

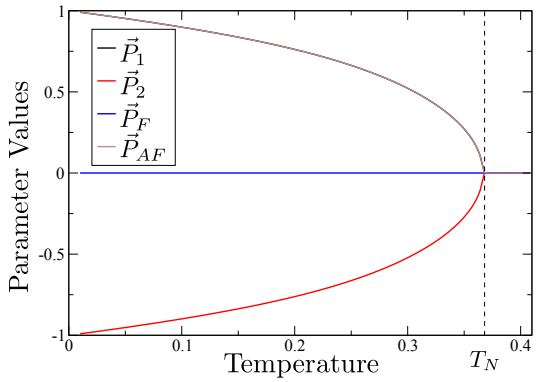

Figure 3.8: A mean field result of the antiferroelectric (brown line, non-zero below T_N, zero above) and ferroelectric (blue line, always zero in this case as there is no applied field) polarisation and the order parameters of the two sublattices in no applied field. Note that the antiferroelectric order parameter sits on top of $\vec{P}_1$ as, in zero field, $\left|\vec{P}_1\right| = \left|\vec{P}_2\right|$ and they are oppositely oriented. The results come from the use of the parameters in equation (3.68)

field and the temperature of the system.

In zero external field the system will undergo a second order antiferroelectric to paraelectric phase transition as seen in figure (3.8) at the Néel temperature, T_N.

Under a small external field this phase transition for a fixed temperature below T_N will be replaced by a second order transition going from an antiferroelectric to a ferroelectric phase shown in figure (3.9a), whereas under a strong external field it will undergo an abrupt first order antiferroelectric to ferroelectric transition as in figure (3.10). The tricritical point lies on boundary of the second and third cases.

Having trialled a wide range of parameters and observing the general trends reported for varying critical temperatures, the following interaction strengths were chosen here to illustrate the phenomenon with simplicity

$$J_{i,j} = \begin{cases} J_E = -0.1 & i,j \in \{\text{Nearest Neighbours}\} \\ J_I = 1 & i,j \in \{\text{Next Nearest Neighbours}\} \\ 0 & \text{Otherwise} \end{cases} \tag{3.68}$$

For the sake of ease the values of $z_{N.N.}$ and $z_{N.N.N.}$ were set to 1, i.e. J_E and J_I were scaled.

Figure (3.9a) shows a classic second order transition (c.f. figure (3.2b)) from antiferroelectric to paraelectric. The brown line is the antiferromagnetic order parameter, at low temperatures this is one and becomes zero at the Néel temperature while the ferroelectric order parameter is zero at all temperatures. This is in zero

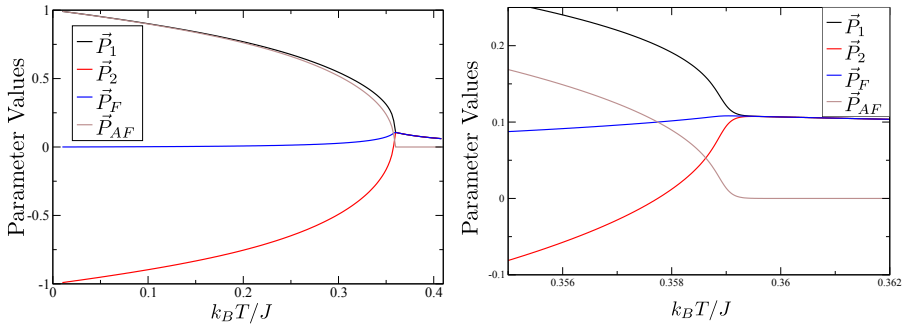

(a) Small external field (b) Large external field

Figure 3.9: A mean field result of the antiferroelectric polarisation and order parameters under a small external field. The figure on the left shows a second order transition from the antiferroelectric to ferroelectric phase. The figure on the right shows a zoomed in view around the transition temperature showing the continuity in the order parameter. The transition is slightly smoothed due to the numerical method used, however, even without this rounding there would be no discernible discontinuity.

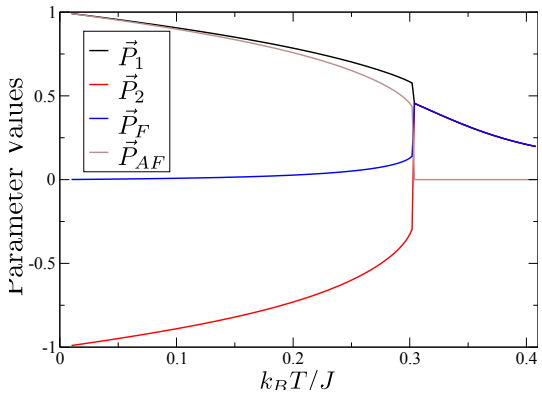

Figure 3.10: A mean field result of the antiferroelectric polarisation and order parameters under a large external fields showing a first order transition from the antiferroelectric to ferroelectric phase. Note the discontinuous change in $\vec{P}_1$ between antiferroelectric and ferroelectric phases - this shows that the ferroelectric phase has a lower free energy than the antiferroelectric phase with a lower value of $\vec{P}_1$, this will cause a large entropy change across the transition.

field.

The application of an external field raises the free energy of the antiferroelectric state and lowers the free energy of the ferroelectric state thus making it possible that there would be a transition from the antiferroelectric to ferroelectric state below the (T_N) as the field is varied.

For a field that is not too large (shown in figure (3.9a)) there is a smooth, second order phase transition from the antiferroelectric to ferroelectric state. For a larger field strength, however, we see see a discontinuous first order transition in the order parameter seen in figure (3.10) (contrast with the continuous change in figure (3.2b)).

So, the strength of the external field can change the phase transition from being a second order transition to first order, how can we tune this to the tricritical point to be at a point where the system transitions continuously but is on the cusp of experiencing a first order transition, thus minimising hysteresis losses for maximum $\Delta\mathcal{S}_{iso}$?

By holding the system at a constant temperature and varying the strength of the external field to see the effect on the order parameter, it is possible to determine where the transition will occur for a combination of temperature and field as seen in figure (3.11).

For low temperatures (the black line in figure (3.11)) there is a definite first order transition in order parameter as we increase the field strength, while at high temperatures (the purple line) the order parameter varies in a clearly smooth manner. In between (the brown and the blue lines) we see the system at a temperature just above the tricritical point and one just above where the order parameter varies in an almost continuous way. Thus the tricritical point exists at $k_BT/J \approx 0.357$ and $|\vec{E}| \approx 0.0235J$.

Having determined what the critical field and critical temperature are for the tricritical point it is possible to examine the entropy changes associated with these values as seen in figure (3.12). The results show that increasing the applied field increases the entropy changes, but does not show the energy that would be lost to hysteresis loops under the application and removal of the field.

This chapter has built upon the statistical mechanics described in chapter 2 and used them to determine the order parameter of a general system. With the order parameter we have constructed local Weiss fields to gave a general, mean field description of the behaviour of our caloric coolant. The flexibility of this description has been shown in its use for locating the tricritical point of a system at a given temperature and applied external field.

All of the pieces are now in place to be able to investigate a general caloric effect and begin a simple description of it so we shall review the literature to find the state of the art of the field and examine what is already known that can aid us in our modelling efforts.

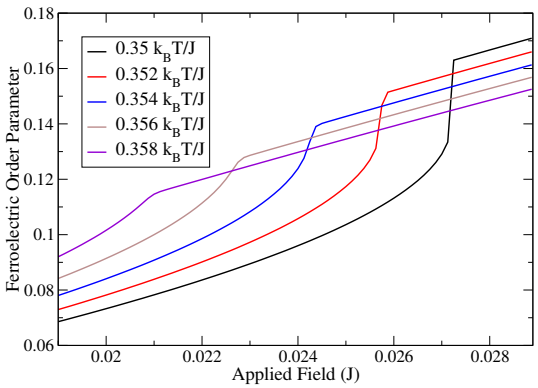

Figure 3.11: A mean field result of the ferroelectric order parameter of an antiferroelectric for different temperatures across a range of applied fields. The antiferroelectric phase exists below a critical applied field for each temperature, below this point the ferroelectric order parameter increases non-linearly with increasing applied field, above the critical field the antiferroelectric has transitioned into a ferroelectric phase and the order parameter increases linearly. The graph suggests that a tricritical point exists somewhere in the region of $(k_BT/J) = 0.356 - 0.358$ and $|\vec{E}|$=0.0234J - 0.0236J. At this combination of temperature and applied field, the order parameter is in the transition of varying continuously between the antiferroelectric and ferroelectric phases (as best demonstrated in the purple line at a higher temperature and lower field) and discontinuously (as is well shown in the black line) as a function of applied field and the transition between phases happens at this value of applied field. The tricritical point exists where the ferroelectric, antiferroelectric and paraelectric phases all coexist, this explains why the transition from one to the other would be continuous in the order parameter.

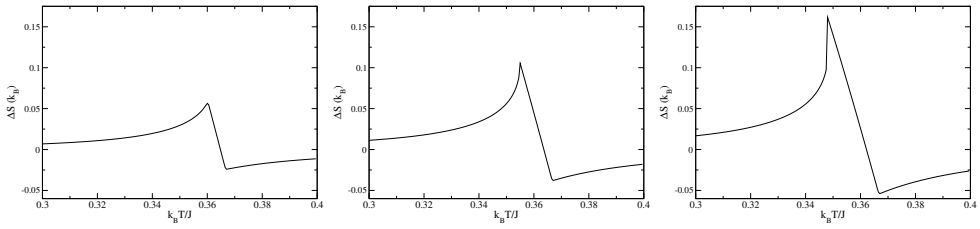

(a) $|\vec{E}| = 0.023$ (b) $|\vec{E}| = 0.0235$ (c) $|\vec{E}| = 0.024$

Figure 3.12: A comparison of the strength of the entropy change of an antiferroelectric for three different electric field strengths across a range of temperatures. The primary peak (due to the antiferroelectric-ferroelectric transition) decreases in size and shifts to higher temperatures for weaker fields. The secondary peak (at the Néel temperature) increases in size but remains at the same point. Figure (3.12a) is below the tricritical point, figure (3.12b) is on the tricritical point and figure (3.12c) is at a field strength above the tricritical point.

Chapter 4

Modelling Materials

4.1 Disorder and Hysteresis

With a good understanding of what has been found experimentally and where the field stands in terms of modelling the electrocaloric effect, we aim to produce our own simple and flexible model that is capable of predicting results of the effect. To that end we begin by trying to model the effects of disorder.

Modelling a material with random interaction strengths and random on site fields (as described in section (1.5)) was well approached by the group of Vives et al. [16]. Following this work we proceed to set up a system of Ising (i.e. non-vector) spins with the Hamiltonian:

$$H = -\frac{1}{2}\sum_{\langle i,j\rangle} J_{ij} S_i S_j - \sum_{i}^{N} E_i S_i \tag{4.1}$$

The sum is now explicitly over nearest neighbour spins and we have included the nature of the random bonds between spins and the random fields into the interaction strengths J_{ij} and the effective single site field imposed on site i, E_i. Both are modelled as having a Gaussian distribution in the weighting of their strengths as both are related to the size and location of PNRs which are expected to be Gaussian distributed [26]. The strength of the on site fields is dictated by the size of PNRs and one would expect the majority of PNRs to be of a similar size as they are formed in the same material under the same conditions. However there is a distribution of sizes as shown by the diffuse peak in the dielectric susceptibility as relaxors undergo the paraelectric to ferroelectric phase transition, a Gaussian distribution is a simple way of accounting for both of these features. Similarly the distance between PNRs accounts for the strength of the interactions and the random locations of the PNRs

distributed in the material would naturally lead to a normal distribution of distances to nearest neighbour PNRs. Our distributions are

$$W(J_\lambda) = Ae^{-\frac{(J_\lambda - \mu)^2}{2\sigma^2}}, \qquad W(E_\lambda) = Ae^{-\frac{(E_\lambda - \mu)^2}{2\sigma^2}} \tag{4.2}$$

where J_λ and E_λ are values of the interaction strength and on site field respectively, A is a normalisation factor, μ is the mean value of the distribution and σ is the standard deviation of the distribution, and hence σ^2 is the variance.

The random bonds are simulated as having a mean value of J and have a standard deviation $\sigma_{R.B.}$ while the random fields have a mean value ϵ and a standard deviation $\sigma_{R.F.}$.

A strong external field is applied in the $+Z$ direction (note that as we consider the electric dipoles to be Ising spins, so too shall we treat the external field as being aligned purely along the Z axis), such that the polarisation is saturated and all spins are aligned in the same direction, this is the ground state of the system. The strength of the field is gradually reduced to zero, waiting at each new field strength for the system to relax to the new ground state which may be a configuration where not all spins are aligned. At zero field strength the orientation of the field is reversed to point in the $-Z$ direction and the strength increased until the polarisation is saturated in this new orientation. The field is stepped back up, through 0, to its initial value in the $+Z$ direction such that a full hysteresis loop of polarisations is explored.

In a material with no random bonds or random fields there is a perfect transition from polarisation in the $+Z$ to the $-Z$ direction when all spins change direction simultaneously at a field equal to the strength of the the spin on a given site's interaction with the rest of the lattice. If the field is removed the material will continue to be aligned in the $-Z$ direction. Should a field now be applied in the $+Z$ direction, the transition from the lattice being aligned in the $-Z$ direction to the $+Z$ direction will occur at the same field strength as before (simply in the opposite orientation), as shown in figure (4.1) where $J_{i,j} = 1$ for all i, j and there are no random fields.

Turning on random bonds and random fields causes polarization avalanches to occur in our Ising spins. Polarization avalanches are analogous to the avalanches seen on mountain sides, in that one small perturbation in the system can cause a cascade of polarisation switching. This works as shown in figure (4.2). Due to the the random nature of the interactions between spins on lattice sites and the random on site fields, there is a spread of external field strengths at which an orientation

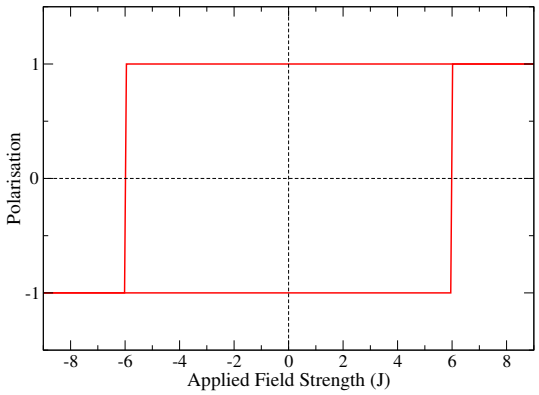

Figure 4.1: Polarisation hysteresis loop of a 3D square lattice of Ising spins with no disorder on bonds or fields, $J_{i,j} = 1$ for all i, j and there are no random fields. The system is in a 3D cubic set up so the value of coercive field for a system with no disorder is $6J$.

transition can occur. At the extreme, consider a spin which has no interactions with the rest of the lattice and has no random on site field (such as one created by the disordered chemical clusters mentioned in section (1.5)), this spin will change orientation as soon as a field is applied in the opposite direction, regardless of the strength of the field. This will, however, not lead to an avalanche.

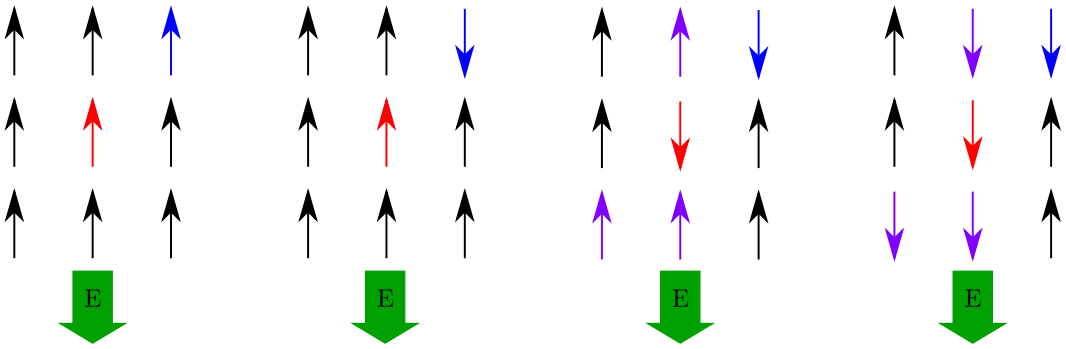

Figure 4.2: A polarisation avalanche occurring working from left to right across the groups of nine dipoles which are the same nine dipoles under different time steps. In the leftmost group of nine dipoles the dipoles are all oriented in the same direction and an external field (E) is applied. In the second group the field causes the blue dipole to switch its orientation. The effect of the blue dipole flipping causes the red dipole to flip. This causes instability in the purple dipoles, finally causing them to flip. Thus, even though the external field was only strong enough to flip one dipole initially, this caused an avalanche leading to five of the nine dipoles flipping.

To consider an avalanche, recall again equation (4.1). For a ferroelectric

interaction with the spins on sites i and j oriented in the same direction, the first term is negative. Should the applied field be oriented oppositely to the Ising spin S_i then the second term is positive and it is only energetically favourable for the spin on site i to remain oriented against the field as long as:

$$\sum_j J_{i,j} S_i S_j > -S_i E_i \tag{4.3}$$

Consider now that for a given value of E_i this condition is initially satisfied, but the spin on site k (the blue spin in figure (4.2)) now transitions, causing the magnitude of the left hand side of inequality (4.3) to reduce by $2J_{i,k}$. Should the inequality no longer be satisfied then the spin on site i (the red spin) will flip only because the spin on site k did. In such a manner a sequence of spin flips (the purple sites) can propagate through the lattice - this is an avalanche.

Figure (4.3) shows the effect of applying random bonds between spins and random on site fields (with standard deviations $\sigma_{R.B.}$ and $\sigma_{R.F.}$, respectively). The application of random fields without any random bonds causes the critical field at which a transition occurs to be reduced, but does not smooth the transition, while applying random bonds without any random fields causes a great rounding of the transition without having much effect on the critical field. The random on-site fields clearly allow for individual spins to transition but do not lead to large avalanches being created, whereas the random bonds encourage avalanche progression and lead to more rounded hysteresis curves. It also appears that random bonds are the dominant factor in changing the transition as for a large $\sigma_{R.B.}$, varying $\sigma_{R.F.}$ does very little while for large $\sigma_{R.F.}$, varying $\sigma_{R.B.}$ can have a large impact. This model only examines the interactions between PNRs or ferroelectric domains, it does not consider any interactions between dipoles within domains or any long range interactions between PNRs or domains which are not nearest neighbours.

We can also compare the simulated results of figure (4.3) to experimental results from figure (4.4). Figure (4.4) is the polarisation hysteresis cycle of Poly(vinylidene fluoride and trifluoroethylene) [P(VDF-TrFE)], a copolymer of hydrogen and fluorine - a ferroelectric polymer [77] (see section (1.5)). These can be compared to figure (4.3) to gain insight into the nature of disorder in P(VDF-TrFE) as understood by our model.

By making a comparison of the shape of the polarisation hysteresis curves as they reach an effective saturation (the maximum possible polarisation for a given input voltage) we can determine what values of $\sigma_{R.B.}$ and $\sigma_{R.F.}$ are most appropriate for describing this particular polymer. These values can then be used to perform

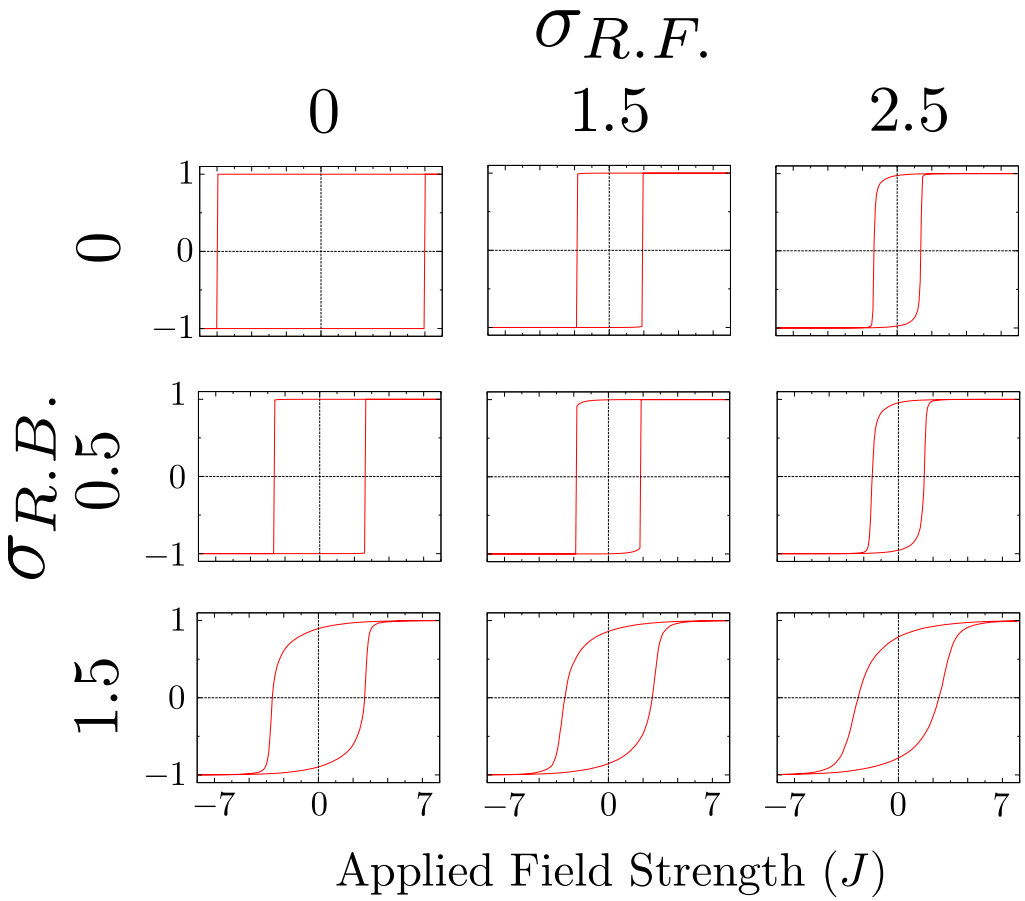

Figure 4.3: A selection of polarisation hysteresis curves for a variety of variances used in selecting the random bond and random field strengths with mean value 1 and 0 respectively. The three columns (working from left to right) show a random field variance of 0, 1.5 and 2.5 while the rows (working from top to bottom) show random bond variance of 0, 0.5 and 1.5. The x-axis of each individual graph is the strength of the applied field and the y-axis is the normalised polarisation of the total material. The system is in a 3D cubic set up so the value of coercive field for a system with no disorder is $6J$. The applied field was parametrised in units of J with a step size of $0.05J$ between field strengths.

isothermal entropy and adiabatic temperature change calculations to compare with experimental data in order to test the validity of the model and then to provide results for systems where performing such experiments may be infeasible. For example figure (4.5) shows an overlap of the experimental results with simulations where $\sigma_{R.B.} = 1$ and $\sigma_{R.F.} = 1.5$.

Note that figures (4.4) and (4.5) do not quite match. At large external field strengths, the simulated results show a saturated polarisation while the experimental

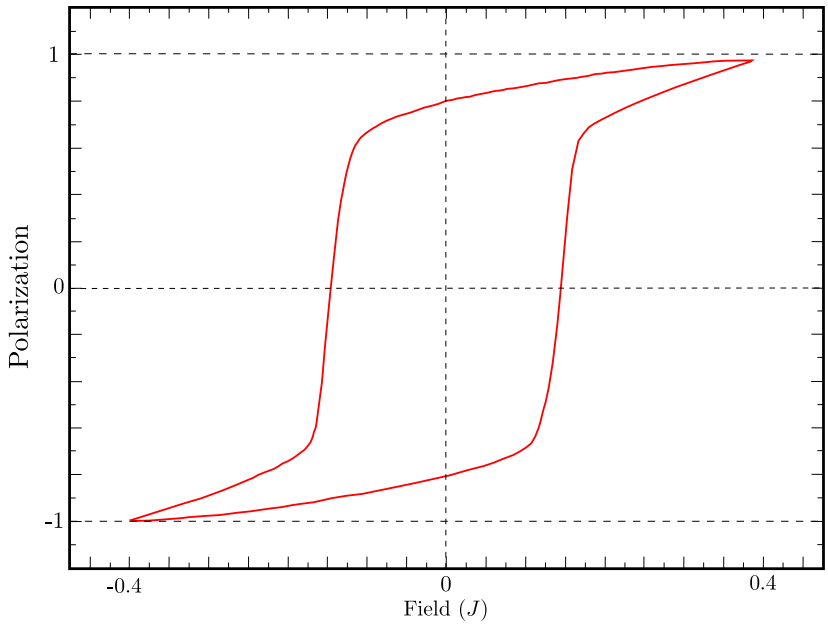

Figure 4.4: Experimentally measured polarisation hysteresis for P(VDF-TrFE) for a variety of applied field strengths, adapted from [78]. The different cycles represent different constant input voltages, while the x-axis is a varying field applied orthogonal to these.

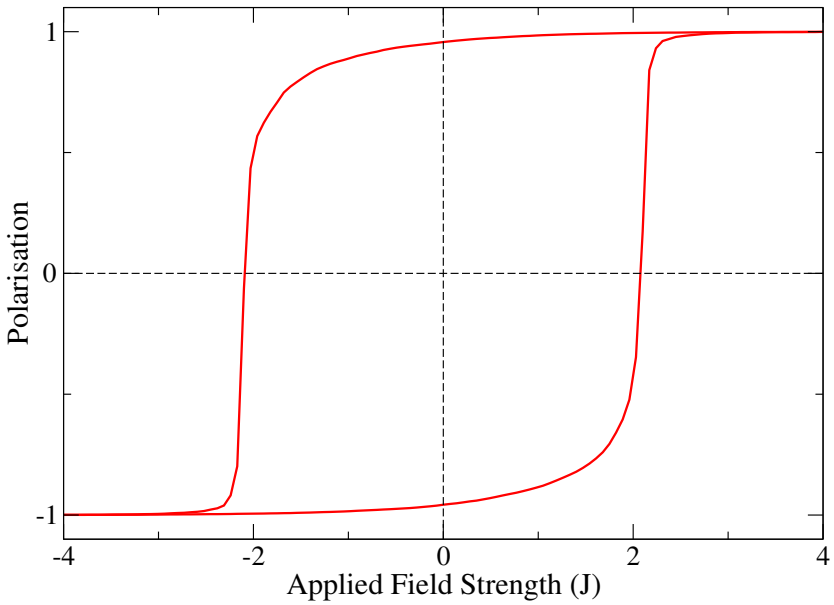

Figure 4.5: Polarisation hysteresis loop of a disordered 3D cubic lattice of Ising spins with $\sigma_{R.B.} = 1$ and $\sigma_{R.F.} = 1.5$. This is simulated to represent a hysteresis loop of P(VDF-TrFE), seen in figure (4.4).

results in figure (4.4) show a linear increase with field strength. The discrepancy between the two figures can be explained by the fact that the electric dipoles are not actually Ising spins with a value of ± 1 along an axis, they could be more realistically modelled as classical Heisenberg spins. In an isotropic model such spins would be free to orient themselves in any direction along the unit sphere, however with the anisotropic Heisenberg model the spins could be be given a preferential alignment along the Z-axis. This would mean that whilst they might, on average, be aligned in a particular orientation, individually they need not be perfectly aligned with the Z-axis, leading to a non saturated polarisation as seen in figure (4.6). As the field increases in strength they would be drawn more towards the direction of the field leading to a result like that seen in figure (4.4). Therefore it is understood why our simulations do not reproduce this feature and this is considered acceptable as the benefits of the simpler and faster to calculate Ising model outweigh this drawback and, as section (4.2) will show, we can produce quantitatively accurate adiabatic temperature changes with the Ising model.

A second discrepancy can be seen in the maximum applied field strengths in figures (4.4) and (4.5), in our simulations the maximum applied field is a larger value (by roughly a factor of 4) than that measured experimentally. This difference comes from the fact that the implementation we have used effectively models the system at 0K, this negates any contribution from thermal fluctuations which would weaken the interactions between spins. In appendix (A) we show, using a different method, that when the temperature of the system is taken into account the maximum applied field strength of our simulations is in line with experiments.

Now that there is an understanding of how disorder presents itself in materials and the effects that it has we proceed to a simple coupling of a disordered spin system to a lattice to induce an adiabatic temperature change.

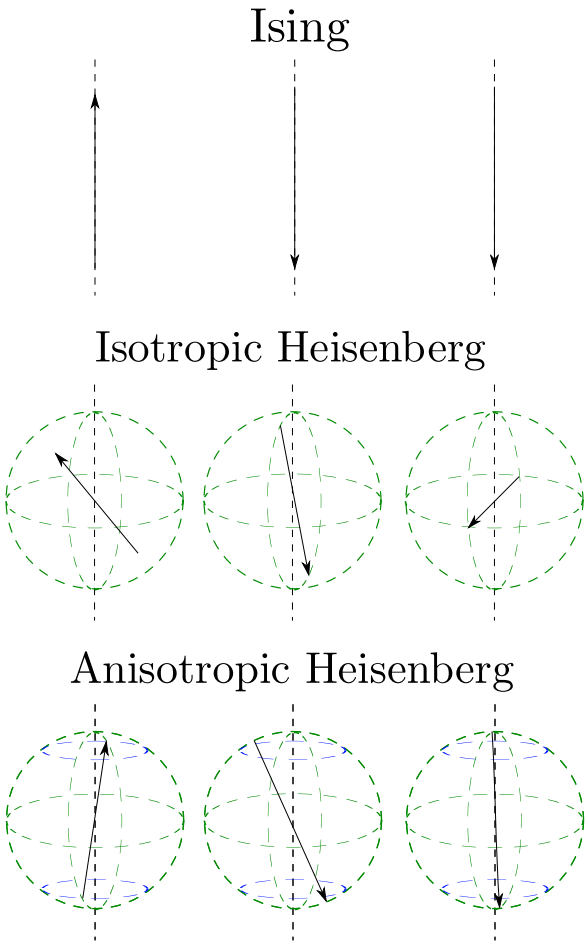

Figure 4.6: The Ising model is a model of uniaxial spins, here shown pointing along the axis. The isotropic classical Heisenberg model allows spins to point in any direction on the unit sphere, ferroelectric and antiferroelectric phases are still possible but the alignment is likely to be much weaker than that in the Ising model case. In the anisotropic classical Heisenberg model, we apply an extra condition that pressures the spins to be oriented between the poles and the blue circles of latitude shown on the diagram. This does not mean that spins will not be found outside of these regions but it is highly unlikely to find such an orientation. We can vary how anisotropic the system is between the extremes of no anisotropy and full anisotropy where we return to the Ising model. Due to the anisotropy we expect a stronger ordering than seen in the isotropic case but weaker than seen in the Ising model case, meaning that increasing the strength of the external field may increase the polarisation even when the system is already oriented in the same direction (which would mean saturation in the case of the Ising model).

4.2 Coupling Disordered Spins to a Thermal Lattice

The model proposed by Valant et al. in their 2010 paper [31] was mentioned in section (1.4), here we shall describe their methodology and how it shall form the basis of our own work.

In their model of a ferroelectric crystal, they take the dipolar spins to be Ising spins, i.e. spins which take a value of $+1$ or -1 and thus are unit vectors pointing parallel or antiparallel to one axis (as in the previous section).

This gives them a partition function of an Ising system rather than the general one found in equation (3.24).

The Hamiltonian is given as

$$H = -\frac{1}{2}\sum_{ij} J_{ij} S_i S_j - E\sum_{i}^{N} S_i \tag{4.4}$$

with the free energy $\tilde{F}$ as found in section (3.9)

$$\begin{aligned}\tilde{F} &= F_{spin} + F_{latt} \\ &= -\frac{1}{2}\sum_{ij} J_{ij} P_i P_j - E\sum_i P_i - \sum_i h_i P - k_B T \ln\left(\prod_L \left(e^{-\beta h_L} + e^{\beta h_L}\right)\right) \\ &\qquad + k_B T \ln\left(\frac{e^{-\beta\Theta_D/2}}{1 - e^{-\beta\Theta_D}}\right)\end{aligned} \tag{4.5}$$

with the entropy

$$\begin{aligned}\mathcal{S} &= -\frac{1}{T}\sum_i \vec{h}_i \cdot \vec{P}_i - k_B \ln\left(\prod_L \left(e^{-\beta h_L} + e^{\beta h_L}\right)\right) - \frac{\Theta_D}{2T}\coth\left(\beta\frac{\Theta_D}{2}\right) \\ &\qquad + k_B \ln\left(\frac{e^{-\beta\Theta_D/2}}{1 - e^{-\beta\Theta_D}}\right) \\ &= \mathcal{S}_{spin} + \mathcal{S}_{latt}\ .\end{aligned} \tag{4.6}$$

This gives the coupling of spin entropy and lattice entropy necessary for modelling a caloric effect.

Valant et al. model their Ising spins to be situated on a 2D square lattice and set $J_{i,j} = 0$ when i and j are not nearest neighbours. With four nearest neighbours per lattice site, the average interaction of J is parametrised such that $4J = T_C$.

Given the disorder in the size of polar nano regions and interactions between them, they model a Gaussian spread of interaction strengths (based on equation (4.2)) with the weighting

$$W(x) = Ae^{-\alpha\left(x-\frac{T_C}{4}\right)^2}. \tag{4.7}$$

The Gaussian variable x is used as a substitute for the interaction strength. The factor of '4' is a conversion to bring x in line with T_C by considering the number of neighbours each site will interact with. α was determined to be 0.024 by comparison to Valant's experimental data.

To use this set up in our mean field approach, we produced a selection of J_λs where the lowest weighting was only one order of magnitude less than that of the highest weighting, 500 different values were used as this provided a relatively smooth output and the calculations could be performed in a feasible simulation time. Then for each one we found the polarisation which minimised equation (4.5) both with and without an applied field. This polarisation was then used to calculate the entropy (equation (4.6)) for the cases with and without an applied field for a range of temperatures.

As described in section (3.10), the values of entropy for each temperature were then stored in a lookup table for this value of J_λ. Once all temperatures had an associated entropy the isothermal entropy change was be calculated by simply finding the difference between the entropy without an applied field and the entropy with an applied field. The adiabatic temperature change was found by taking the entropy for the system under an applied field at temperature T_1, and finding the value of entropy for the system in zero field (at temperature T_2) which analytically satisfies (or numerically minimises) the relation

$$|\mathcal{S}(T_1, E) - \mathcal{S}(T_2, 0)| \tag{4.8}$$

the adiabatic temperature change for this value of x is then $T_1 - T_2$.

Once this has been performed for all entropy values in the lookup table for this value of x the output is weighted by the relation in (4.7), we proceed to calculate the contribution for each individual x and sum the contributions of each interaction strength to calculate the total strength of the electrocaloric effect for a variety of temperatures and applied field strengths as shown in figure (4.7).

The strengths of applied field in the experiment by Valant et al. were in units of MV/m, coupling to ions in the crystal of $Pb(Zn_{1/3}Nb_{2/3})O_3$-$PbTiO_3$ with a

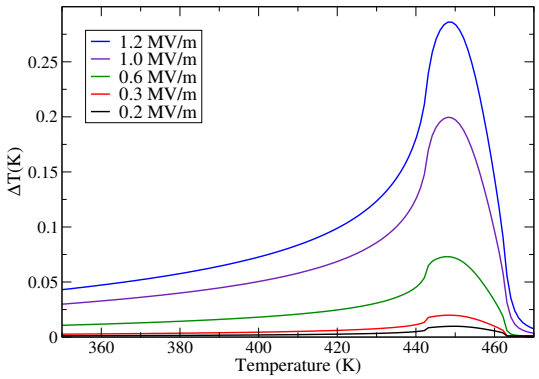

Figure 4.7: Values of the ECE at different temperatures for different applied fields attempting to simulate the adiabatic temperature change in $Pb(Zn_{1/3}Nb_{2/3})O_3$-$PbTiO_3$. The Curie temperature for this material is $\approx$ 450 K. Different lines are for different strengths of applied field, the values selected were chosen to match those from experiment (see figure (4.8)). The scales on the x and y-axes have been converted from units of J to Kelvin for ease of comparison with figure (4.8). The Debye temperature is 300K, the Curie temperature is 453K and thus the mean value of interaction strength used was 113.25 while $\sigma^2_{R.B.} = 83.3$. Reproduction of the work done in [31]

dipole moment of 0.95×10^{-30} Cm, thus the strengths from experiment were taken, multiplied by the dipole moment and divided by $113.25k_B$ ($= J$) to give the strength of applied field in units of interaction strength.

This model was developed explicitly to examine the electrocaloric effect below T_C which explains why the simulated temperature change drops off beyond the Curie temperature and there is limited or no electrocaloric effect in the paraelectric phase. Experiments [31] (see figure (4.8)) show that the peak of the electrocaloric effect is indeed at the Curie temperature but that the electrocaloric effect continues well into the paraelectric phase. Later publications [40] have suggested that while there is a peak at the depolarisation temperature (T_d, the Curie temperature in a classical ferroelectric), in a relaxor the existence of PNRs above T_d until their destruction at the Burns temperature allows for the continued existence of the electrocaloric effect.

4.3 Modelling P(VDF-TrFE)

Using the methodology of Valant et al. in section (4.2) we shall take the results of the polarisation hysteresis study in section (4.1) and estimate the electrocaloric effect that would be found in P(VDF-TrFE). We calculated that $\sigma_{R.B.} = 1$ and $\sigma_{R.F.} = 1.5$ for a 3D system where each lattice site has 6 nearest neighbours. The

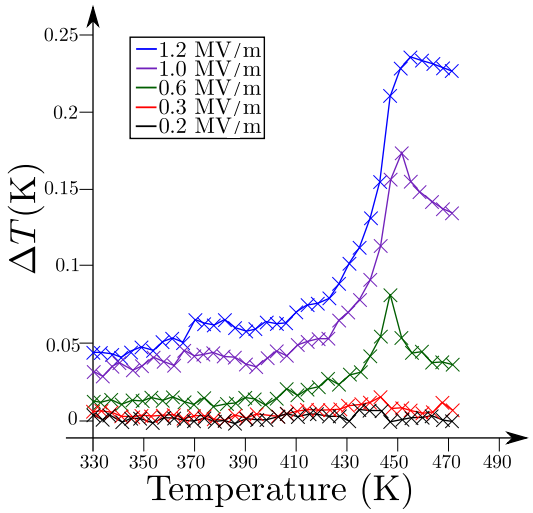

Figure 4.8: Experimental results for a crystal of $Pb(Zn_{1/3}Nb_{2/3})O_3$-$PbTiO_3$. For comparison to figure (4.7), adapted from [31].

Curie temperature for this copolymer of P(VDF-TrFE) is 391.15 K [46] giving the mean value of the random bonds as $\frac{391.15}{6} = 65.17$, the mean for the random fields remains at 0 as usual. Scaling the mean values in this way means we must also scale the variances by the same ratio leading to values of $\sigma^2_{R.B.} = 65.17$ and $\sigma^2_{R.F.} = 146.68125$. This predicts an electrocaloric effect strength seen in figure (4.9).

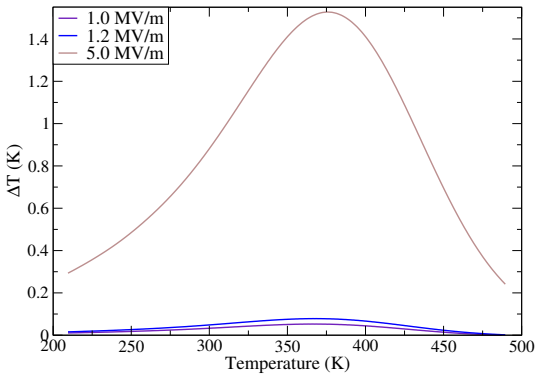

Figure 4.9: A prediction of the electrocaloric effect strength for P(VDF-TrFE) with $\mu_{R.B.} = 65.17$ and $\sigma^2_{R.B.} = 65.17$, also $\mu_{R.F.} = 0$ and $\sigma^2_{R.F.} = 146.68125$ based on results from the experimental hysteresis curve provided in section (4.1), figure (4.4). The blue and purple lines have external fields of the same strength (in MV/m) to the same coloured lines in figure (4.7).

The results in figure (4.9) suggest that P(VDF-TrFE) has a weaker effect than PZN-PT for equivalent field strengths (the purple and blue lines) and exhibits a much broader effect, the peak values for P(VDF-TrFE) are roughly one quarter

of the value of those for PZN-PT while the full width at half max for each is 150K and 40K respectively. This means that while PZN-PT is expected to have a larger electrocaloric strength, the greater electric breakdown strength of P(VDF-TrFE) allows the application of larger fields, leading to larger effects. The brown line of figure (4.9) corresponds to a field of 5 MV/m which is significantly smaller than its breakdown strength [79] thus even larger effects could be realised experimentally and this analysis suggests that even at room temperature there could (for sufficiently large field) be a strong enough effect at room temperature to justify using P(VDF-TrFE) as an electrocaloric refrigerant to replace conventional refrigerants. A temperature change of 3K would be sufficient to replace cooling devices currently in use with electrocaloric based devices with comparable costs while a 6K change could halve the cost over the lifetime of the unit [3], these are feasible targets for P(VDF-TrFE) with sufficiently large fields.

From this apparently simple ferroelectric system we wish to move on to discussing more complicated systems, such as those discussed in sections (1.5) and (1.6) where large isothermal entropy and adiabatic temperature changes are observed. The interest in these large changes for developing a strong cooling cycle is clear. However they are complicated materials to model, far more so than the simple ferroelectric crystal we have just described. We shall break the process down then by first modelling the more studied metallic magnetocaloric compounds choosing one which has an antiferromagnetic to ferromagnetic transition and using this as the basis of a model for the antiferroelectric to ferroelectric transition in relaxor polymers [24].

4.4 Modelling Iron Rhodium

As was mentioned in section (1.6), it has been shown that there is a large isothermal entropy change and adiabatic temperature change associated with the antiferroelectric to ferroelectric transition in inorganic relaxors [24]. Magnetocalorics are more comprehensively studied materials and there are some which exhibit an antiferromagnetic to ferromagnetic transition, so we shall use these as an analogy for our model for the relaxor polymers.

Iron rhodium (FeRh) is an ordered metallic alloy with a unit cell shown in figure (4.10). We impose a lattice on this system even at high temperatures where the system does not relax into an ordered state, at these temperatures we consider that there is an equal probability of finding an atom of either type on any of the lattice sites.

As the system cools down, it forms into the B2 alloyed structure where there are unit cells with one atom type on the corners and the other atom type in the centre. However, at non-zero temperatures there is a non-zero probability of finding an Fe atom having displaced an Rh atom from the Rh lattice or vice versa (at least one or two percent of the sites may experience this after typical annealing processes [53], the higher the temperature the greater this probability). Thus if the system is quenched from a high temperature it may form a state with large deviation in local stoichiometry (the ratio of the constituent elements) from a global 50-50 mix. Thus we normally observe FeRh but under deviation from stoichiometry we shall define as the convention that we observe $Fe_{1+x}Rh_{1-x}$.

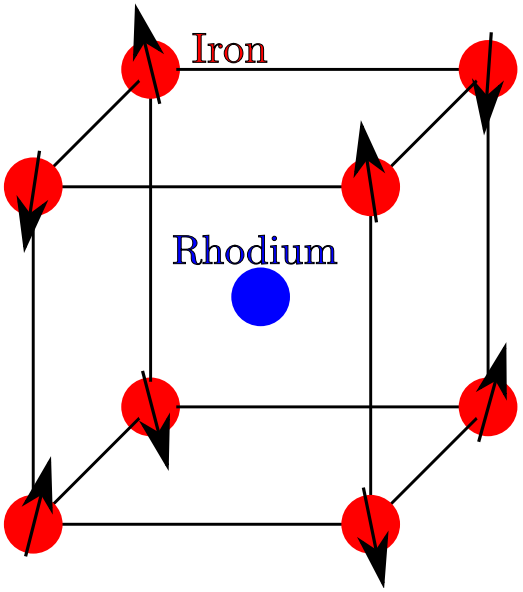

Figure 4.10: The unit cell of iron rhodium, a B2 (CsCl) alloy. The whole lattice appears as two interleaved primitive cubic lattices, one for each atom type. As such the unit cell we see here has rhodium at the centre of the unit cell and iron on the edges, the arrows show the antiferromagnetic ordering of the magnetic moments of the iron atoms, rhodium (in this system's anti-ferromagnetic phase) has no magnetic moment. In the ferromagnetic phase, the rhodium gains a magnetic moment in line with the iron moments and reinforces the ferromagnetic alignment.

Deviation from stoichiometry is an important consideration for FeRh as it is a magnetocaloric material that is very sensitive to composition, even a 2% variation in iron concentration can completely remove a ferromagnetic to antiferromagnetic phase transition that exists when the material contains equal proportions of iron and rhodium [54]. The temperature of this transition can be readily changed by

varying the way the sample is treated (e.g. via electron irradiation) [55]

Such a strong sensitivity to disorder for a material on a well ordered regular lattice indicates that it could be well treated by the methodology of section (4.2) with addition from the insights into random bonds and fields provided by the work of section (4.1).

We now use a slightly different Hamiltonian, based upon the work in [54], [80]. This models the FeRh system in the following way:

$$H = -\frac{1}{2N}\sum_{\langle i,j\rangle} J_{N.N.}\vec{S}_i \cdot \vec{S}_j - \frac{1}{2}J_{L.R.}S_{Ferro} - \frac{1}{2N}\sum_{\langle i,j\rangle} A\left(\vec{S}_i \cdot \vec{S}_j\right)^2 - \frac{1}{2N}\sum_{\langle i,j\rangle} B\left(\vec{S}_i \cdot \vec{S}_j\right) S_{Ferro} - \frac{1}{2}CS_{Ferro}^2 - \sum_i^N \vec{E}\cdot\vec{S}_i \ , \tag{4.9}$$

where the $\vec{S}_i$ are local magnetic moments on the iron sites, $J_{N.N.}$ and $J_{L.R.}$ are the interaction strength for nearest iron neighbours and long range interactions (effective interaction with the whole lattice, discussed in more detail below) respectively, $\vec{E}$ is the applied field, S_{Ferro} is the magnitude of the ferromagnetic order parameter defined by:

$$S_{Ferro} = \left|\sum_i \vec{S}_i\right| \qquad P_{Ferro} = \left|\sum_i \vec{P}_i\right| \qquad \vec{P}_i = \left\langle \vec{S}_i \right\rangle \ , \tag{4.10}$$

Equation (4.10) shows that in the antiferromagnetic phase $P_{Ferro} \approx 0$ as all vectors will be anti-aligned with their neighbours, thus their sum will lead to a zero vector and $J_{L.R.}$ will not contribute to the energy of the system. This represents the rhodium atoms being non-polarised in the antiferromagnetic state. When the system is in the ferromagnetic state, however, the lattice has expanded slightly and the rhodium atoms have moved slightly off centre such that they now contribute to the magnetic ordering and have a long range ferromagnetic order. In our simulation, $P_{Ferro} \neq 0$ and this couples to the $J_{L.R.}$ term, reinforcing the ferromagnetic ordering.

The values of A, B and C as well as the interaction strengths for nearest and long range interactions are determined by density functional theory [80] to be:

$$A = 2.68 \times 10^{-3} Ry$$
$$B = -1.2 \times 10^{-4} Ry$$
$$C = -5.94 \times 10^{-3} Ry$$
$$J_{N.N.} = -12.88 \times 10^{-3} \times (1 + 0.6x - 3.2C_2)\, Ry \tag{4.11}$$
$$J_{L.R.} = +27.70 \times 10^{-3} \times (1 + 1.56x + 2.2C_2)\, Ry \tag{4.12}$$

Where x is the average deviation from stoichiometry and should be fixed to a value in the range $-0.03 < x < 0.03$. Were the stoichiometry to deviate any further then the antiferromagnetic to ferromagnetic transition vanishes in agreement with experiment [54]. C_2 is a random variable for a chosen x to reflect the local fluctuations in the concentration of Fe, an Fe atom in place of an Rh atom would lead to new interactions from each corner site with the centre of the unit cell, while an Rh atom on an Fe site would remove ordering interactions there, it is sampled in the range

$$\begin{cases} x - 0.03 < C_2 < x + 0.03 & x > 0 \\ -0.03 < C_2 < 0.03 & x < 0 \end{cases} \tag{4.13}$$

This restricts the variation in iron concentration to be within 3%, so as to simulate the incomplete B2 ordering set up after an experimental annealing process [54].

The literature places the value of the Debye temperature for a mixture of iron and rhodium in the mid 300 K range [81], [82]. Simulations were run to determine the effect that changing the Debye temperature would have on our results and it was discovered that varying the Debye temperature by as much as 200 K (in the range from 200-400K) had no effect on $\Delta\mathcal{S}$ or ΔT, this is because changing the Debye temperature changed the entropy and the free energy of the system both with and without an applied field equally (down to machine precision) and thus any choice of Debye temperature within the 200-400 K range would yield the same result as any other. For the final simulations and the results in this thesis, the value of the Debye temperature was set at 300 k.

Our free energy is then defined by our averaged Hamiltonian (4.9) in six terms, the interaction of sites with the Weiss fields in a seventh and the final terms being the entropy of the system.

$$
\begin{aligned}
F = & -\frac{1}{2N}\sum_{\langle i,j\rangle} J_{N.N.}\vec{P}_i\cdot\vec{P}_j - \frac{1}{2}J_{L.R.}P_{Ferro} - \frac{1}{2N}\sum_{\langle i,j\rangle} A\left(\vec{P}_i\cdot\vec{P}_j\right)^2 \\
& - \frac{1}{2N}\sum_{\langle i,j\rangle} B\left(\vec{P}_i\cdot\vec{P}_j\right)P_{Ferro} - \frac{1}{2}CP_{Ferro}^2 - \sum_i \vec{E}\cdot\vec{P}_i \\
& - \sum_i \vec{h}_i\cdot\vec{P}_i - k_BT\ln\left[\prod_L\left(\frac{4\pi\sinh\left(h_L\beta\right)}{h_L\beta}\right)\right] \\
& - \frac{\Theta_D}{2}\coth\left(\beta\frac{\Theta_D}{2}\right) - k_BT\ln\left(\frac{e^{-\Theta_D\beta/2}}{1-e^{-\Theta_D\beta}}\right)
\end{aligned}
\tag{4.14}
$$

For our Weiss field we have

$$
\begin{aligned}
\vec{h}_i = & -\frac{1}{N}\sum_l J_{N.N.}\vec{P}_l - \frac{J_{L.R.}}{N}\sum_j \vec{P}_j - \frac{2}{N}\sum_l A\left(\left(\vec{P}_i\cdot\vec{P}_l\right)\vec{P}_l\right) \\
& - \frac{1}{N^3}B\left(P_{Ferro}\sum_l \vec{P}_l + \sum_l\left(\vec{P}_l\cdot\vec{P}_i\right)\sum_j\vec{P}_j\right) - \frac{2C}{N}P_{Ferro}\sum_j\vec{P}_j - \vec{E}
\end{aligned}
\tag{4.15}
$$

Therefore we also have an entropy of:

$$
\mathcal{S} = \ln\left(\prod_L\left(\frac{4\pi\sinh\left(h_L\beta\right)}{h_L\beta}\right)\right) - \frac{1}{T}\sum_i\vec{h}_i\cdot\vec{P}_i + \ln\left(\frac{e^{-\Theta_D\beta/2}}{1-e^{-\Theta_D\beta}}\right) \tag{4.16}
$$

Values of the entropy calculated with equation (4.16) need to be converted into an extensive form (one that varies as a function of the amount of material in the system) and so must consider the density of FeRh in order to be compared to experiment. The conversion factor to be used is $52.37JK^{-1}kg^{-1}$, where we divide Avogadro's number by the summed molar mass of iron and rhodium (in g per mol) and multiply by k_B to keep the dimensions correct. All entropy results presented below have been converted through this method.

The FeRh system can be forced into either a ferromagnetic or antiferromagnetic state across a wide range of temperatures as both states are either the lowest energy ground state or a metastable state. The free energy of either state can be measured using equation (4.14) and these results can be used to determine the temperature of the phase transitions as seen in figure (4.11). For the parameters $x = 0$ and $C_2 = 0$, the transition temperatures are 566 K for the transition from antifer-

romagnetism (below) to ferromagnetism (above) and the Curie temperature at 759 K (compared to 340 K and 670 K respectively from experiment [54]).

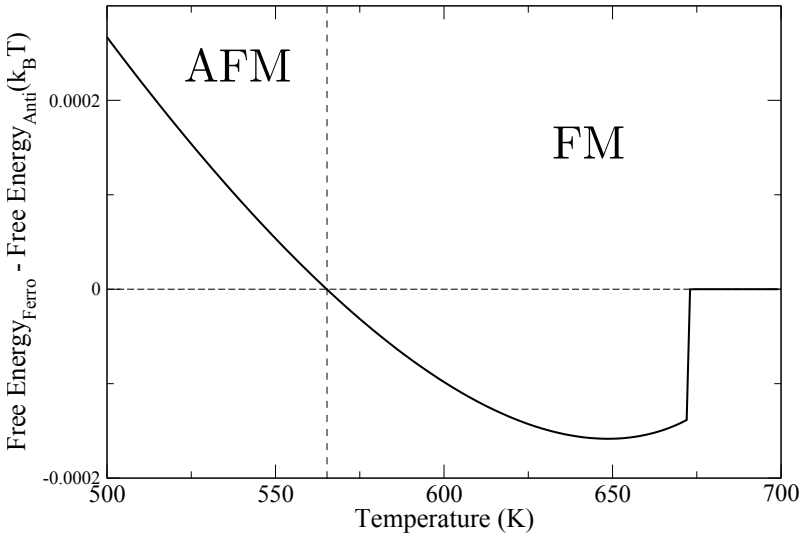

Figure 4.11: Simulation results for the difference in free energy, as a function of temperature, of the ferromagnetic and antiferromagnetic states of perfectly B2-ordered FeRh with parameters $x = C_2 = 0$. Below 566 K the system is antiferromagnetic, between 566-759 K the system is ferromagnetic and above 759 K the system is paramagnetic. This graph shows that at 674 K the free energies meet again. This is when the antiferroelectric state is no longer a metastable state and so the system collapses into a ferromagnetic ground state even if we attempt to enforce an antiferromagnetic state. The temperature of the transition is not related to the Debye temperature

We can observe in figure (4.12) how this free energy crossover manifests itself in the magnetisation and the order parameters of FeRh when averaging over 500 instances of $x = 0$ and C_2 varies with $\sigma^2 = 2.5 \times 10^{-6}$. At low temperatures the system is in the antiferromagnetic state, i.e. there is no magnetisation in the 0-field case and only a very small magnetisation in the applied field case (seen in sub-figure (4.12a)). As we cross the transition at 566 K (note that it is at a slightly lower temperature in the applied field case as the external field makes the ferromagnetic state more energetically favourable than it would be in zero field) we observe a dramatic change from a negligible magnetisation to a magnetisation on the order of half fully magnetised. Sub-figure (4.12b) at this point shows how the order parameter of the system changes as the antiferromagnetic state is more ordered than the ferromagnetic state. This change in order parameter value causes a change in the entropy. Sub figure (4.12b) then continues to show that as we reach the Curie temperature of the system at around 760 K the system in 0 field reduces

to a zero order parameter (and magnetisation) while in the applied field case it decreases to 0 at a much slower rate due to the influence of the external field. Sub figure (4.12c) shows the order parameters of the system if it were forced to maintain either a ferromagnetic or antiferromagnetic ordering for all temperatures.

The effects of disorder broadening cause the second order ferromagnetic to paramagnetic transition to become broader (as is observed if the gradual decay to zero order parameter in figure (4.12) is compared with figure (3.8)). However no effect of broadening is seen in the first order antiferromagnetic to ferromagnetic transition. We can understand this in that the antiferromagnetic to ferromagnetic transition is a whole system transition from one ordered phase to another and, for our system sizes, it appears to be energetically unfavourable for the two phases to coexist so the whole system is either purely ferromagnetic or antiferromagnetic. Whereas the ferromagnetic to paramagnetic transition is a transition from an ordered phase to a disordered phase and occurs as spins become decoupled from each other due to thermal agitation, this will happen at a diffuse range of temperatures as determined by the variation in interaction strengths and thus is disorder broadened.

Examining the isothermal entropy change of a system with $x = C_2 = 0$ under the application of a 2T external field, we see the results of figure (4.13). For reference, in units of $J_{N.N.}$ with $x = 0$ and $C_2 = 0$, a 2 Tesla field would have a strength of $2.68 J_{N.N.}$ [80].

These results show how the antiferromagnetic to ferromagnetic transition has a large entropy spike associated with it, but it is very localised to the transition, the ferromagnetic to paramagnetic transition exhibits a much weaker but broader peak. This discrepancy between the nature of the two transitions will affect how they behave under the influence of disorder.

In figure (4.14) we can see that for even a small change in C_2 value the weighted isothermal entropy change around the antiferromagnetic to ferromagnetic transition drops off rapidly, while the value around the ferromagnetic to paramagnetic transition does not vary greatly.

We take results for constant σ^2 but 800 different values of C_2 (this was the lowest round number of results which produced a sufficiently smooth output to be able to clearly observe the results, extra smoothing was required on the data but taking more results required significantly longer computer time to perform the simulations) and smoothed the output with a running average. The running average had a length of 40, this means that its first data point was the mean of the first 40 data points from the original data set, the second data point was the mean of the second to forty-first data point and so on. Each updated data point replaces

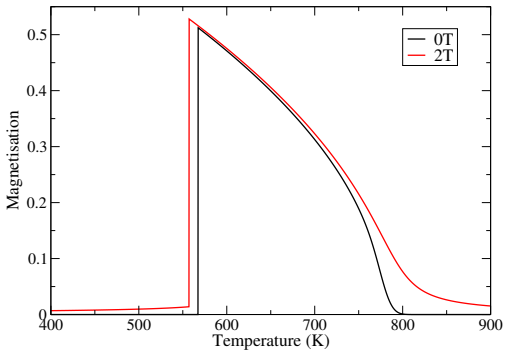

(a) The magnetisation as a function of temperature, both with and without an applied field.

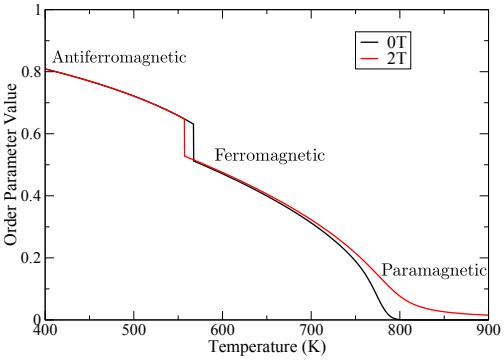

(b) The order parameter of the system as a function of temperature. Note that jump in the value of the order parameter at the antiferromagnetic to ferromagnetic transition.

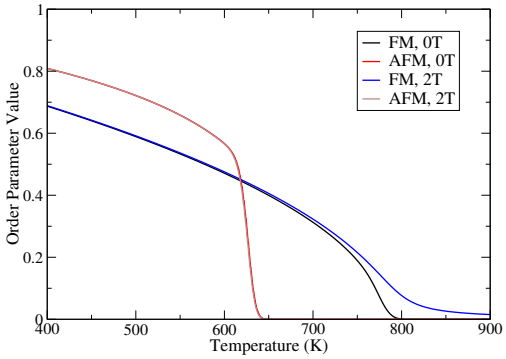

(c) The ferromagnetic and antiferromagnetic order parameters both with and without an applied field for the full temperature range.

Figure 4.12: The sharp change in the order parameter as the system goes through an antiferromagnetic to ferromagnetic phase transition is what leads to a large entropy change. Experimentally it is challenging to measure the order parameter of an antiferromagnetic (seen for our simulations in sub-figure (4.12b)) whereas it is possible to measure the polarisation directly (seen for our simulations in sub-figure (4.12a), thus we can compare our results to experiment and also observe the change in order parameter that has a direct effect on the entropy. Sub-figure (4.12c) was created by forcing the system into the antiferromagnetic or ferromagnetic state across the whole temperature regime and measuring the order parameter, it is possible to do this easily in simulation as when one state is the global minimum of free energy the other is a metastable state capable and the system can relax into that state, at least temporarily.

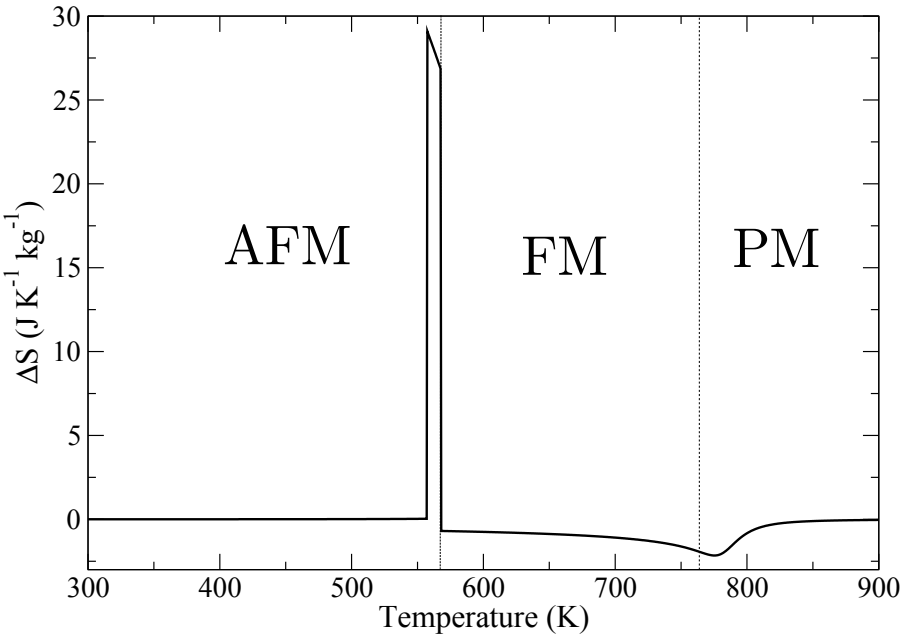

Figure 4.13: The isothermal entropy change under a 2T applied field of perfectly B2-ordered FeRh with parameters $x = C_2 = 0$.

the central point of the set that the mean was calculated from, meaning that there are 39 less data points (20 lost from the start and 19 from the end) after averaging. Performing the running average swiftly removes the sharp peaks from the original data set producing a smooth output of the isothermal entropy change and the adiabatic temperature change expected for an FeRh system under the application and removal of a 2 Tesla external field.

As described in more detail in the previous section (section (4.2)), we shall take multiple single values with the appropriate Gaussian weighting and sum them together as seen in figure (4.14). These results highlight just how quickly the isothermal entropy change ($\Delta\mathcal{S}_{iso}$) and adiabatic temperature change (ΔT_{adi}) can vary with disorder. We see that, as expected, when disorder broadened, the peak at the antiferromagnetic to ferromagnetic (AFM-FM) transition drops in amplitude and becomes a more diffuse transition while the change at the ferromagnetic to paramagnetic (FM-PM) transition does not broaden much at all and the peak height varies significantly less.

Tables (4.1), (4.2) and (4.3) show how while the percentage change of peak height is equivalent for varying C_2 values at both the AFM-FM and FM-PM transitions, the magnitude variation is much greater at the AFM-FM transition (as it has a larger magnitude for $C_2 = 0$ than the FM-PM transition does). Coupling

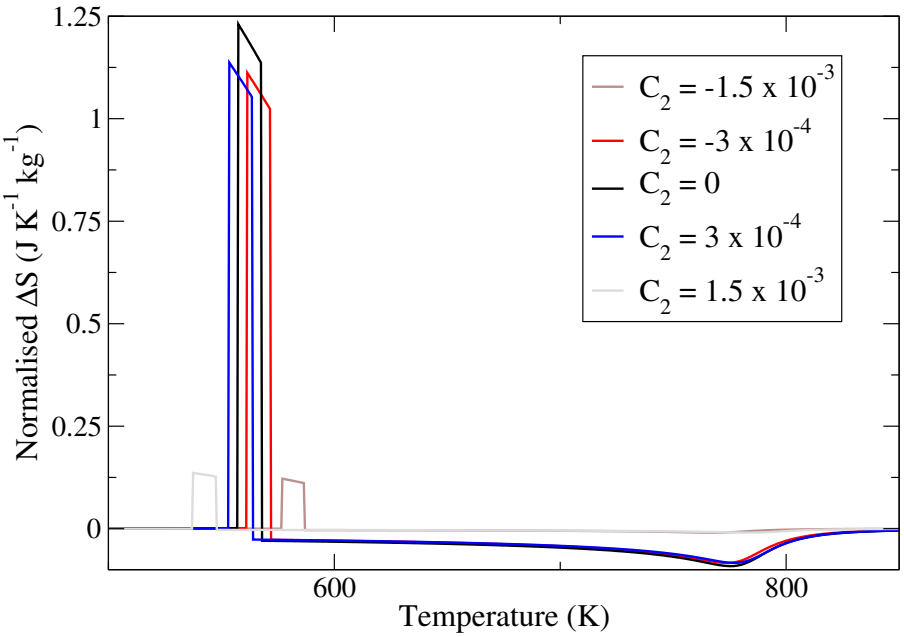

Figure 4.14: The total isothermal entropy change is the sum of the weighted change for each value of critical temperature. For this figure the ΔS results for different values of C_2 were weighted by a Gaussian with mean $C_2 = 0$ and a variance of $\sigma^2 = 5 \times 10^{-7}$, $x = 0$. The applied field strength is 2T. Select values were taken here to emphasise the effect that the weighting has on the value of the entropy change with even a small variation in C_2 value which is why $C_2 = \pm 1.5 \times 10^{-3}$ has a peak value almost ten times smaller than the peak at $C_2 = 0$.

C_2 value	-1.5×10^{-3}	-3×10^{-4}	3×10^{-4}	1.5×10^{-3}
AFM-FM	-1.09	-0.0936	-0.119	-1.11
FM-PM	0.0817	0.00794	0.00776	0.0816

Table 4.1: Values of peak height for $C_2 \neq 0$ with the peak height of $C_2 = 0$ subtracted at both the AFM-FM and FM-PM transitions to 3 significant figures. This shows a much larger magnitude change for the normalised peak height at the AFM-FM transition that at the FM-PM transition.

C_2 value	-1.5×10^{-3}	-3×10^{-4}	3×10^{-4}	1.5×10^{-3}
AFM-FM	-88.9	-7.61	-9.66	-90.1
FM-PM	-89.5	-8.71	-8.50	-89.4

Table 4.2: Percentage change peak height for $C_2 \neq 0$ compare to the peak height of $C_2 = 0$ at both the AFM-FM and FM-PM transitions to 3 significant figures. This shows that the percentage change at each transition is approximately the same for the same C_2 value.

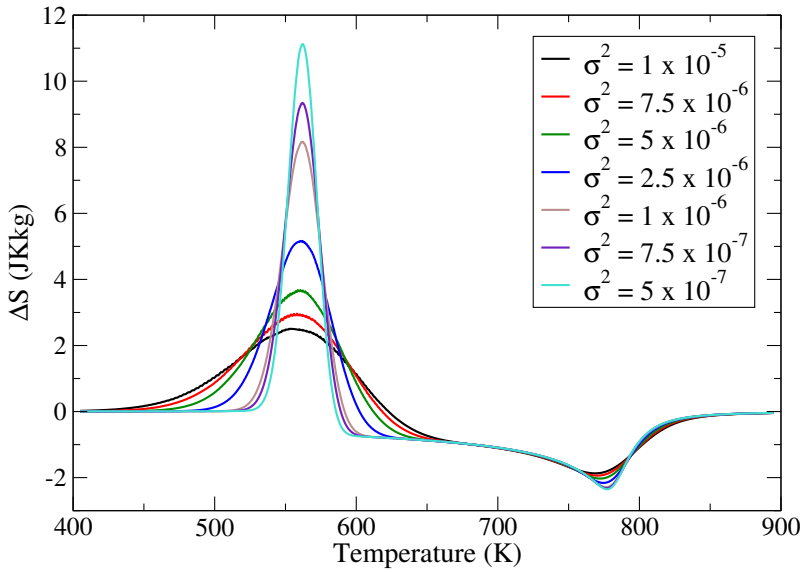

Figure 4.15: The isothermal entropy change, under a 2T field, of a disorder broadened FeRh system for varying widths of Gaussian spread of interaction strengths.

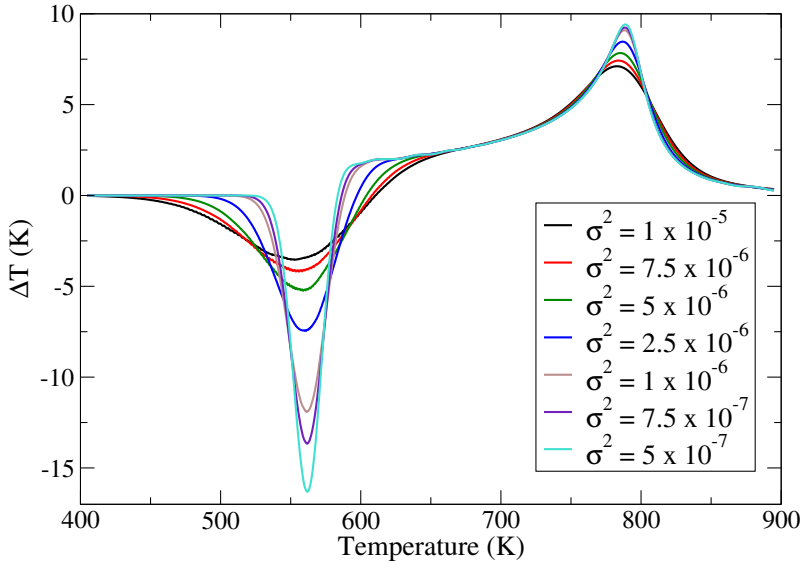

Figure 4.16: The adiabatic temperature change, under a 2T field, of a disorder broadened FeRh system for varying widths of Gaussian spread of interaction strengths.

this to the fact that there is greater variation in the temperature at which the peak value occurs at the AFM-FM transition we see that variations in disorder will have a greater effect on the width and strength of the AFM-FM peak than they will to

C_2 value	-1.5×10^{-3}	-3×10^{-4}	3×10^{-4}	1.5×10^{-3}
AFM-FM	-20	-4.5	4	19.5
FM-PM	8	1.5	-2	-8.5

Table 4.3: Temperature difference between the locations of the peak height for $\Delta\mathcal{S}_{iso}$ for $C_2 \neq 0$ when compared to $C_2 = 0$ at both the AFM-FM and FM-PM transitions. This clearly shows that the AFM-FM transition varies much more strongly than the FM-PM transition.

the FM-PM peak.

So far we have looked at the variation of $J_{N.N.}$ and $J_{L.R.}$ and have a good handle on how disorder (i.e. variation in the C_2 parameter) can affect $\Delta\mathcal{S}_{iso}$ and ΔT_{adi} there, but what happens when we vary the x parameter while keeping the variance of the Gaussian distribution of C_2 constant? These results are seen in figures (4.17) and (4.18).

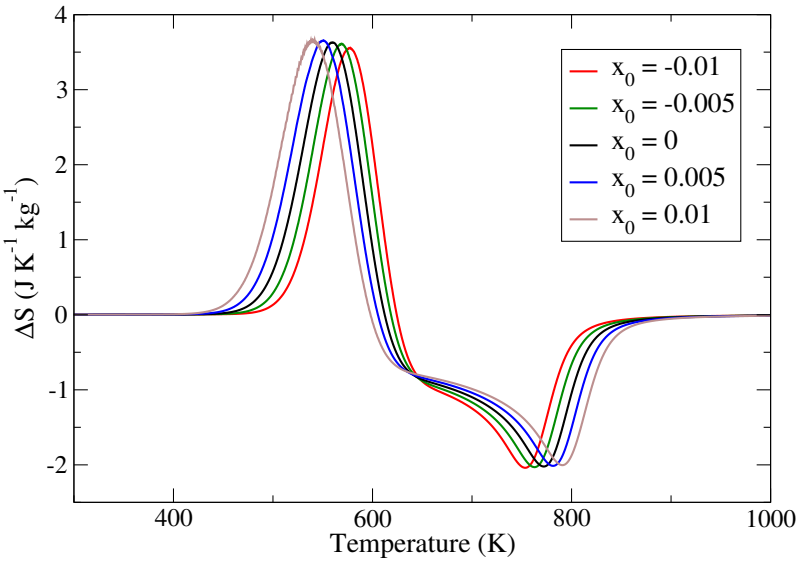

Figure 4.17: The isothermal entropy change, under a 2T field, of a disorder broadened FeRh system for varying widths of Gaussian spread of interaction strengths. The values of x are varying but σ^2 is kept constant at 5×10^{-6}.

x controls the transition temperatures of the system, we can see that even modest values have a noticeable effect on the location of the transition temperatures. The more negative x is, the more it weakens the ferromagnetic state (as evidenced by the increase in temperature of the antiferromagnetic to ferromagnetic transition and the decrease in temperature of the ferromagnetic to paramagnetic transition) and decreases $\Delta\mathcal{S}_{iso}$ and ΔT_{adi}. The more positive x is the more it enhances the

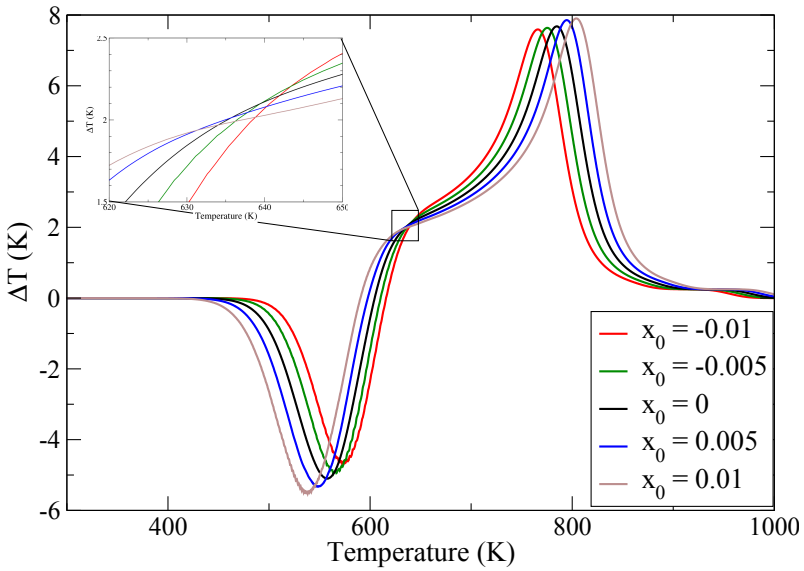

Figure 4.18: The adiabatic temperature change, under a 2T field, of a disorder broadened FeRh system for varying widths of Gaussian spread of interaction strengths. The values of x are varying but σ^2 is kept constant at 5×10^{-6}.

ferromagnetic state (notice how the transition temperatures move apart, lowering the temperature of the antiferromagnetic to ferromagnetic transition) and increases $\Delta\mathcal{S}_{iso}$ and ΔT_{adi}, such variation is seen experimentally [83], [84].

A consequence of this is that the more positive x is, the larger the isothermal entropy and adiabatic temperature changes become for the antiferromagnetic to ferromagnetic transition. This is due to the larger change in order parameter across the transition at lower temperatures. Around the ferromagnetic to paramagnetic transition there is a lesser change in entropy and temperature as shown in table (4.4)

	$\Delta\mathcal{S}_{iso}(JK^{-1}kg^{-1}$				$\Delta T_{adi}(K)$			
x values	-0.01	-0.005	0.005	0.01	-0.01	-0.005	0.005	0.01
AF/F	0.04	0.025	-0.02	-0.07	-0.4	-0.2	0.15	0.44
F/P	-0.019	-0.009	0.008	0.017	-0.1	-0.05	0.05	0.1

Table 4.4: The shift of $\Delta\mathcal{S}_{iso}$ and ΔT_{adi} in figures (4.17) and (4.18) at a deviation from $x = 0$ for both the antiferromagnetic to ferromagnetic (AF/F) transition and the ferromagnetic to paramagnetic (F/P) transitions.

Comparing our results to experimental results (see figures (4.21), (4.22) compiled from references [61], [85]), we cannot reproduce the experimental results quantitatively, but we get good qualitative agreement - as the strength of the external

	Fig (4.17)				Fig (4.18)			
x values	-0.01	-0.005	0.005	0.01	-0.01	-0.005	0.005	0.01
AF/F	-20	-10	9	17	-20	-9	8	16
F/P	-18.5	-9.5	9.5	18.5	-19	-9	10	19

Table 4.5: The shift of location of the peak in figures (4.17) and (4.18) at a deviation from $x = 0$ for both the antiferromagnetic to ferromagnetic (AF/F) transition and the ferromagnetic to paramagnetic (F/P) transitions.

field increases as well as the peak of the adiabatic temperature change and the full width at half maximum of both the isothermal entropy change and adiabatic temperature change increase with increase applied field. We also observe a saturation of the isothermal entropy change and adiabatic temperature change as the strength of the external field increases.

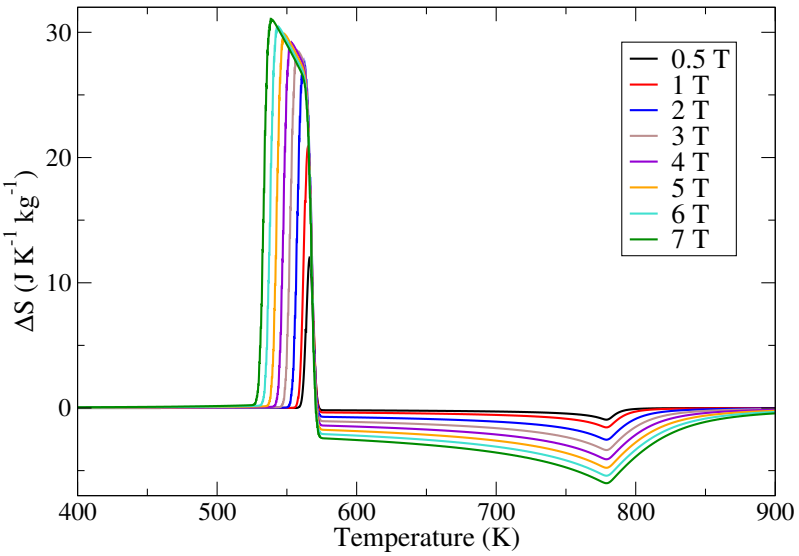

Figure 4.19: The isothermal entropy change of a disorder broadened FeRh system for varying strengths of applied field. $x = 0$, $\sigma^2 = 3 \times 10^{-8}$. For comparison with figure (4.21) [61]

We have calculated the full width at half maximum (FWHM) from selected representative experimental results [61], [85]. These results are for comparison to the FWHM for our simulations, the results are shown in figure (4.25). The results show that the FWHM in real materials is more sensitive to the strength of the external field than our simulations are. Both experimental papers show roughly the same trend of roughly $FWHM \approx 9E$ where E is the applied field strength in Tesla.

We varied the strength of σ^2 in an attempt to match the FWHM of simu-

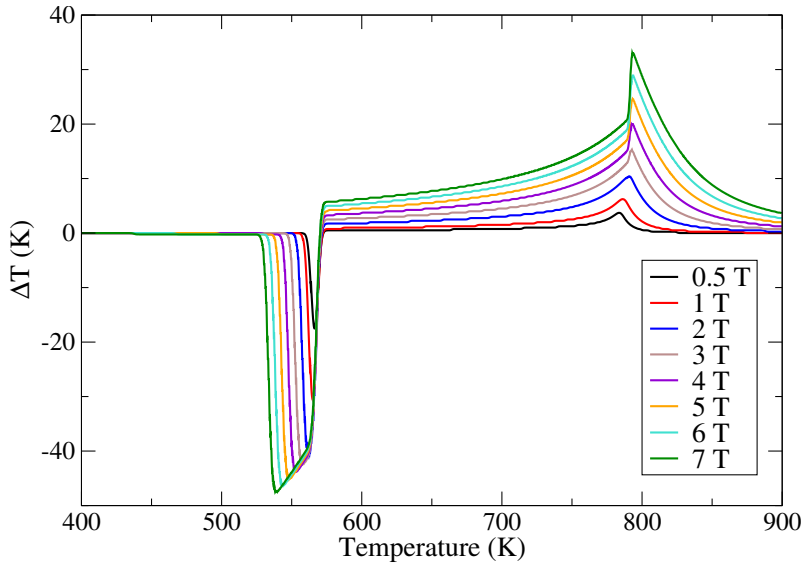

Figure 4.20: The adiabatic temperature change of a disorder broadened FeRh system for varying strengths of applied field. $x = 0$, $\sigma^2 = 3 \times 10^{-8}$. For comparison with figure (4.22) [85].

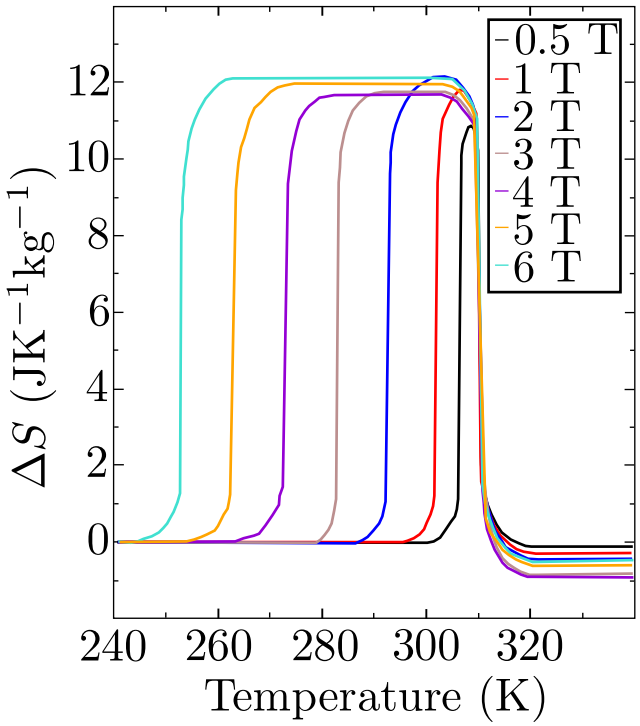

Figure 4.21: Experimental results of the isothermal entropy change of FeRh at the antiferromagnetic to ferromagnetic transition, adapted from [61]

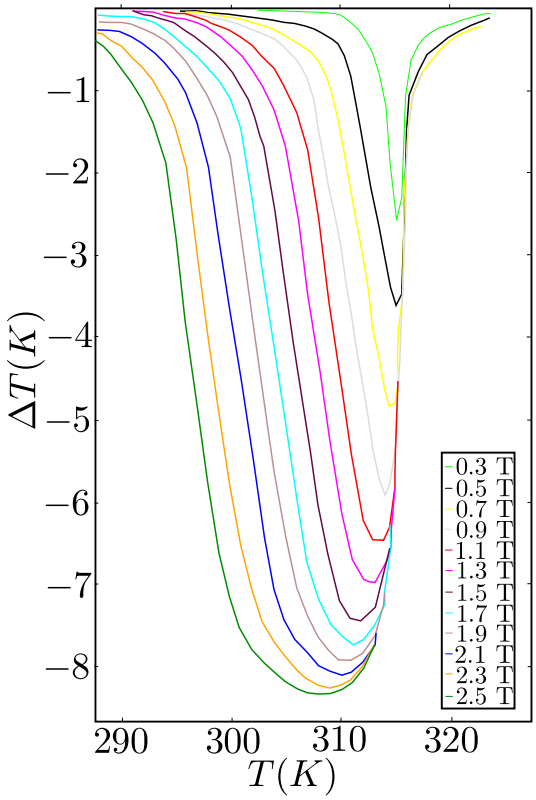

Figure 4.22: Experimental results of the adiabatic temperature change of FeRh at the antiferromagnetic to ferromagnetic transition, adapted from [85].

lations to the experimental data. Our results show that for large values of σ^2 (say $\sigma^2 \geq 5\times10^{-7}$) there is a very weak effect found by varying the field, while for smaller values an asymptotic limit is reached of $FWHM \approx 5E$ where E is the applied field strength in Tesla. The largest value of σ^2 that lies completely on this asymptote is 1×10^{-9} so the disorder in a simulation will need to be at most this value in order to represent the linear nature of the growth of the FWHM, thus at least qualitatively representing experiment even if not quantitatively doing so. The reason that less disordered systems would experience a greater response to the application of an external field is due to a stronger attraction between spins. Highly disordered systems would have a wide range of interaction strengths meaning that there will be some regions where spins are more strongly aligned than in a pure system and some regions where they are less strongly aligned. In a pure system, spins will react not just to the applied field, but also to the reaction of their neighbours, this amplifies the effect of the field. In a disordered system, however, regions of weak alignment will not have this secondary amplification and so will show less sensitivity to the

external field.

The other figure of merit to compare the simulations to experiment is the peak value attained for a given applied field strength. Figures (4.26) and (4.27) are intended to show how the peak values of the isothermal entropy change and adiabatic temperature change vary as a function of applied field, both in experiment and in our simulations.

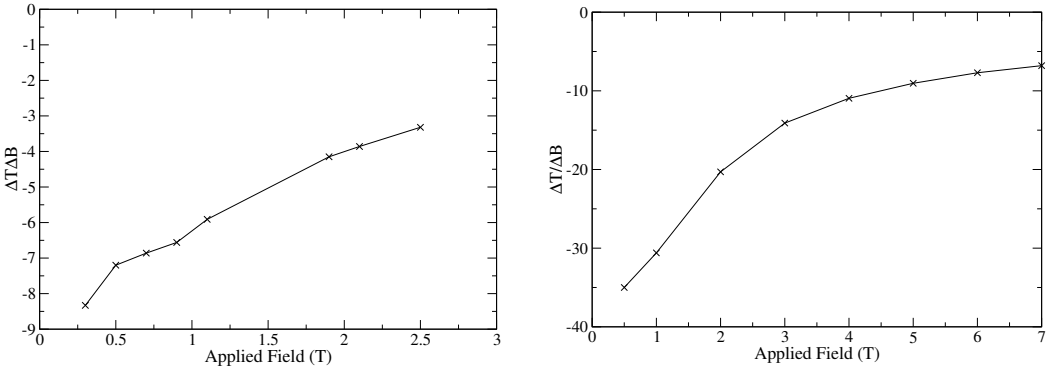

(a) Experimental results of $\Delta B/\Delta T$ [85] (b) Theoretical results of $\Delta B/\Delta T$

Figure 4.23: In units of K/T these figures show measurements of the magnetocaloric strength (i.e. $\Delta T_{adi}/\Delta B$) for both the antiferromagnetic-ferromagnetic (AF/F) transition and the ferromagnetic-paramagnetic transition (F/P). The left hand graph shows experimental results from [85] while the right hand graph shows results from our simulation . Comparing results from our simulations to experiment we see that while the magnetocaloric strength is a factor of five larger in our results, the percentage change in strength per Tesla is roughly equivalent in the same ranges, around 25% for the 0.5-1 Tesla range and around 35% in the 1-2 Tesla range.

Our calculations of the magnetocaloric strength shown in figure (4.23) are larger than those seen experimentally (c.f. [61], [85]) but then the entropy change is larger than seen experimentally too [86], [87], [82]. The qualitative results are promising in that the values begin to plateau at larger fields and that the results are stronger at the antiferromagnetic to ferromagnetic transition than at the ferromagnetic to paramagnetic transition.

The refrigerant capacity (see figure (4.24)) is also anomalously high when compared quantitatively to the literature, however the general trend is again satisfactory.

Stern Taulats et al. [61] supply only isothermal entropy change data and the peak value as a function of applied field is broadly flat, with no obvious influence of the effect of the field (see figure (4.21)). The closest results found in simulation

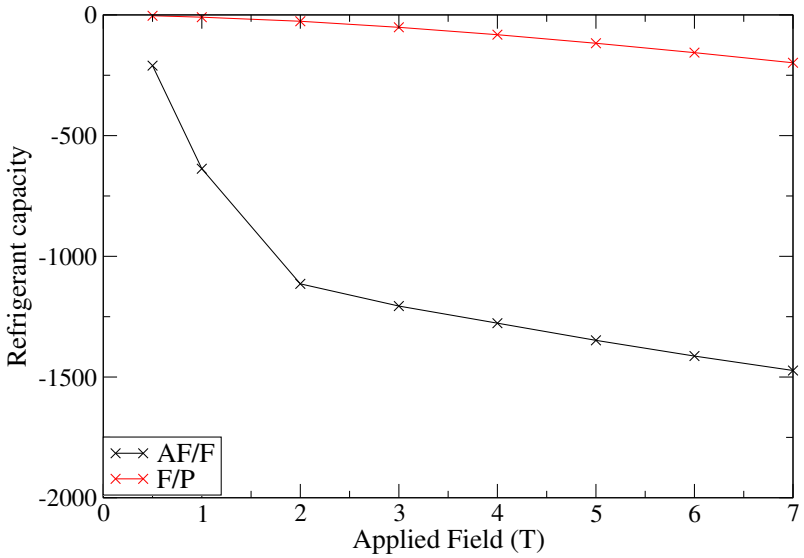

Figure 4.24: The refrigerant capacity ($\Delta T_{adi} \cdot \Delta \mathcal{S}_{iso}$) of our simulated system for a variety of applied field strengths.

are for values of σ^2 that are 1×10^{-9} or less, at which point the peak isothermal entropy change value has reached an asymptote and increases only slowly. This gives a rough qualitative agreement but value of the peak height is overestimated by a factor of 3.

Comparisons with the peak value of adiabatic temperature change can be made with the results from Annaorazov et al. [85], who report a slight curve to an asymptotic limit at low field strengths. This differs from all other results thus far in suggesting a slightly more disordered system ($\sigma^2 \gtrsim 1 \times 10^{-9}$). The variation is very slight and happens over a longer range than is entirely reproducible in our simulations. Once again the peak values have too large a magnitude in simulation when compared to experiment but the qualitative long term trend is well matched.

In summary of the above results, our simple spin model with disordered interaction strengths and random on site fields provides a reasonable qualitative picture of how disorder broadening affects the isothermal entropy change and adiabatic temperature change in FeRh under a variety of applied field strengths. The model used to examine the magnetocaloric FeRh was applied to the electrocaloric polymer P(VDF-TrFe) to predict the strength of its adiabatic temperature change under the application and removal of an external electric field. The effects of disorder on the interaction strength also correspond well with the disordered nature of interactions in the oxide perovskite PZN-PT as reported in the literature and modelled earlier. We have demonstrated that we have a model which is well suited

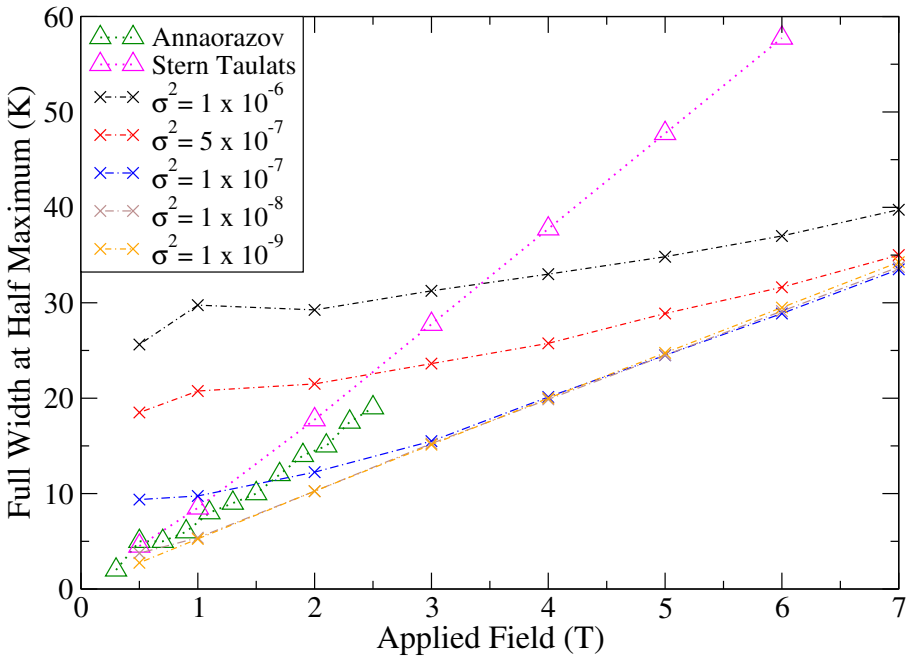

Figure 4.25: The average of the full width at half max of ΔT and $\Delta \mathcal{S}_{iso}$ for experimental results (the pink and green triangular plots) and simulated values of different σ^2 values (all other plots). The theoretical results are the average FWHMs of figures (4.19) and (4.20) while the experimental results are from figures (4.21) and (4.22). The lines are a guide to the eye to follow the trend.

to examining the broad effects of disorder and with a set up that is versatile enough to change Hamiltonian or values of interaction strengths to model other systems should appropriate parameters be given or determined through the interrogation of hysteresis curves.

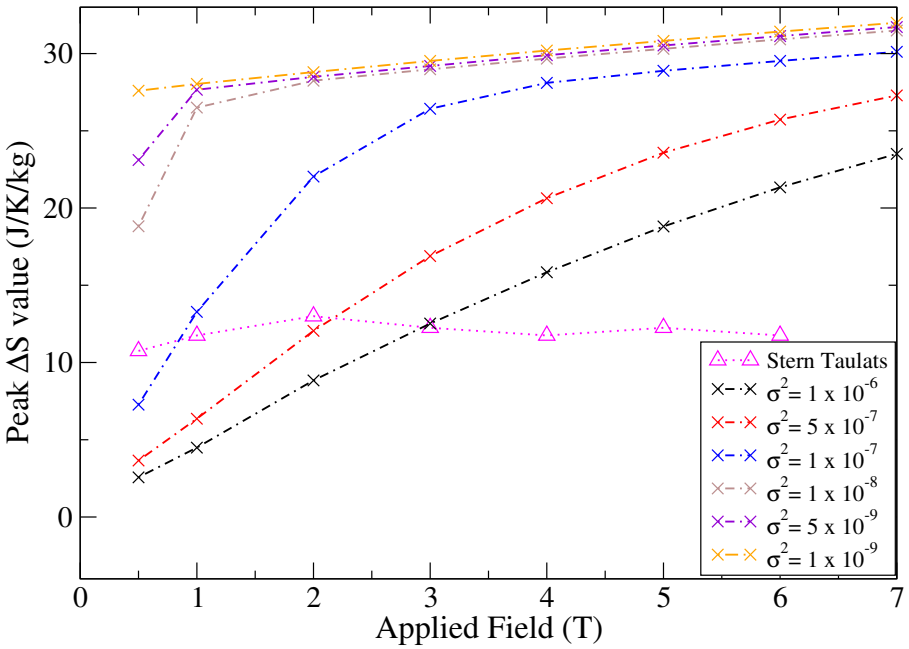

Figure 4.26: The peak value of $\Delta\mathcal{S}_{iso}$ in FeRh for a variety of disorder values and applied field strengths. The Stern Taulats results are from reference [61]

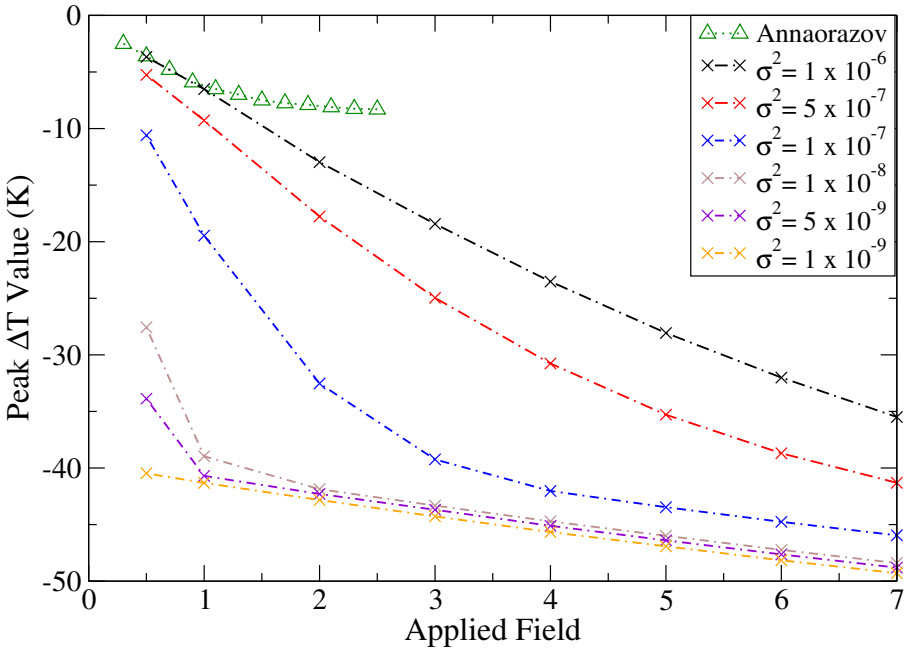

Figure 4.27: The peak value of the ΔT in FeRh for a variety of disorder values and applied field strengths. The green Annaorazov results are from reference [85].

Chapter 5

Binary Tree Graphs

5.1 Background Methodology

As an aside to the main project, some time was also spent collaborating with Goldsborough et al. on work that is being written into a paper by Goldsborough [88]. This chapter deals with the part of the work in which I was most influential and neglects the sections in [88] where I had a minor contribution. This chapter has no relevance to the theoretical modelling of a solid state cooling cycle.

This work looked at ordered Catalan tree graphs, similar tree graphs are widely used in computer science and as an analogue for connections in the Hilbert space of disordered (quantum) Heisenberg chains, for example modelling correlations between magnetic atoms in a quantum wire.

Ordered Catalan tree graphs are full binary trees (as shown in figure (5.1)), i.e. every internal vertex has exactly two children (hence binary), an external vertex (or leaf) is one with no children. An n vertex tree has n internal vertices or nodes, the root vertex is the one at the top of the tree and the only vertex that has no parent vertex, a sub tree with root v is the set of nodes (including v) and leaves which branch from v.

Figure (5.2) demonstrates that there are a finite number of unique trees for a given n, using diagrammatic notation we can define the total number of unique Catalan trees for a given n, it is the number of trees in the left hand sub tree multiplied by the number of trees in the right hand sub tree, defining these numbers as C_α and $C_{n-\alpha-1}$ and using induction we see the relation:

$$C_n = \sum_{\alpha=0}^{n-1} C_\alpha C_{n-\alpha-1} \tag{5.1}$$

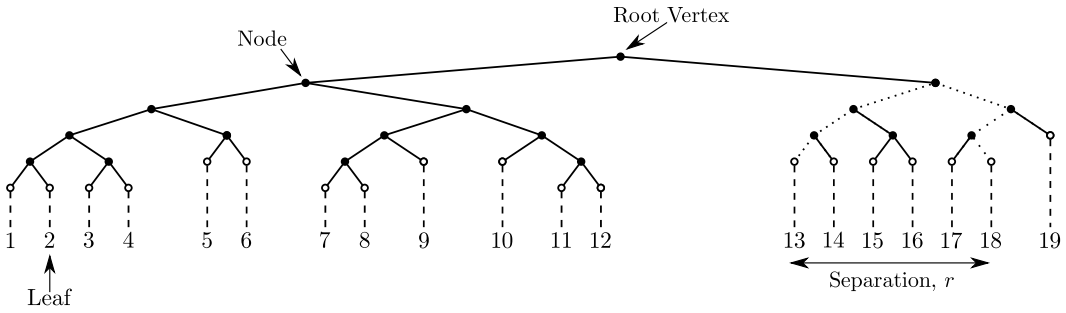

Figure 5.1: A tree diagram showing the Root Node where the tree starts; each vertex having two children (making it a binary tree). Leaves being the final vertex in a chain; the separation, r, between two leaves (in this case 13 and 18) joined by the dotted path. This is a random tree as not every leaf is on the same level

Which is known as Segner's relation [89] for Catalan numbers:

$$C_n \frac{1}{n+1} \begin{pmatrix} 2n \\ n \end{pmatrix} \frac{(2n)!}{(n+1)!n!} = \frac{4n-2}{n+1C_{n-1}} \tag{5.2}$$

As well as being able to define the number of trees with n nodes, we also note that the number of leaves for a tree with n nodes is $L = n+1$, as demonstrated (for small n) in figure (5.2) where we see that trees with $n = 1, 2, 3$ have $L = 2, 3, 4$

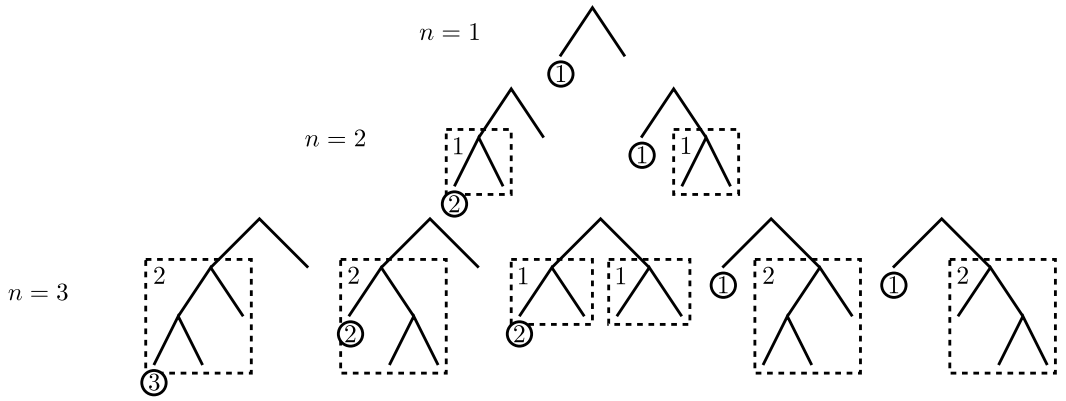

Figure 5.2: Counting the depth of the first leaf for each family of n vertex graphs ($n = 1, 2, 3$)

We shall use generating functions [89], [90] to form and solve equations involving the Catalan numbers as, in general, they can be used for manipulating and determining the properties of an unknown series. Given a general infinite series with terms a_0, a_1, $\cdots$, a_n, $\cdots$, it is possible to define a function:

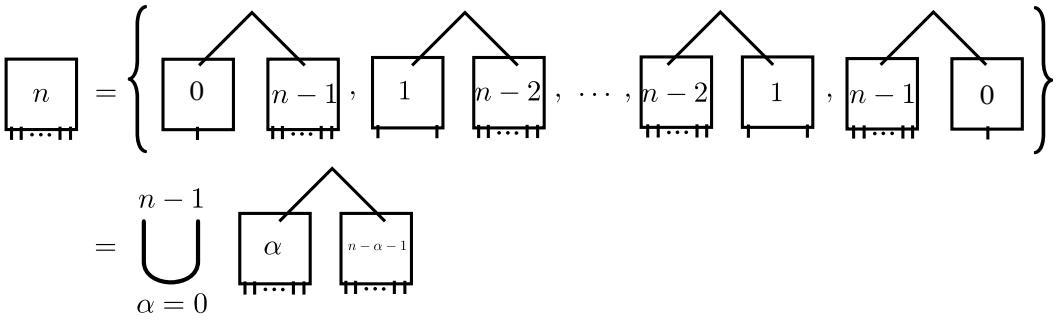

Figure 5.3: The decomposition of the set of trees with n nodes in terms of sub trees from the root.

$$a(x) = a_0 + a_1 x + a_2 x^2 + \cdots a_n x^n + \cdots \tag{5.3}$$

$$= \sum_{n=0}^{\infty} a_n x^n \tag{5.4}$$

which is called the generating function of the sequence a_n. The inverse relation of this gives that a_n is the coefficient of x^n in the Taylor series representation of $a(x)$ about 0. We shall use notation from [90] to write:

$$a_n = [x^n]\{a(x)\} \tag{5.5}$$

Thus we shall define the generating function of the Catalan numbers to be:

$$\mathcal{C}(x) = \sum_{n=0}^{\infty} C_n x^n \tag{5.6}$$

with the inverse relation

$$C_n = [x^n]\{\mathcal{C}(x)\} \tag{5.7}$$

Equation (5.6) can be squared to give:

$$\begin{aligned}\mathcal{C}^2(x) &= C_0^2 + (C_0C_1 + C_1C_0)\,x + \cdots (C_0C_n + C_1C_{n-1} + \cdots + C_nC_0)\,x^n + \cdots \\ &= C_1 + C_2x + C_3x^2 + \cdots C_{n+1}x^n + \cdots \\ &= \frac{\mathcal{C}(x) - C_0}{x} \end{aligned} \tag{5.8}$$

$$\Rightarrow \mathcal{C}(x) = x\mathcal{C}^2(x) + 1 \tag{5.9}$$

where we have used (5.1) to simplify the terms and the fact that $C_0 = 1$.

5.2 Depth of the First Leaf

The first numerical challenge was to determine the depth of the first leaf, that is the number of nodes that must be passed through on an n node tree to reach from the first leaf to the root node (including the root node itself). This problem is a combinatorial issue and well treated by the diagrammatic notation and simple algebra discussed above. However, using the generating functions described at the end of the previous section will stand us in good stead for heading onto further problems.

The more general case of this problem will be finding the depth of the m^{th} leaf, and $D_{m,n}$ is the depth function giving the total number of nodes that connect the m^{th} leaf to the root summed over all unique graphs with n nodes.

The depth of the first leaf can be expressed as the sum over sub-trees as shown in figure (5.2).

Notice that figure (5.2) shows that the depth of the first leaf of a sub tree on a given row is equal to the total depth of the row above plus the degeneracy of that row, equivalently:

$$d_{1,n} = D_{1,n-1} + C_{n-1} \tag{5.10}$$

However, to find the total depth for $m = 1$ for a given n it is necessary to sum over all sub tress and to take account of the degeneracies of the paired sub trees. For example, the right hand graph for $n = 3$ in figure (5.4), the $n = 0$ sub tree has a first leaf depth of 1 but is paired with a sub tree with $n = 2$, meaning that there are, in reality, two sub trees with n=0 whose first leg depth must be summed over.

Taking the degeneracy into account and summing over the sub trees in de-

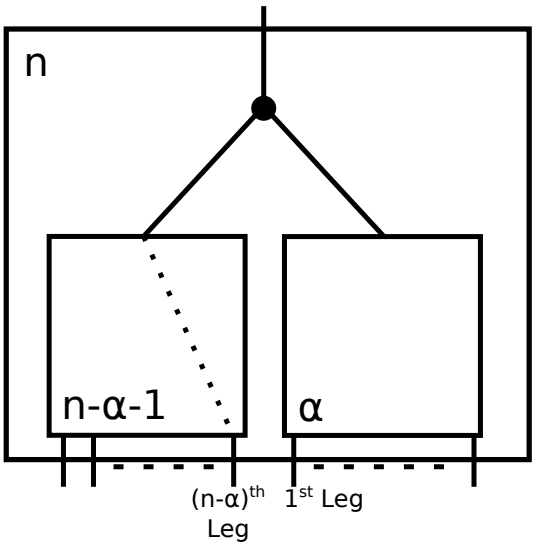

Figure 5.4: An n vertex tree split into a single vertex, an $n-\alpha-1$ vertex tree and an α vertex tree

creasing size, we obtain the relation:

$$\begin{aligned} D_{1,n} &= \sum_{k=0}^{n-1} [D_{1,n-1-k}C_k + C_{n-1-k}C_k] \\ &= \sum_{k=0}^{n-1} D_{1,n-1-k}C_k + C_n \end{aligned} \tag{5.11}$$

We shall use the term 'master equations' to describe all equations that define a given term by sums over combinations of Catalan numbers. To solve our first master equation we shall define the following generating function:

$$\mathcal{D}_1(x) = \sum_{n=0}^{\infty} D_{1,n}x^n \tag{5.12}$$

and we shall define $D_{1,0} = 0$ as there is no path length in a 0 node tree. We can multiply this by the generating function for Catalan numbers to give:

$$\begin{aligned}
\mathcal{D}_1(x)\mathcal{C}(x) &= D_{1,0}C_0 + (D_{1,0}C_1 + D_{1,1}C_0)\,x + \cdots + \\
&\qquad (D_{1,0}C_n + D_{1,1}C_{n-1} + \cdots + D_{1,n}C_0)\,x^n + \cdots \\
&= (D_{1,1} - C_1) + (D_{1,2} - C_2)\,x + \cdots + (D_{1,n+1} - C_{n+1})\,x^n + \cdots \\
&= \sum_{n=0}^{\infty} D_{1,n+1}x^n - \sum_{n=0}^{\infty} C_{n+1}x^n \\
&= \frac{(\mathcal{D}_1(x) - D_{1,0}) - (\mathcal{C}(x) - C_0)}{x}
\end{aligned}$$

$$\begin{aligned}
\Rightarrow \mathcal{D}_1(x) &= \mathcal{C}^2(x) + (D_{1,0} - C_0)\,\mathcal{C}(x) \\
&= \mathcal{C}^2(x) - \mathcal{C}(x)
\end{aligned} \tag{5.13}$$

This can be re-written in the style of a generating function:

$$\mathcal{D}_1(x) = \sum_{n=0}^{\infty} [C_{n+1} - C_n]\,x^n \tag{5.14}$$

which is equivalent to saying:

$$D_{1,n} = C_{n+1} - C_n \tag{5.15}$$

5.3 Depth of the Second Leaf

Moving beyond the depth first leaf means it is necessary to consider a more complicated situation as the second leaf is not always in the left hand sub tree as shown for the second leaf in figure (5.5). This gives us the master equation for the second leaf:

$$D_{2,n} = \sum_{k=1}^{n-1} D_{2,k}C_{n-1-k} + D_{1,n-1} + C_n \tag{5.16}$$

We shall again create a generating function, this time for the depth of the second leaf:

$$\mathcal{D}_2(x) = \sum_{n=1}^{\infty} D_{2,n}x^n \tag{5.17}$$

This time the sum starts at 1 as the depth cannot be defined for a tree with only one leaf.

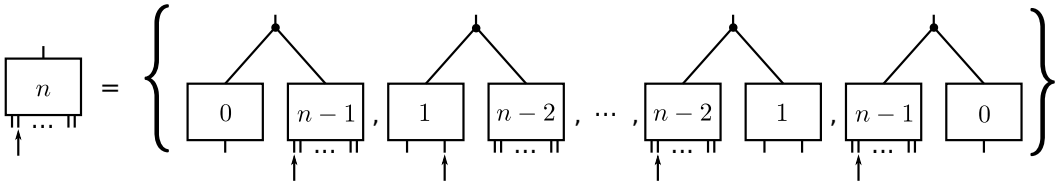

Figure 5.5: The decomposition of the set of trees with n nodes in terms of sub trees from the root. The second leaf is highlighted to show how it is no longer solely in the left hand sub tree, this will hold for any leaf at position m where $m \geq 2$

As before we shall multiply by the generating function for the Catalan numbers and compare to the master equation.

$$\begin{aligned}
\mathcal{D}_2(x)\mathcal{C}(x) &= D_{2,1}C_0x + (D_{2,1}C_1 + D_{2,2}C_0)\,x^2 + \cdots \\
&\qquad + (D_{2,1}C_{n-1} + \cdots + D_{2,n}C_0)\,x^n + \cdots \\
&= (D_{2,2} - D_{1,1} - C_2)\,x + \cdots + (D_{2,n+1} - D_{1,n} - C_{n+1})\,x^n + \cdots \\
&= \sum_{n=1}^{\infty} D_{2,n+1}x^n - \sum_{n=1}^{\infty} D_{1,n}x^n - \sum_{n=1}^{\infty} C_{n+1}x^n \\
&= \left[\frac{\mathcal{D}_2(c) - D_{2,1}x}{x}\right] - [\mathcal{D}_1(x) - D_{1,0}] - \left[\frac{\mathcal{C}(x) - C_1x - C_0}{x}\right] \qquad (5.18)
\end{aligned}$$

Using the same method to get from equation (5.6) to equation (5.9), we can see that we can write $\mathcal{D}_2(x) = x\mathcal{C}(x)\mathcal{D}_1(x) + \mathcal{C}^2(x) - \mathcal{C}(x)$ and $x\mathcal{D}_1(x) = \mathcal{C}(x) - x\mathcal{C}(x) - 1$. Using this with equation (5.18) we get:

$$\begin{aligned}
\mathcal{D}_2(x) &= 2\mathcal{C}^2(x) - 2\mathcal{C}(x) - x\mathcal{C}^2(x) && (5.19)\\
&= \sum_{n=0}^{\infty} [2C_{n+1} - 2C_n]\,x^n - \sum_{n=1}^{\infty} C_n c^n && (5.20)\\
&= \sum_{n=1}^{\infty} [2C_{n+1} - 3C_n]\,x^n && (5.21)
\end{aligned}$$

$$\Rightarrow D_{2,n} = 2C_{n+1} - 3C_n \qquad (5.22)$$

5.4 Solving the Depth of the m^{th} Leaf

To create a master equation for the depth of a general leaf we notice that there was one case for the second leaf where the leaf was not in the left hand sub tree and there will be $m-1$ cases for the m^{th} leaf. When the left sub tree has between $k=0$ and $k=m-2$ nodes then the contribution to the depth is from leaf $m-k-1$, as the left sub tree has $k+1$ leaves. The degeneracy of this term is simply C_k. When $k > m-2$, the m^{th} leaf is in the left hand sub tree as before. Thus we can write the full master equation as:

$$D_{m,n} = C_n + \sum_{k=m-1}^{n-1} D_{m,k} C_{n-1-k} + \sum_{k=0}^{m-2} D_{m-k-1,n-k-1} C_k \tag{5.23}$$

At this point we note that the depth function is symmetric, i.e. the depth of the m^{th} leaf from the left is the same as the depth of the m^{th} leaf from the right, this means $D_{m,n} \equiv D_{n+2-m,n}$. Thus a master equation for the p^{th} leaf from the right hand side can be given by:

$$D_{n+2-p,n} = C_n + \sum_{k=0}^{n-p} D_{n-k-p+1,n-k-1} C_k + \sum_{k=n-p+1}^{n-1} D_{n+2-p,k} C_{n-1-k} \tag{5.24}$$

where the first sum is for when the $(n+2-p)^{\text{th}}$ leaf is $(n-k-p+1)$ leaves into the right hand sub tree. The second sum is when the left hand sub tree has at least $n-2-p$ leaves. The degeneracies in each case are given by the number of leaves in the opposite sub tree as before. It can be shown that equation (5.24) is equivalent to (5.23) by simply substituting $m = n+2-p$.

It should also be noted that, as was seen when $m=2$, it is necessary to start the sum in the generating function at $m-1$, giving a generating function for the depth of the m^{th} leaf of:

$$\mathcal{D}_m(x) = \sum_{n=m-1}^{\infty} D_{m,n} x^n \tag{5.25}$$

Adapting the general master equation to be for the case $D_{m,n+m}$, we see:

$$D_{m,n+m} = C_{n+m} + \sum_{k=m-1}^{n+m-1} D_{m,k} C_{n+m-1-k} + \sum_{k=0}^{m-2} D_{m-k-1,n+m-k-1} C_k \tag{5.26}$$

which, using the same methodology as before, gives the relation:

$$\mathcal{D}_m(x) = \mathcal{C}^2(x) - \mathcal{C}(x)\sum_{n=0}^{m-1} C_n x^n + \mathcal{C}(x) D_{1,m-1} x^{m-1} + \mathcal{C}(x)\sum_{k=0}^{m-2} C_k x^{k+1}\left[\mathcal{D}_{m-k-1}(x) - D_{1,m-k-2}x^{m-k-2}\right] \tag{5.27}$$

This shows that is it only necessary to know the depth of the first leaf to create a generating function for the m^{th} leaf. This changes equation (5.27) to:

$$\mathcal{D}_m(x) = \mathcal{C}^2(x) - \mathcal{C}(x)\sum_{n=0}^{m-1} C_n x^n + \mathcal{C}(x)\left(C_m - C_{m-1}\right)x^{m-1} + \mathcal{C}(x)\sum_{k=0}^{m-2} C_k x^{k+1}\left(\mathcal{D}_{m-k-1}(x) - \left(C_{m-k-1} - C_{m-k-2}\right)x^{m-k-2}\right) \tag{5.28}$$

We can also adapt equation (5.1) to give the following relations that will allow us to simplify (5.28):

$$\sum_{k=0}^{m-2} C_k C_{m-k-2} = C_{m-1} \tag{5.29}$$

$$\sum_{k=0}^{m-2} C_k C_{m-k-1} = \sum_{k=0}^{m-1} C_k C_{m-k-1} - C_{m-1}C_0 = C_m - C_{m-1} \tag{5.30}$$

This lets us write:

$$\mathcal{D}_m(x) = \mathcal{C}^2(x) - \mathcal{C}(X)\sum_{n=0}^{m-1} C_n x^n + \mathcal{C}(x) C_{m-1} x^{m-1} + \mathcal{C}(x)\sum_{k=0}^{m-2} C_k x^{k+!}\mathcal{D}_{m-k-1}(x) \tag{5.31}$$

As we already have a relation for $m = 1$, we shall take $m \geq 2$ and simplify further:

$$\mathcal{D}_m(x) = \mathcal{C}^2(x) - \mathcal{C}(X)\sum_{n=0}^{m-2} C_n x^n - \mathcal{C}(x)C_{m-1}x^{m-1}$$
$$\mathcal{C}(x)C_{m-1}x^{m-1} + \mathcal{C}(x)\sum_{k=0}^{m-2} C_k x^{k+1}\mathcal{D}_{m-k-1}(x) \tag{5.32}$$

$$\mathcal{D}_m(x) = \mathcal{C}^2(x) + \mathcal{C}(x)\sum_{n=0}^{m-2} C_n x^n \left[x\mathcal{D}_{m-n-1}(x) - 1\right] \tag{5.33}$$

This is tantalisingly close to a general solution, we shall introduce an ansatz that assumes that the generating function $\mathcal{D}_m(x)$ may be written as:

$$\mathcal{D}_m(x) = f_m(x)\mathcal{C}(x) + g_m(x) \tag{5.34}$$

where $f_m(x)$ and $g_m(x)$ are polynomial in x and are of order $m-2$. The ansatz was motivated by noticing that for $m \geq 2$, $D_{m,n}$ is composed of a sum of Catalan numbers with indices from $n-(m-2)$ to $n+1$, thus the form of $f_m(x)\mathcal{C}(x)$ gives the expression for $D_{m,n}$. When putting it in the form of equation (5.23) there are extra terms which are part of $g_m(x)$.

This allows us to solve (see Appendix A):

$$D_{m,n} = mC_{n+1} - C_n - 2\sum_{k=0}^{m-2}(m-k-1)\,C_k C_{n-k} \tag{5.35}$$

Which means that this expression explicitly gives:

$$D_{m,n} = mC_{n+1} - C_n - \frac{2(2n+1)mC_n}{n+2}$$
$$+ \frac{m(m+1)C_m(2n-2m+3)(n-m+2)C_{n-m+1}}{(n+1)(n+2)} \tag{5.36}$$
$$= \frac{2m(m+1)(2n-2m+1)(2n-2m+3)}{(n+1)(n+2)}C_m C_{n-m} - C_n \tag{5.37}$$

5.5 Leaf to Leaf Paths

We now move to considering the number of nodes connecting two leaves with separation r, taking the sum of all paths over all leaves with separation r for all unique trees with n nodes we get the value $S_n(r)$ which can be divided by the total number

of paths to give the to give the average leaf to leaf path length $A_n(r)$.

Investigating the path length for $r = 1$ we split an n node tree into two sub trees of size α and $(n - \alpha - 1)$. For the tree with α nodes, the path length is S_α (we drop the descriptor of length for convenience) while for the $(n - \alpha - 1)$ path it is $S_{n-\alpha-1}$. There is one final path to consider, that between the two trees connecting the $(n - \alpha)^{\text{th}}$ leaf of the $(n - \alpha - 1)$ tree to the first leaf of the α tree. The depth of the latter is simply $D_{1,\alpha}$ as given by equation (5.27). This path must be summed over $C_{n-\alpha-1}$ times due to the degeneracy of the left hand sub tree; similarly, the depth of the $(n - \alpha)^{\text{th}}$ vertex is $D_{n-\alpha,n-\alpha-1}$ and this must be multiplied by the degeneracy C_α. The final consideration is that to connect these two paths we must go through the root node, adding 1 to the length each time, but this must be multiplied by both degeneracies thus giving a total sum of:

$$C_\alpha D_{n-\alpha,n-\alpha-1} + C_{n-\alpha-1} D_{1,\alpha} + C_{n-\alpha-1} C_\alpha \tag{5.38}$$

Finally, to get the total result we must sum over contributions from all sizes of sub trees giving:

$$\begin{aligned} S_n(1) = \sum_{\alpha=0}^{n-1} [&C_\alpha D_{n-\alpha,n-\alpha-1} + C_{n-\alpha-1} D_{1,\alpha} C_{n-\alpha-1} C_\alpha \\ &+ S_{n-\alpha-1}(1) C_\alpha + S_\alpha(1) C_{n-\alpha-1}] \end{aligned} \tag{5.39}$$

This may be simplified to:

$$\begin{aligned} S_n(1) &= 2C_{n+1} - 3C_n + 2\sum_{\alpha=0}^{n-1} S_\alpha(1) C_{n-\alpha-1} \\ &= D_{2,n} + 2\sum_{\alpha=0}^{n-1} S_\alpha(1) C_{n-\alpha-1} \end{aligned} \tag{5.40}$$

We shall again make use of generating functions, this time defining:

$$\mathcal{S}(1, x) = \sum_{n=0}^{\infty} S_n(1) x^n \tag{5.41}$$

with the additional definition $S_0 = 0$, this then allows us to describe the master equation as:

$$
\begin{aligned}
\mathcal{S}(1,x) &= \sum_{n=0}^{\infty} S_{n+1}(1)x^{n+1} \\
&= 2\sum_{n=0}^{\infty} C_{n+2}x^{n+1} - 3\sum_{n=0}^{\infty} C_{n+1}x^{n+1} + 2\sum_{n=0}^{\infty}\sum_{\alpha=0}^{n} S_\alpha(1)C_{n-\alpha}x^{n+1} \\
&= \frac{2}{x}\left(\sum_{n=0}^{\infty} C_n x^n - C_0 - C_1 x\right) - 3\left(\sum_{n=0}^{\infty} C_n x^n - C_0\right) \\
&\qquad + 2x\sum_{n=0}^{\infty}\sum_{\alpha=0}^{n} S_\alpha(1)C_{n-\alpha}x^{n-\alpha}x^\alpha \\
&= \frac{2}{x}\left[\mathcal{C}(x) - 1\right] - 2 - 3\mathcal{C}(x) + 3 + 2x\sum_{q=-\alpha}^{\infty}\sum_{\alpha=0}^{\infty} H_q C_q x^q S_\alpha(1)x^\alpha \\
&= \frac{2}{x}\left[\mathcal{C}(x) - 1\right] + 1 - 3\mathcal{C}(x) + 2x\sum_{q=0}^{\infty}\sum_{\alpha=0}^{\infty} C_q x^q S_\alpha(1)x^\alpha \\
&= \frac{2}{x}\left[\mathcal{C}(x) - 1\right] + 1 - 3\mathcal{C}(x) + 2x\mathcal{S}(1,x)\mathcal{C}(x) \qquad (5.42)
\end{aligned}
$$

where H_q is a step function with $H_q = 1$ if $q \geq 0$, and 0 otherwise. Solving for $\mathcal{S}$ and simplifying we get:

$$
\begin{aligned}
\mathcal{S}(1,x) &= \frac{\frac{2}{x}\left[\mathcal{C}(x) - 1\right] + 1 - 3\mathcal{C}(x)}{1 - 2x\mathcal{C}(x)} \\
&= \frac{2\mathcal{C}^2(x) - 3\mathcal{C}(x) + 1}{\sqrt{1-4x}} \\
&= \sum_{n]0}^{\infty} \left[2(n+1)C_{n+1} - 3(2n+1)C_n + (n+1)C_n\right] x^n \qquad (5.43)
\end{aligned}
$$

Which is simplified using the definition definition [90] that:

$$
\mathcal{C}(x) = \frac{1 - \sqrt{1-4x}}{2x} \qquad (5.44)
$$

and the following three relations which are derived from it:

$$\begin{aligned}\sum_{\alpha=0}^{\infty}(\alpha+1)C_\alpha x^\alpha &= \mathcal{C}(x) + x\frac{\partial}{\partial x}\mathcal{C}(x) \\ &= \frac{1-\sqrt{1-4x}}{2x} + \left[\frac{1}{\sqrt{1-4x}} - \frac{1-\sqrt{1-4x}}{2x}\right] \\ &= \frac{1}{\sqrt{1-4x}} \end{aligned} \tag{5.45}$$

$$\begin{aligned}\frac{\mathcal{C}(x)}{\sqrt{1-4x}} &= \sum_{\alpha=0}^{\infty} C_\alpha x^\alpha \sum_{\beta=0}^{\infty}(\beta+1)C_\beta x^\beta \\ &= \sum_{\alpha,\beta=0}^{\infty}(\beta+1)C_\alpha C_\beta x^{\alpha+\beta} \\ &= \sum_{n=0}^{\infty}\sum_{\beta=0}^{n}(\beta+1)C_{n-\beta}C_\beta x^n \\ &= \sum_{n=0}^{\infty}(2n+1)C_n x^n \end{aligned} \tag{5.46}$$

$$\begin{aligned}\frac{\mathcal{C}^2(x)}{\sqrt{1-4x}} &= \mathcal{C}(x)\left(\frac{\mathcal{C}(x)}{\sqrt{1-4x}}\right) \\ &= \sum_{\alpha=0}^{\infty} C_\alpha x^\alpha \sum_{\beta=0}^{\infty}(2\beta+1)C_\beta x^\beta \\ &= \sum_{\alpha,\beta=0}^{\infty}(2\beta+1)C_\alpha C_\beta x^{\alpha+\beta} \\ &= \sum_{n=0}^{\infty}\sum_{\beta=0}^{n}(2\beta+1)C_{n-\beta}C_\beta x^n \\ &= \sum_{n=0}^{\infty}(n+1)C_{n+1}x^n \end{aligned} \tag{5.47}$$

Therefore, the n^{th} term of this $(S_n(1) = [x^n]\{\mathcal{S}(1,x)\}$ is simply:

$$\begin{aligned}S_n(1) &= 2(n+1)C_{n+1} - (5n+2)C_n \\ &= \frac{3n^2 C_n}{n+2} \end{aligned} \tag{5.48}$$

Given that there are n paths per tree and a degeneracy of C_n trees, the average path length then becomes:

$$A_n(1) = \frac{3n}{n+2} \tag{5.49}$$

5.6 Further Investigations

For the curious reader, my collaborators continued on this path to find the path lengths for $S_n(2)$ and we managed to create a master equation for general separation, however solving this equation was decidedly non-trivial. Inviting in a new collaborator who had more experience with generating functions meant he was able to create a diagrammatic algebra and find a general solution for both $S_n(r)$ and $A_n(r)$. The work may all be found in reference [88].

Chapter 6

Conclusions and Future Work

In this thesis I have shown how one may start the process of investigating a cooling cycle with classical thermodynamics, building on this with the use of statistical mechanics to produce a mean field spin model that couples to a thermal model of a solid to describe the electrocaloric effect in relaxor ferroelectrics. Greater understanding of the physics behind the electrocaloric effect will open wide the possibility of cheaper and greener cooling on both an industrial and residential level, potentially reducing the cost of home refrigeration by up to half over the lifetime of a unit and removing the greenhouse effect caused by current refrigerants.

The literature has shown that disorder is a key feature in the description and modelling of relaxors and that spin models are well suited to simulate the electrocaloric effect. I reproduced work from two groups (Vives et al. [16] and Valant et al. [31]) to gain insight into where the state of the filed lies with regards to modelling. I used a model based on the work of Vives et al. to examine the disorder in a relaxor polymer, observing the effect that random bonds and random fields have on polarisation-hysteresis loops and matching the output of simulations to experiment. Based on the work of Valant et al. I produced a spin model on a lattice that is able to give a strong qualitative description of the effect of the application and removal of an external field on the magnetocaloric iron rhodium.

The model produced in my work is able to investigate first and second order transitions as well as search for tri-critical points, it is able to produce a strong, qualitative result on the effects of varying disorder (as may be experimentally implemented by changing the method of production of the refrigerant) or changing interaction strengths (examined experimentally by doping with other materials). A methodology is set up that is able to produce reliable comparisons between materials requiring only a limited number of input parameters. The strength of this

work is to show that complex systems, such as relaxor ferroelectrics, may indeed be modelled in a simple and general way and electrocaloric effect can be given a strong qualitative description with a very limited number of input parameters. I predicted the strength of the electrocaloric effect in polyvinylidene fluoride trifluoroethylene, P(VDF-TrFE), obtaining material parameters through the comparison of simulated polarisation-electric field hysteresis loops with experimental ones. With these material parameters it was possible to calculate the entropy and free energy of disordered P(VDF-TrFE) and determine that, due to the large electric breakdown strength, it is a refrigerant worth investigating as the potential adiabatic temperature change at room temperature under large fields could be enough to replace conventional refrigerants.

There have, unfortunately, been no publications as a result of the work on this thesis, although chapter (5), which is an aside to the main project, has a paper being written which we are hoping to publish.

There are several possible courses for the future direction of research in this area, the obvious first suggestions are to calibrate the model of section 4.3 to results for P(VDF-TrFE) when they are available and to work on improving the model from section 4.4 such that the results become not only qualitatively correct but can also directly reproduce results seen for iron rhodium in experiment. Another possibility is to continue on with the strong qualitative handle on the effects of disorder on the isothermal entropy and adiabatic temperature change of a caloric material. A lattice model where different lattice sites could be given different interaction strengths would allow for a more complex treatment of disordered systems, regions of chemical imbalance could be directly specified rather than implicitly taken in the averaging that is done now. This would allow for more flexibility and control over the disorder in the material and would be a strong starting point for evaluating the effects of local and long range interactions in an inhomogeneous medium. With such a model it would be possible to examine phase segregated regions, local impurity clusters embedded within the material (as described by [32]). This would allow exploration of the phenomenon of phase coexistence (when an embedded material can exist in a ferroelectric state within an embedding material in an antiferroelectric state) and the effects on transition temperature and the isothermal entropy and adiabatic temperature changes of the disordered material.

Another potential model of interest to explore would be a two spin model with two interaction scales to represent the two temperature scales of PNR formation and freezing. Such a model could allow a simple insight into the complicated mechanisms behind relaxors and the effect that these length scales have on the electrocaloric

effect.

Appendix A

Temperature Dependence of Maximum Applied Field Strength in Hysteresis Loops

In figure (A.1) we have used the Monte Carlo Method [91] at three different temperatures ($0.5T_C$, $0.75T_C$ and $0.9T_C$, for comparison, the experimental hysteresis loops were measured at room temperature which is $0.75T_C$ for P(VDF-TrFE)) to include the thermal fluctuations. The output of these simulations show that including thermal fluctuations reduces this difference to a factor of around 2, this is a reasonable discrepancy for simulation. The extra computing cost of simulating the hysteresis loops with Monte Carlo Methods justifies the use of mean field theory as these calculations are faster and produce equivalently shaped hysteresis loops, the error in the maximum applied field strength does not affect the measure of disorder and thus is unimportant to the measurement.

The system was set up such that a 2-dimensional lattice was modelled with the interaction strength between pairs of sites being set to 1. The code selects a random site (using the Well random number generator: www.iro.umontreal.ca/ panneton/WELLRNG.html) trials a flip on the site by computing the energy cost of making such a move, calculating the probability given by the Boltzmann distribution and allowing the move if its probability is greater than a randomly generated number. One pass through the lattice is made when as many sites have been selected as there are sites in the lattice (note that as sites are selected randomly this means that some sites may not be selected in any given pass). The system was given 5000 passes to equilibrate and a further 5000 passes for measurements.

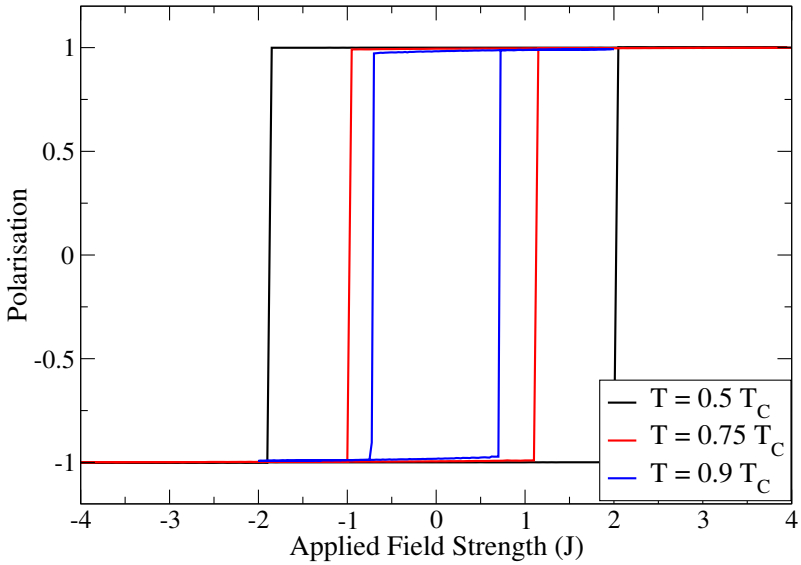

Figure A.1: Polarisation hysteresis loop of a disordered 3D cubic lattice of Ising spins with $\sigma_{R.B.} = 1$ and $\sigma_{R.F.} = 1.5$. This is simulated to represent a hysteresis loop of P(VDF-TrFE), seen in figure (4.4). Using the Monte Carlo method we have simulated the system at three different temperatures: ($0.5T_C$, $0.75T_C$ and $0.9T_C$

Appendix B

Solving the Depth of the m^{th} Leaf

This appendix relates to chapter (5) and has no relevance to the theme of theoretical modelling of a solid state cooling cycle.

We drop the index in equation (5.26) on the first sum to zero and introduce a step function ($H_p = 1$ if $p \geq 0$ and 0 otherwise) so that the upper limit can go to infinity:

$$D_{m,n+m} = C_{n+m} + \sum_{k=0}^{\infty} D_{m,k+m-1} C_{n-k} H_{n-k} + \sum_{k=0}^{m-2} D_{m-k-1,n+m-k-1} C_k \qquad \text{(B.1)}$$

Multiply both sides by x^{m+n} and sum from $n = 0$ to ∞ to match the generating function. Note that we use $n + m$ rather than $n + m - 1$ as in the generating function so that the index on the Catalan numbers is never negative.

$$\begin{aligned}\sum_{n=0}^{\infty} D_{m,n+m} x^{n+m} = \sum_{n=0}^{\infty} C_{n+m} x^{n+m} + \sum_{n=0}^{\infty} \sum_{k=0}^{\infty} D_{m,k+m-1} C_{n-k} H_{n-k} x^{n+m} \\ + \sum_{n=0}^{\infty} \sum_{k=0}^{m-2} D_{m-k-1,n+m-k-1} C_k x^{n+m} \qquad \text{(B.2)}\end{aligned}$$

The left hand side can clearly be expressed in terms of $\mathcal{D}_m(x)$:

$$\begin{aligned}\sum_{n=0}^{\infty} D_{m,n+m}x^{m+n} &= \sum_{n=1}^{\infty} D_{m,n+m-1}x^{n+m-1} \\ &= \sum_{n=0}^{\infty} D_{m,n+m-1}x^{n+m-1} - D_{m,m-1}x^{m-1} \\ &= \mathcal{D}_m(x) - D_{m,m-1}x^{m-1} \end{aligned} \tag{B.3}$$

The first term on the right can be written in terms of $\mathcal{C}(x)$ as

$$\begin{aligned}\sum_{n=0}^{\infty} C_{n+m}x^{n+m} &= \sum_{n=m}^{\infty} C_n x^n \\ &= \sum_{n=0}^{\infty} C_n x^n - \sum_{n=0}^{m-1} C_n x^n \\ &= \mathcal{C}(x) - \sum_{n=0}^{m-1} C_n x^n \end{aligned} \tag{B.4}$$

The second term can also be written in terms of generating functions:

$$\begin{aligned}\sum_{n=0}^{\infty}\sum_{k=0}^{\infty} D_{m,k+m-1}C_{n-k}H_{n-k}x^{n+m} &= \sum_{k=0}^{\infty} D_{m,k+m-1}x^{m+k}\sum_{n=0}^{\infty} C_{n-k}H_{n-k}x^{n-k} \\ &= x\sum_{k=0}^{\infty} D_{m,k+m-1}x^{k+m-1}\sum_{l=-k}^{\infty} C_l H_l x^l \\ &= x\mathcal{D}_m(x)\mathcal{C}(x) \end{aligned} \tag{B.5}$$

where we have used $l = n - k$ on the second line. The final term is similarly

$$\begin{aligned}\sum_{n=0}^{\infty}\sum_{k=0}^{m-2} D_{m-k-1,n+m-k-1}C_k x^{n+m} &= \sum_{k=0}^{m-2} C_k x^{k+1}\sum_{n=0}^{\infty} D_{m-k-1,n+m-k-1}x^{n+m-k-1} \\ &= \sum_{k=0}^{m-2} C_k x^{k+1}\left(\sum_{n=0}^{\infty} D_{m-k-1,n+m-k-2}x^{n+m-k-2}\right. \\ &\qquad \left. -D_{m-k-1,m-k-2}x^{m-k-2}\right) \\ &= \sum_{k=0}^{m-2} C_k x^{k+1}\left(\mathcal{D}_{m-k-1}(x)\right. \\ &\qquad \left. -D_{m-k-1,m-k-2}x^{m-k-2}\right) \end{aligned} \tag{B.6}$$

When put together this gives

$$\begin{aligned}\mathcal{D}_m(x) - D_{m,m-1}x^{m-1} = \mathcal{C}(x) - \sum_{n=0}^{m-1} C_n x^n + x\mathcal{D}_m(x)\mathcal{C}(x) \\ + \sum_{k=0}^{m-2} C_k x^{k+1}\left(\mathcal{D}_{m-k-1}(x) - D_{m-k-1,m-k-2}x^{m-k-2}\right)\end{aligned} \tag{B.7}$$

Collecting the $\mathcal{D}_m(x)$ on the left then using equation (5.6) and $D_{m,n} = D_{n+2-m,n}$ results in equation (5.27).

We now continue from equation (5.34). We start by writing

$$x^m\mathcal{C}(x) = \sum_{n=0}^{\infty} C_n x^{n+m} = \sum_{k=m}^{\infty} C_{n-m}x^n \tag{B.8}$$

Inserting equation (5.34) gives

$$f_m(x)\mathcal{C}(x) + g_m(x) = \mathcal{C}^2(x) + \mathcal{C}(x)\sum_{n=0}^{m-2} C_n x^n\left[x f_{m-n-1}(x)\mathcal{C}(x) + x g_{m-n-1}(x) - 1\right] \tag{B.9}$$

In the spirit of the ansatz we use equation (5.9) to remove the $\mathcal{C}^2(x)$ terms and make the expression dependent on just $\mathcal{C}(x)$:

$$f_m(x)\mathcal{C}(x) + g_m(x) = \frac{\mathcal{C}(x)}{x} - \frac{1}{x} + \mathcal{C}(x)\sum_{n=0}^{m-2} C_n x^n \left[x g_{m-n-1}(x) - 1\right] + (\mathcal{C}(x) - 1)\sum_{n=0}^{m-2} C_n x^n f_{m-n-1}(x)\mathcal{C}(x) \tag{B.10}$$

Collecting coefficients of $\mathcal{C}(x)$ gives

$$f_m(x) = \frac{1}{x} + \sum_{n=0}^{m-2} C_n x^n \left[f_{m-n-1}(x) + x g_{m-n-1}(x) - 1\right] \tag{B.11}$$

leaving

$$g_m(x) = -\frac{1}{x} - \sum_{n=0}^{m-2} C_n x^n f_{m-n-1}(x) \tag{B.12}$$

We can now write out $f_m(x)$ and $g_m(x)$ for the first few m. Recall that the above expressions are only valid for $m \geq 2$, we therefore obtain $f_1(x)$ and $g_1(x)$ from equation (5.13) to seed the other terms. The first seven $f_m(x)$ are:

$$\begin{aligned}
f_1(x) &= \frac{1}{x} - 1 \\
f_2(x) &= \frac{2}{x} - 3 \\
f_3(x) &= \frac{3}{x} - 5 - 2x \\
f_4(x) &= \frac{4}{x} - 7 - 4x - 4x^2 \\
f_5(x) &= \frac{5}{x} - 9 - 6x - 8x^2 - 10x^3 \\
f_6(x) &= \frac{6}{x} - 11 - 8x - 12x^2 - 20x^3 - 28x^4 \\
f_7(x) &= \frac{7}{x} - 13 - 10x - 16x^2 - 30x^3 - 56x^4 - 84x^5
\end{aligned}$$

and for $g_m(x)$

$$
\begin{aligned}
g_1(x) &= -\frac{1}{x} \\
g_2(x) &= -\frac{2}{x} + 1 \\
g_3(x) &= -\frac{3}{x} + 2 + x \\
g_4(x) &= -\frac{4}{x} + 3 + 3x + 2x^2 \\
g_5(x) &= -\frac{5}{x} + 4 + 5x + 7x^2 + 5x^3 \\
g_6(x) &= -\frac{6}{x} + 5 + 7x + 12x^2 + 19x^3 + 14x^4 \\
g_7(x) &= -\frac{7}{x} + 6 + 9x + 17x^2 + 33x^3 + 56x^4 + 42x^5
\end{aligned}
$$

It is possible to spot patterns in these equations and write a general formula for each

$$
\begin{aligned}
f_m(x) &= \frac{m}{x} - 1 - 2H_{m-2}C_0(m-1)2H_{m-3}C_1(m-2)x - 2H_{m-4}C_2(m-3)x^2 \\
&\qquad - 2H_{m-5}C_3(m-4)x^3 - \cdots \\
&= \frac{m}{x} - 1 - 2\sum_{k=0}^{m-2}(m-k-1)C_k x^k \\
g_m(x) &= -\frac{m}{x} + H_{m-2}\left(C_1(m-2) + C_0\right) + H_{m-3}\left(C_2(m-3) + C_1\right)x \\
&\qquad + H_{m-4}\left(C_3(m-4) + C_2\right)x^2 + H_{m-5}\left(C_4(m-5) + C_3\right)x^3 + \cdots \\
&= -\frac{m}{x} + \sum_{k=0}^{m-2}\left[(m-k-2)C_{k+1} + C_k\right]x^k
\end{aligned} \tag{B.13}
$$

In the first lines of each a step function H_p has been introduced to cut the expression so that it gives only the terms allowed for that m. This is neatly included within the summations in the final forms. Finally we multiply our expression for $f_m(x)$ by $\mathcal{C}(x)$ using equation (B.8) yields

$$
\begin{aligned}
f_m(x)\mathcal{C}(x) &= \sum_{n=0}^{\infty}\left[\frac{m}{x} - 1 - 2\sum_{k=0}^{m-2}(m-k-1)C_k x^k\right] C_n x^n \\
&= \sum_{n=m-1}^{\infty}\left[mC_{n+1} - C_n - 2\sum_{k=0}^{m-2}(m-k-1)C_k C_{n-k}\right] x^n \\
&\quad + m\sum_{n=-1}^{m-2} C_{n+1}x^n - \sum_{n=0}^{m-2} C_n x^n - 2\sum_{k=0}^{m-2}\sum_{n=k}^{m-2}(m-k-1)C_k C_{n-k}x^n
\end{aligned}
\tag{B.14}
$$

This implies equation (5.35). We now just have to show that the rest of the terms are taken care of by $g_m(x)$. Using the double sum identity:

$$
\sum_{a=0}^{c}\sum_{b=a}^{c} M_{a,b} = \sum_{b=0}^{c}\sum_{a=0}^{b} M_{a,b} \tag{B.15}
$$

where a, b, $c \in \mathbb{Z}_+$, the final term in equation (B.14) can be simplified:

$$
\begin{aligned}
\sum_{k=0}^{m-2}\sum_{n=k}^{m-2}(m-k-1)C_k C_{n-k}x^n &= \sum_{n=0}^{m-2}\sum_{k=0}^{n}(m-k-1)C_k C_{n-k}x^n \\
&= \sum_{n=0}^{m-2}\sum_{k=0}^{n}\left[mC_k C_{n-k} - (k+1)C_k C_{n-k}\right] x^n \\
&= \sum_{n=0}^{m-2}\left[mC_{n+1} - (2n+1)C_n\right] x^n
\end{aligned}
\tag{B.16}
$$

and in the final line we have used Segner's relation on the first term. Thus equation (B.14) can be written as:

$$
\begin{aligned}
f_m(x)\mathcal{C}(x) = \sum_{n=m-1}^{\infty} D_{m,n}x^n + \frac{m}{x} \\
- \sum_{n=0}^{m-2}\left[C_n - mC_{n+1} + 2mC_{n+1} - 2(2n+1)C_{n+1}\right] x^n
\end{aligned}
\tag{B.17}
$$

Using the recursion relation for Catalan number (equation (5.2)) then gives:

$$
\begin{aligned}
f_m(x)\mathcal{C}(x) &= \sum_{n=m-1}^{\infty} D_{m,n}x^n + \frac{m}{x} - \sum_{n=0}^{m-2} \left[C_n + mC_{n+1} - (n+2)C_{n+1}\right] x^n \\
&= \sum_{n=m-1}^{\infty} D_{m,n}x^n + \frac{m}{x} - \sum_{n=0}^{m-2} \left[(m-n-2)C_{n+1} + C_n\right] x^n \\
&= \mathcal{D}_m(x) - g_m(x) \qquad \text{(B.18)}
\end{aligned}
$$

as desired.

Bibliography

[1] J. Hodson, "The repertory of patent inventions, and other discoveries and improvements in arts, manufactures, and agriculture, new series - vol vii," 1834. https://books.google.co.uk/books?id=80oEAAAAQAAJ&pg=PA192&lpg=PA192&dq=apparatus+and+means+for+producing+ice+and+in+cooling+fluids&source=bl&ots=o-mx7QqWCM&sig=LBdaDWwO1u5RjKbtgRT8oTkco3w&hl=en&sa=X&sqi=2&ved=0CCcQ6AEwAWoVChMIq8i017nsxgIVygrbCh2HkQkR#v=onepage&q=apparatus%20and%20means%20for%20producing%20ice%20and%20in%20cooling%20fluids&f=false.

[2] K. Sandeman, "Gas-free refrigeration," *Magnetics Technology International*, vol. 1, pp. 30–31, 2011.

[3] M. Valant, "Electrocaloric materials for future solid-state refrigeration technologies," *Progress in Materials Science*, vol. 57, no. 6, pp. 980–1009, 2012.

[4] G. J. M. Velders, D. W. Fahey, J. S. Daniel, M. Mcfarland, and S. O. Andersen, "The large contribution of projected HFC emissions to future climate forcing," *Proceedings of The National Academy of Sciences of the United States of America*, vol. 106, no. 27, pp. 10949–10954, 2009.

[5] United States Environmental Protection Agency, "National greenhouse gas emissions data: Draft inventory of U.S. greenhouse gas emissions and sinks 1990-2013," 2015.

[6] Department for Environment, Food and Rural Affairs, "Fluorinated greenhouse gases (F gases) regulated by the EU," 2014.

[7] M. M. Vopson, "Theory of giant-caloric effects in multiferroic materials," *Journal of Physics D: Applied Physics*, vol. 46, p. 345304, 2013.

[8] European Commission, "Gas-free refrigeration," 2011.

[9] B. Shen, J. R. Sun, F. X. Hu, H. W. Zhang, and Z. H. Cheng, "Recent progress in exploring magnetocaloric materials," *ArXiv Pre-Print*, p. 45, 2010.

[10] S.-G. Lu, B. Rožič, Q. M. Zhang, Z. Kutnjak, R. Pirc, M. Lin, X. Li, and L. Gorny, "Comparison of directly and indirectly measured electrocaloric effect in relaxor ferroelectric polymers," *Appl. Phys. Lett.*, vol. 97, no. 20, p. 202901, 2010.

[11] J. Valasek, "Piezoelectric and Allied Phenomena in Rochelle Salt," *Phys. Rev.*, vol. 15, no. 6, pp. 537–538, 1920.

[12] P. Kobeko and I. V. Kurtchatov, "Dielectric properties of rochelle salt crystal," *Z. Phys*, vol. 66, pp. 192–205, 1930.

[13] E. Warburg, "Magnetische untersuchungen," *Ann. Phys. (Leipzig)*, vol. 13, p. 141, 1881.

[14] G. S. Zhdanov, *Crystal Physics*. Oliver & Boyd, 1965.

[15] R. A. Cowley, S. N. Gvasaliya, S. G. Lushnikov, B. Roessli, and G. M. Rotaru, "Relaxing with relaxors: A review of relaxor ferroelectrics," *Advances in Physics*, vol. 60, no. 2, pp. 229–327, 2011.

[16] E. Vives and A. Planes, "Hysteresis and Avalanches in Disordered Systems," *Journal of Magnetism and Magnetic Materials*, vol. 221, pp. 164–171, 2000.

[17] Z.-K. Liu, X. Li, and Q. M. Zhang, "Intrinsic electrocaloric effect in ferroelectric alloys from atomistic simulations," *Phys. Rev. B*, vol. 80, p. 140102(R), 2012.

[18] B. Neese, B. Chu, S.-G. Lu, Y. Wang, E. Furman, and Q. M. Zhang, "Large electrocaloric effect in ferroelectric polymers near room temperature.," *Science*, vol. 321, no. 5890, pp. 821–823, 2008.

[19] X. Li, X.-S. Qian, H. Gu, X. Chen, S.-G. Lu, M. Lin, F. Bateman, and Q. M. Zhang, "Giant electrocaloric effect in ferroelectric poly(vinylidenefluoride-trifluoroethylene) copolymers near a first-order ferroelectric transition - supplementary material," *Appl. Phys. Lett.*, vol. 101, no. 13, 2012.

[20] B. Li, J. B. Wang, X. L. Zhong, Y. K. Zeng, and Y. C. Zhou, "The coexistence of the negative and positive electrocaloric effect in ferroelectric thin films for solid-state refrigeration," *Europhysics Letters*, vol. 102, no. 4, p. 47004, 2013.

[21] X. Moya, S. Kar-Narayan, and N. D. Mathur, "Caloric materials near ferroic phase transitions," *Nature Materials*, vol. 13, no. 5, pp. 439–450, 2014.

[22] I. Ponomareva and S. Lisenkov, "Bridging the macroscopic and atomistic descriptions of the electrocaloric effect," *Phys. Rev. Lett.*, vol. 108, no. 16, p. 167604, 2012.

[23] J. Hagberg, A. Uusimäki, and H. Jantunen, "Electrocaloric characteristics in reactive sintered $0.87Pb(Mg_{13}Nb_{23})O_30.13PbTiO_3$," *Appl. Phys. Lett.*, vol. 92, no. 13, p. 132909, 2008.

[24] B. Peng, H. Fan, and Q. Zhang, "A giant electrocaloric effect in nanoscale antiferroelectric and ferroelectric phases coexisting in a relaxor $Pb_{0.8}Ba_{0.2}ZrO_3$ thin film at room temperature," *Ad. Func. Mat.*, pp. 1–6, 2013.

[25] J. Perantie, J. Hagberg, A. Uusimaki, and H. Jantunen, "Electric-field-induced dielectric and temperature changes in a ⟨011⟩-oriented $Pb(Mg_{1/3}Nb_{2/3})O_3$-$PbTiO_3$ single crystal," *Phys. Rev. B*, vol. 82, no. 13, p. 134119, 2010.

[26] R. Pirc, R. Blinc, V. Bobnar, and A. Gregorovic, "Spherical model of relaxor polymers," *Phys. Rev. B*, vol. 72, p. 014202, 2005.

[27] D. I. Woodward, R. Dittmer, W. Jo, D. Walker, D. S. Keeble, M. W. Dale, J. Rdel, and P. A. Thomas, "Investigation of the depolarisation transition in Bi-based relaxor ferroelectrics," *J. Appl. Phys.*, vol. 115, p. 114109, 2014.

[28] A. A. Bokov and Z. G. Ye, "Recent progress in relaxor ferroelectrics with perovskite structure," *J. Mat. Sci.*, vol. 41, pp. 31–52, 2006.

[29] R. Pirc, Z. Kutnjak, and N. Novak, "Compressible spherical dipolar glass model of relaxor ferroelectrics." Arxiv pre-print, 2012.

[30] M. D. Glinchuk and R. Farhi, "A random field theory based model for ferroelectric relaxors," *J. Phys. Condens. Matter*, vol. 8, pp. 6985–6996, 1996.

[31] M. Valant, L. J. Dunne, A.-K. Axelsson, N. Alford, and G. Manos, "Electrocaloric effect in a ferroelectric $Pb(Zn_{1/3}Nb_{2/3})O_3$-$PbTiO_3$ single crystal," *Phys. Rev. B*, vol. 81, p. 214110, 2010.

[32] R. Pirc, Z. Kutnjak, and N. Novak, "Electrocaloric effect in relaxor ferroelectrics," *App. Phys. Lett.*, vol. 98, no. 2, p. 021909, 2011.

[33] Z.-G. Ye, Y. Bing, J. Gao, A. A. Bokov, P. Stephens, B. Noheda, and G. Shirane, "Development of ferroelectric order in relaxor (1-x)Pb($Mg_{1/3}Nb_{2/3}$)O_3xPbTiO_3 (0∼x∼0.15)," *Phys. Rev. B.*, vol. 67, no. 10, p. 104104, 2003.

[34] R. Blinc, J. Dolinek, A. Gregorovi, B. Zalar, and C. Filipi, "Local polarization distribution and edwards-anderson order parameter of relaxor ferroelectrics," *Phys. Rev. Lett.*, vol. 83, no. 2, pp. 424–427, 1999.

[35] L. E. Cross, "Relaxor ferroelectrics," *Ferroelectrics*, vol. 76, no. 1, pp. 241–267, 1987.

[36] R. Pirc and R. Blinc, "Spherical random-bond-random-field model of relaxor ferroelectrics," *Phys. Rev. B*, vol. 60, p. 13470, 1999.

[37] Q. M. Zhang, "Giant electrostriction and relaxor ferroelectric behavior in electron-irradiated poly(vinylidene fluoride-trifluoroethylene) copolymer," *Science*, vol. 280, no. 5372, pp. 2101–2104, 1998.

[38] G. Samara and L. Boatner, "Ferroelectric-to-relaxor crossover and oxygen vacancy hopping in the compositionally disordered perovskites KTa1-xNbxO3:Ca," *Phys. Rev. B*, vol. 61, no. 6, pp. 3889–3896, 2000.

[39] W. Li, H. Zeng, J. Hao, and J. Zhai, "Enhanced dielectric and piezoelectric properties of Mn doped ($Bi_{0.5}Na_{0.5}$)TiO_3($Bi_{0.5}K_{0.5}$)TiO_3SrTiO_3 thin films," *Journal of Alloys and Compounds*, vol. 580, pp. 157–161, 2013.

[40] F. Le Goupil, A.-K. Axelsson, L. J. Dunne, M. Valant, G. Manos, Lukasiewicz, J. Dec, A. Berenov, and N. M. Alford, "Anisotropy of the electrocaloric effect in lead-free relaxor ferroelectrics," *Advanced Energy Materials*, vol. 4, no. 9, p. 1301688, 2014.

[41] G. Akcay, S. P. Alpay, J. V. Mantese, and G. a. Rossetti, "Magnitude of the intrinsic electrocaloric effect in ferroelectric perovskite thin films at high electric fields," *Appl. Phys. Lett*, vol. 90, no. 25, p. 252909, 2007.

[42] A. S. Mischenko, Q. Zhang, J. F. Scott, R. W. Whatmore, and N. D. Mathur, "Giant electrocaloric effect in thin-film Pb$Zr_{0.95}Ti_{0.05}O_3$," *Science*, vol. 311, no. 5765, pp. 1270–1271, 2006.

[43] V. K. Agarwal and V. K. Srivastava, "Thickness dependence of breakdown field," *Thin solid Films*, vol. 8, pp. 377–381, 1971.

[44] H. K. Kim and F. G. Shi, "Thickness dependent dielectric strength of a low-permittivity dielectric film," *IEEE Transactions on Dielectrics and Electrical Insulation*, vol. 8, no. 2, pp. 348–252, 2001.

[45] X. Li, X.-S. Qian, H. Gu, X. Chen, S.-G. Lu, M. Lin, F. Bateman, and Q. M. Zhang, "Giant electrocaloric effect in ferroelectric poly(vinylidenefluoride-trifluoroethylene) copolymers near a first-order ferroelectric transition," *Appl. Phys. Lett.*, vol. 101, no. 13, p. 132903, 2012.

[46] M. Lallart, *Ferroelectrics - Physical Effects*. InTech, first ed., 2011.

[47] P. Atkins and L. Jones, *Chemistry. Molecules, Matter, and Change*. W. H. Freeman and Company, third ed., 1997.

[48] A. L. Allred, "Electronegativity values from thermochemical data," *Journal of Inorganic and Nuclear Chemistry*, vol. 17, pp. 215–221, 1961.

[49] Y. J. Park, S. J. Kang, C. Park, K. J. Kim, and H. S. Lee, "Irreversible extinction of ferroelectric polarization in P(VDF-TrFE) thin films upon melting and recrystallization.," *Appl. Phys. Lett.*, vol. 28, no. 24, p. 242908, 2006.

[50] Y. Imry and M. Wortis, "Influence of quenched impurities on first-order phase transitions," *Phys. Rev. B*, vol. 19, no. 7, pp. 3580–3585, 1979.

[51] V. Westphal, W. Kleemann, and M. k, "Diffuse phase transitions and random-field-induced domain states of the "relaxor" ferroelectric $PbMg_{1/3}Nb_{2/3}O_3$," *Phys. Rev. Lett.*, vol. 68, no. 6, pp. 847–850, 1992.

[52] V. K. Pecharsky and K. A. Gschneidner Jr., "Giant Magnetocaloric Effect in $Gd_5(Si_2Ge_2)$," *Phys. Rev. Lett.*, vol. 78, p. 4494, 1997.

[53] W. L. Bragg and E. J. Williams, "The effect of thermal agitation on atomic arrangement in alloys," *Proc. R. Society A*, vol. 145, p. 699, 1934.

[54] J. B. Staunton, R. Banerjee, M. dos Santos Dias, A. Deák, and L. Szunyogh, "Fluctuating local moments, itinerant electrons, and the magnetocaloric effect: Compositional hypersensitivity of FeRh," *Phys. Rev. B*, vol. 89, no. 5, p. 054427, 2014.

[55] K. Aikoh, S. Kosugi, T. Matsui, A. Iwase, K. Aikoh, S. Kosugi, T. Matsui, and A. Iwase, "Quantitative control of magnetic ordering in FeRh thin films using 30 keV Ga ion irradiation from a focused ion beam system," *J. Appl. Phys.*, vol. 109, p. 07E311, 2011.

[56] S. Carnot, *Réflexions sur la puissance motrice du feu et sur les machines propres à développer cette puissance.* Chez Bachelier, Libraire, 1824.

[57] L. Reichl, *A Modern Course in Statistical Physics.* Wiley VCH, second ed., 1998.

[58] M. E. Wood and W. H. Potter, "General analysis of magnetic refrigeration and its optimization using a new concept: maximization of refrigerant capacity," *Cryogenics*, vol. 25, no. 12, pp. 667–683, 1985.

[59] C. W. Miller, D. V. Williams, N. S. Bingham, and H. Srikanth, "Magnetocaloric effect in Gd/W thin film heterostructures," *Journal of Applied Physics*, vol. 107, no. 9, p. 09A903, 2010.

[60] L. Li, M. Kadonaga, D. Huo, Z. Qian, and T. Namiki, "Low field giant magnetocaloric effect in RNiBC (R = Er and Gd) and enhanced refrigerant capacity in its composite materials," *Appl. Phys. Lett.*, vol. 101, no. 12, p. 122401, 2012.

[61] E. Stern-taulats, A. Planes, and C. Frontera, "Barocaloric and Magnetocaloric Effects in $FE_{49}Rh_{51}$," *Phys. Rev. Lett.*, vol. 58, no. 2, pp. 86–88, 1987.

[62] J. Liu, T. Gottschall, K. P. Skokov, J. D. Moore, and O. Gutfleisch, "Giant magnetocaloric effect driven by structural transitions," *Nature Materials*, vol. 11, no. 7, pp. 620–626, 2012.

[63] L. Caron, M. Hudl, V. Höglin, N. H. Dung, C. P. Gomez, M. Sahlberg, E. Brück, Y. Andersson, and P. Nordblad, "Magnetocrystalline Anisotropy and the Magnetocaloric Effect in Fe_2P," *Arxiv Pre-Print*, p. 16, 2013.

[64] L. Landau, "On the theory of phase transitions," *Zh. Eksp. Teor. Fiz.*, vol. 7, pp. 19–32, 1937.

[65] A. F. Devonshire, "XCVI. Theory of Barium Titanate," *Phil. Mag.*, vol. 40, pp. 1040–1063, 1949.

[66] V. L. Ginzburg and L. Landau, "To the theory of superconductivity," *Zh. Eksp. Teor. Fiz.*, vol. 20, p. 1064, 1950.

[67] W. Cao, "Constructing landau-ginzburg-devonshire type models for ferroelectric systems based on symmetry," *Ferroelectrics*, vol. 375, pp. 28–39, 2008.

[68] Y. P. Shi and A. K. Soh, "Modeling of enhanced electrocaloric effect above the curie temperature in relaxor ferroelectrics," *Acta Materialia*, vol. 59, no. 14, pp. 5574–5583, 2011.

[69] L. I. Vinokurova, V. A. Vlasov, and M. Pardavi-Horvath, "Pressure Effects on Magnetic Phase Transitions in FeRh and FeRhIr Alloys," *Phys. Stat. Sol. (b)*, vol. 78, p. 353, 1976.

[70] H. Chen, T.-l. Ren, X.-m. Wu, Y. Yang, and L.-t. Liu, "Giant electrocaloric effect in lead-free thin film of strontium bismuth tantalite," *Appl. Phys. Lett.*, vol. 94, p. 182902, 2009.

[71] P. Weiss and A. Piccard, "Sur un nouveau phénomene magnétocalorique," *Comptes Rendus Herbomdaires des séances de l'académie des sciences*, vol. 166, p. 352, 1917.

[72] A. Aharoni, *Introduction to the Theory of Ferromagnetism.* Oxford Science Publications, 1996.

[73] D. Prato and D. E. Barraco, "Bogoliubov inequality," *Revista Mexicana de Física*, vol. 42, no. 1, pp. 145–150, 1996.

[74] B. Wunderlich, *Handbook of Thermal Analysis and Calorimetry. Vol 3: Applications to Polymers and Plastics.* Elsevier Science, 2002.

[75] P. Debye, "Zur Theorie des spezifischen Waerme," *Annalen der Physik*, vol. 39, no. 4, p. 789, 1912.

[76] P. M. Chaikin and T. C. Lubensky, *Principles of Condensed Matter Physics.* Cambridge University Press, 2000.

[77] M. Reece and C. Zhu. personal communication.

[78] C. Zhu, "Ferroelectric materials for future thermal management applications," 2013.

[79] J. P. Zheng, "Dielectric properties of pvdf films and polymer laminates with pvdf for energy storage applications," *Proceedings of The 6th International Conference on Properties and Applications of Dielectric Materials*, pp. 423–426, 2000.

[80] J. B. Staunton. personal communication.

[81] J. Ricodeau and D. Melville, "Model of the Antiferromagnetic-Ferromagnetic Transition in FeRh Alloys," *Journal of Physics F: Metal Physics*, vol. 2, no. 2, pp. 337–350, 1972.

[82] D. W. Cooke, F. Hellman, and C. Baldasseroni, "Thermodynamic Measurements of Fe-Rh Alloys," *Phys. Rev. Lett.*, vol. 109, p. 255901, 2012.

[83] J. V. Driel, R. Coehoorn, G. J. Strijkers, E. Brück, and F. R. D. Boer, "Compositional dependence of the giant magnetoresistance in Fe_x Rh_{1x} thin films," *J. Appl. Phys.*, vol. 85, no. 2, p. 1026, 1999.

[84] L. J. Swartzendruber, "The Fe-Rh (Iron-Rhodium) System," *Bull. Alloy Phase Diagrams*, vol. 5, no. 5, p. 456, 1984.

[85] M. P. Annaorazov, S. A. Nikitin, A. L. Tyurin, K. A. Asatryan, and A. K. Dovletov, "Anomalously high entropy change in FeRh alloy Anomalously high entropy change in FeRh alloy," *J. Appl. Phys.*, vol. 79, no. 3, pp. 1689–1695, 1996.

[86] M. J. Richardson, "Specific Heat Measurements on an FeRh Alloy," *Phys. Lett.*, vol. 46A, no. 2, pp. 153–154, 1973.

[87] S. Nikitin, G. Myalikgulyev, M. Annaorazov, A. Tyurin, R. Myndyev, and S. Akopyan, "Giant elastocaloric effect in FeRh alloy," *Phys. Lett. A*, vol. 171, pp. 234–236, 1992.

[88] A. M. Goldsborough, J. M. Fellows, M. Bates, S. A. Rautu, G. Rowlands, and R. A. Römer, "Leaf-to-leaf distances in catalan tree graphs," *Arxiv Pre-Print*, p. 47, 2015.

[89] T. Koshy, *Catalan Numbers with Applications*. Oxford University Press, 2nd ed., 2009.

[90] H. S. Wilf, *Generatingfunctionology*. Academic Press Inc., 2nd ed., 1994.

[91] N. Metropolis, "The Beginning of the Monte Carlo Method," *Los Alamos Science*, vol. 15, no. 584, pp. 125–130, 1987.